Technical Report

STABILITY AND VIBRATIONS OF INTERNAL WINDINGS OF HIGH-CURRENT SUPERCONDUCTING SOLENOID MAGNETS

K. Hara and F. C. Moon

December 1984

submitted to the
Office of Naval Research
Structural Mechanics Program, Material Sciences Division
ONR Contract No. N00014-79-C-0224
Task No. NR 064-621

Departments of Theoretical & Applied Mechanics
and Structural Engineering
Cornell University
Ithaca, New York 14853

ABSTRACT

High field solenoid magnets may experience internal damage or eventually collapse due to the powerful magnetic fields they produce. Elastic deformations of the conductor and insulation in these magnets deserve attention because they can cause local damage that can lead to electrical breakdown. In conventional stress analysis of cylindrically wound magnets, the magnetic field gradient, or magnetic stiffness, is usually neglected. However, in this thesis the magnetic stiffness is shown to have a significant effect on the elastic stability and vibration of these magnets.

One-turn and multi-turn superconducting rings were used to study the effects of deformations on stability and vibration. Both static and dynamic methods were used to determine the critical buckling currents. The dispersion of natural frequencies with increase in current and subsequent in-plane and out-of-plane buckling of the rings near the critical buckling current were observed.

A model based on ring theory and magnetic stiffness was developed to explain experimental observations and showed a fair to good agreement between experimental and theoretical values of the buckling current. This model was used to evaluate the buckling current of 7- and 10-turn magnets. The analysis showed buckling concentrated in the outer turns.

ACKNOWLEDGEMENTS

This report is essentially a reproduction of the thesis submitted in May 1984 by the first author in partial fulfillment for the degree of Doctor of Philosophy. The second author, Professor Francis C. Moon, supervised this research. The authors would also like to thank Bryon Shapey who helped conduct the experiments. In addition to sponsorship by the Office of Naval Research, portions of this work were also supported by the National Science Foundation under a grant from the Mechanical Engineering and Applied Mechanics Program of the Engineering Division.

TABLE OF CONTENTS

Chapter		Page
1	INTRODUCTION	1
	1.1 Introduction to Superconducting Magnets	1
	1.1.1 Superconductor	2
	1.1.2 Superconducting Magnets	3
	1.1.3 Magnet Systems for Fusion and Their Structural Problems	6
	1.1.4 Internal Buckling of Windings	11
	1.2 Literature Survey	15
	1.3 Objective and Scope of the Work	19
2	GENERAL THEORY	23
	2.1 Theory of Electromagnetism	23
	2.1.1 Electromagnetic Field Equations	23
	2.1.2 Electromagnetic Constitutive Equations and Ohm's Law	24
	2.1.3 Boundary Conditions	26
	2.1.4 Potential Functions	29
	2.1.5 Inductance and Vector Potential	31
	2.1.6 Magnetic Force and Magnetic Stiffness	32
	2.1.7 Magnetic Field by a Circular Current Loop	34
	2.2 Theory of Elasticity	37
	2.2.1 Deformation - Compatibility	37
	2.2.2 Linear Momentum and the Stress Tensor - Equilibrium Equations	38
	2.2.3 Balance of Angular Momentum	39
	2.2.4 Constitutive Equations	40
	2.2.5 Problem Statement in Dynamic Elasticity	41
	2.3 Ring Theory	43
	2.3.1 Kinematics	43
	2.3.2 Equilibrium Equations	46
	2.3.3 Constitutive Equations	47
	2.3.4 In-Plane Deformation	48
	2.3.5 Out-of-Plane Deformation	49

Chapter		Page
3	EXPERIMENT	50
	3.1 Buckling and Vibration of Superconducting Rings	50
	3.1.1 Purpose	50
	3.1.2 Experimental Model	52
	3.1.3 Experimental Apparatus	57
	3.1.4 Measurement System	59
	3.1.5 Procedure	63
	3.1.6 Experimental Result	64
	3.2 Buckling of Pancake Winding by a High Current Pulse Discharge	81
	3.2.1 Description of Experiment	81
	3.2.2 Experimental Result	83
4	THEORETICAL ANALYSIS AND COMPARISON WITH EXPERIMENTAL RESULTS	87
	4.1 Magnetic Field in the Concentric Ring Model	87
	4.2 Single Ring in the Transverse Magnetic Field	94
	4.2.1 Derivation of Equation	94
	4.2.2 Comparison Between Theory and Experiment	101
	4.2.3 Nondimensionalization	108
	4.3 Multi Ring Analysis	112
	4.3.1 Derivation of Equations	112
	4.3.2 Comparison Between Analytical and Experimental Results	120
	4.3.3 General Analysis	129
5	CONCLUSIONS	143
	5.1 Summary	143
	5.2 Conclusions	146
	5.3 Suggestions for Further Research	147
	APPENDIX A	149
	APPENDIX B	151
	REFERENCES	153

LIST OF FIGURES

Figure		Page
1.1	Illustration of the major components of the magnet for the fusion Engineering Test Facility.	8
1.2	MFTF-B with cutaways to reveal arrangement of machine components and magnetic configuration in the buidling . .	10
1.3	End view of rectangular distribution transformer coils with core removed after being subjected to short-circuit currents in excess of design capability	13
1.4	Part of the windings of a high-powered solenoid distorted through the action of electromagnetic forces.	14
1.5	Typical cross-section of MFTF-B coil.	20
2.1	Pillbox and circuit contour for the derivation of the boundary jump conditions.	27
2.2	Current carrying loop located in the xy plane and point P where the magnetic field will be calculated	35
2.3	Differential element AB of a rectangular cross section cut out of the ring and orientation of the forces and moments at P.	44
3.1	Internal structure of superconducting solenoid magnets and experimental model.	51
3.2	Schematic of one-ring model experiment and top view of three-ring experiment	54
3.3	Experimental apparatus for one-ring, two-ring, and three-ring experiments.	55
3.4	Close up of experimental apparatus showing interturn springs, strain gauges, and driving coils	56
3.5	Cutaway diagram of experimental set up.	60
3.6	Electrical power and data collection system	62
3.7	Experimental strain vs. current squared (proportional to magnetic force) curves for one-ring model without interturn rings.	66
3.8	Southwell plot of static data for one-ring model without interturn springs	67

Figure		Page
3.9	Experimental current-frequency dispersion curve for one-ring model without interturn springs.	68
3.10	Experimental strain vs. current squared curve for one-ring model with interturn springs.	70
3.11	Southwell plot of static data for one-ring model with interturn springs	71
3.12	Experimental current-frequency dispersion curves for one-ring model with interturn springs	72
3.13	Experimental strain vs. current squared (proportional to magnetic force) curves for two-ring model with interturn springs	74
3.14	Experimental current-frequency dispersion curves for two-ring model with interturn springs	75
3.15	Experimental strain vs. current squared curves for three-ring model with interturn springs	77
3.16	Southwell plot of middle ring for three-ring model with interturn springs	78
3.17	Southwell plots of inner ring for three-ring model with interturn springs	79
3.18	Experimental current-frequency dispersion curves for three-ring model with interturn springs	80
3.19	Set up for buckling pancake winding experiment and measured current	82
3.20	Pancake winding buckled by pulsed high current.	84
3.21	Close up of buckled pancake winding showing expansion inside and deformation outside due to compression.	85
4.1	Circular current loop and z component of its magnetic field	88
4.2	Z component of magnetic field produced by 10 concentric coplanar rings (r = 11-20 cm)	89
4.3	Z component of magnetic field acting on 14 cm ring calculated by removing the 14 cm ring	91
4.4	Z component of magnetic field acting on 20 cm ring calculated by removing the 20 cm ring	92

Figure		Page

4.5 Magnetic field acting on each ring produced by other rings. 93

4.6 In-plane rigid body motion (n = 0 and 1) and bending deformation (n = 2, 3, 4, ...) of circular ring 100

4.7 Theoretical current-frequency dispersion curves for one-ring model without interturn springs. 104

4.8 Theoretical current-frequency dispersion curves for one-ring model with interturn springs 107

4.9 Nondimensionalized critical buckling load vs. nondimensionalized spring constant for carrying ring in transverse magnetic field. 111

4.10 Nondimensionalized critical buckling load vs. nondimensionalized magnetic stiffness for current carrying ring in transverse magnetic field 113

4.11 Three-dimensional plot of nondimensionalized critical buckling load vs. mechanical stiffness vs. magnetic stiffness for current carrying ring in transverse magnetic field. 114

4.12 Theoretical current-frequency dispersion curves for two-ring model with interturn stiffness 123

4.13 Theoretical current-frequency dispersion curves for circumferential second mode for three-ring model with interturn stiffness 126

4.14 Theoretical current-frequency dispersion curves of circumferential fourth mode for three-ring model with interturn stiffness. 127

4.15 Comparison of experimental and theoretical current-dispersion curves for three-ring model with interturn stiffness 128

4.16 Theoretical current-frequency dispersion curves for circumferential second mode for three-ring model with interturn stiffness 131

4.17 Theoretical current-frequency dispersion curves for circumferential third mode for three-ring model with interturn stiffness 132

4.18 Theoretical current-frequency dispersion curves for circumferential eighth mode for three-ring model with interturn stiffness 133

Figure		Page
4.19	Theoretical current-frequency dispersion curves of circumferential sixth mode for seven-ring model with interturn stiffness	137
4.20	Radial or circumferential deflection vs. position curves when current is zero and at buckling for circumferential sixth (C6) mode of seven-ring model with interturn springs	138
4.21	Theoretical current-frequency dispersion curves for circumferential third (C3) mode for ten-ring model with interturn springs	140
4.22	Theoretical current-frequency dispersion curves of circumferential sixth (C6) mode for ten ring-model with interturn springs	141
4.23	Radial or circumferential deflection vs. position curves at buckling of circumferential third (C3) and sixth (C6) modes for ten-ring model with interturn springs	142

LIST OF TABLES

Table		Page
1.1	Comparison of large superconducting magnet systems.	4
4.1	Experimental and theoretical values of buckling constants and natural frequencies for one-ring model without springs.	103
4.2	Experimental and theoretical critical buckling constants for one-ring model with springs	106
4.3	Comparison of experimental and theoretical critical currents and natural frequencies for two-ring model with interturn stiffness	122
4.4	Theoretical critical currents, natural frequencies and deformation ratios of the three-ring model with interturn stiffness	125
4.5	Theoretical critical buckling currents for three-ring model with interturn stiffness.	130
4.6	Theoretical critical buckling currents for seven-ring model with interturn stiffness.	136
4.7	Theoretical critical buckling currents for ten-ring model with interturn stiffness.	139

CHAPTER 1

INTRODUCTION

1.1 Introduction to Superconducting Magnets

Development of reliable magnets is central to the goal of economic usage of high magnetic fields in such applications as magnetic fusion energy, magnetohydrodynamics (MHD), accelerators in nuclear physics, and nuclear magnetic resonance (NMR) for medical use.

The renaissance of magnetic technology started in the early 1950's with the establishment of high energy accelerators. About a decade later in 1961, high-field superconducting laboratory magnets became a reality, after the discovery of superconductivity. Conventional electromagnets, which are still used widely, operate at near zero efficiency. To generate high magnetic fields in a useful volume, considerable amounts of power are needed. Superconducting magnets, on the other hand, consume a minimal amount of power required for refrigeration.

The design and construction of superconducting magnets are central to the economic feasibility of high magnet field technologies. At the same time, these devices have to be constructed on a scale many times larger and more costly than any magnet constructed to date. This will require an interdisciplinary effort among engineers who today may have limited experience with magnet design fundamentals.

The development of superconducting materials remarkably improved the magnetic energy storage capacity, which has led to the development of a number of superconducting devices and applications as mentioned above.

At the same time, this technology brought with it a new set of engineering problems in both the electrical and mechanical sciences. Some problems involve the design and manufacture of the superconducting material itself, while others involve magnet construction or overall system problems. This thesis seeks to explain the problems located within the mechanical aspects; specifically vibrations and structural stability of the superconducting magnets.

1.1.1 Superconductor

The superconducting phenomenon of mercury was discovered by Kamerlingh Onnes in 1911. However, it was 50 years before superconducting materials were discovered which could sustain high current densities and magnetic fields without becoming resistive or normal [Rose-Innes (1978)]. They are generally referred to as "hard superconductors" of Type II. NbTi and Nb_3Sn are the most common compounds of this type commercially available.

In order for a superconductor to be in its superconducting state (as opposed to its "normal state"), the temperature, field and current must all be below certain "critical" values, and these values are interrelated [Brechna (1973)]. At a given temperature and level of transverse magnetic field, for example, the material has a "critical current," at which the transition from the superconducting to normal state takes place. The critical current for a given high-field material is extremely sensitive to material and structure. Any given alloy will show little change in critical temperature or upper critical field with changes in metallurgical treatment, such as cold work or annealing, but the critical currents will show wide variations.

Niobium-titanium conductors, for example, if operated at 1.8 K have sufficient critical current to generate field of 12 T. The superior mechanical characteristics of NbTi make them attractive despite the lack of temperature margin available. Conversely, Niobium-tin, with its much higher critical field, can be operated at 4.5 K but it has well known unattractive brittle mechanical properties. To achieve high current densities, it was found that the superconducting material should be backed with a good conductor or small filaments of these materials embedded in a copper matrix should be used.

1.1.2 Superconducting Magnets

The status of the technology of large superconducting magnets in terms of stored magnetic energy for selected devices is given in Table 1.1. The stored energy is the energy contained in the magnetic field at an operating level for each system. It is a measure of the size of the device, because stored magnetic energy is proportional to the integral of the square of the local magnetic field over all space. It is also a measure of structural requirements because the magnetic energy density can be interpreted as a nonuniform pressure which is exerted on the current-carrying elements. This pressure must be restricted by the structural components of the system.

The systems in Table 1.1 are grouped into three basic types. The first four systems are bubble chamber magnets for high-energy physics. These are identified by locations as follows: Brookhaven National Laboratory (BNL), Argonne National Laboratory (ANL), Fermi National Accelerator Laboratory (FNAL), and Centre Européen pour la Researche

Table 1.1 Comparison of Large Superconducting Magnet Systems

Device	Type	Status	Stored Energy (MJ)
BNL	Bubble Chamber	complete	12
ANL	Bubble Chamber	complete	80
FNAL	Bubble Chamber	complete	395
CERN	Bubble Chamber	complete	800
U25	MHD	complete	34
ETL	MHD	complete	60
CFFF	MHD	under construction	168
CDIF	MHD	under construction	200
ETF	MHD	design	2,900
CDP	MHD	design	6,300
BL	MHD	design	15,200
MFTF	Fusion (Mirror)	under construction	3,000
LCTF	Fusion (Tokamak)	under construction	700
INTOR	Fusion (Tokamak)	design	35,000
CRR	Fusion (Tokamak)	design	108,000

Nucléaire (CERN). These four are complete. In comparison to the MHD and fusion configurations, the bubble chamber solenoidal magnets are simple and straightforward. The axial symmetry inherent in a solenoidal configuration leads to magnetic and mechanical design problems which are much less severe than the other two types.

The second class of magnet systems consists of MHD magnet systems, of which two are complete and operational, two are under construction, and three are in the conceptual design stage. The first listed (U25-B) was built at ANL and installed in the bypass loop of the U25 MHD test facility in Moscow. The second system is at the Japanese Electro-Technical Laboratory (ETL). Of the two magnets under construction, the first is to be used at the Coal-Fired Flow Facility (CFFF) at the University of Tennessee, while the second is to be used at the CDIF in Montana. The final three magnet systems are conceptual designs for three successive stages of development envisioned for commercialization of MHD. These include the engineering test facility (EFT), the commercial demonstration plant (CDP), and a full-scale magnet for base load (BL) operation.

The last type of the magnet systems consists of fusion magnet systems, of which two are under construction and two are in the conceptual design stage. The first of these is for the Mirror Fusion Test Facility (MFTF) at Lawrence Livermore National Laboratory. The geometry of this system is different from that of the other three fusion systems listed here. This systems is the largest superconducting magnet presently under construction in the United States. The second fusion magnet system under construction is for the LCTF at the Oak Ridge National

Laboratory. The final two systems listed are conceptual designs for the commercialization of fusion. Both are based on Tokamak configurations. The first is for the fusion engineering test facility (ETF), while the value given for the commercial power reactor (CPR) is based on the UWMAK III design generated at the University of Wisconsin.

The range of stored energies given on Table 1.1 is indicative of the enormous size of the magnet systems which are believed to be necessary to commercialize MHD and fusion technologies. The step from existing superconducting magnets to the magnets necessary for commercialization is an enormous one, as indicated by the increase in stored energy and size. A clear understanding of the magnetic field and force design fundamentals is necessary for making such a step successful and cost efficient.

1.1.3 Magnet Systems for Fusion and Their Structural Problems

Development of reliable magnets is the main technological problem to realize economic fusion power. Because they are expensive and interlocked aspects of the reactor, magnets must have a life-expectancy similar to the lifetime of the reactor. The Mirror Fusion Test Facility (MFTF) and the Large Coil Program (CLP) are the major superconducting projects which will provide technical data to design future magnets. Successful completion of these tests will give the confidence necessary to advance on the much larger fusion Engineering Test Facility (ETF) or International Tokamak Reactor (INTOR) in the last half of this decade.

In this section the Tokamak reactor will be described first, followed by the MFTF, Mirror type, and finally their structural problems.

Tokamak

Tokamaks are "closed system" toroidal devices, as opposed to the "open system" linear mirror devices. The closed systems have achieved plasma confinement time and density combinations much in advance of the mirror systems and are therefore judged most appropriate for the next steps in the fusion program.

An outline of the fusion EFT, the next-step fusion system, is shown in Figure 1.1 [Haubenreich (1981)]. The magnet system consists of toroidal field (TF) coils and the poloidal field (PF) coils. The TF coils produce the high magnetic field in the toroidal direction. The PF coils include the ohmic heating (OH) solenoid, interior and exterior equilibrium field (EF) coils, and create vertical and radial magnetic fields.

The Tokamaks require a pulsed vertical or poloidal field for the induction of plasma current, produced by OH coils, in addition to a steady-state toroidal field produced by TF coils. After ignition the plasma is then controlled by EF coils. This is the major drawback of the Tokamak magnet system. The toroidal field coils will be in a steady-state, but the conductors will be exposed in varying degrees, to the pulse fields from the poloidal field systems.

Superconducting magnet technology is being developed in the Large Coil Task Program, a six coil torus which will only simulate the electromagnetic interactions from the plasma [Gray (1979)]. The majority of main-line experiments operating and under construction are all copper coil systems. The next-step Tokamak ETF will use superconducting magnets. The capital cost of copper and superconducting systems

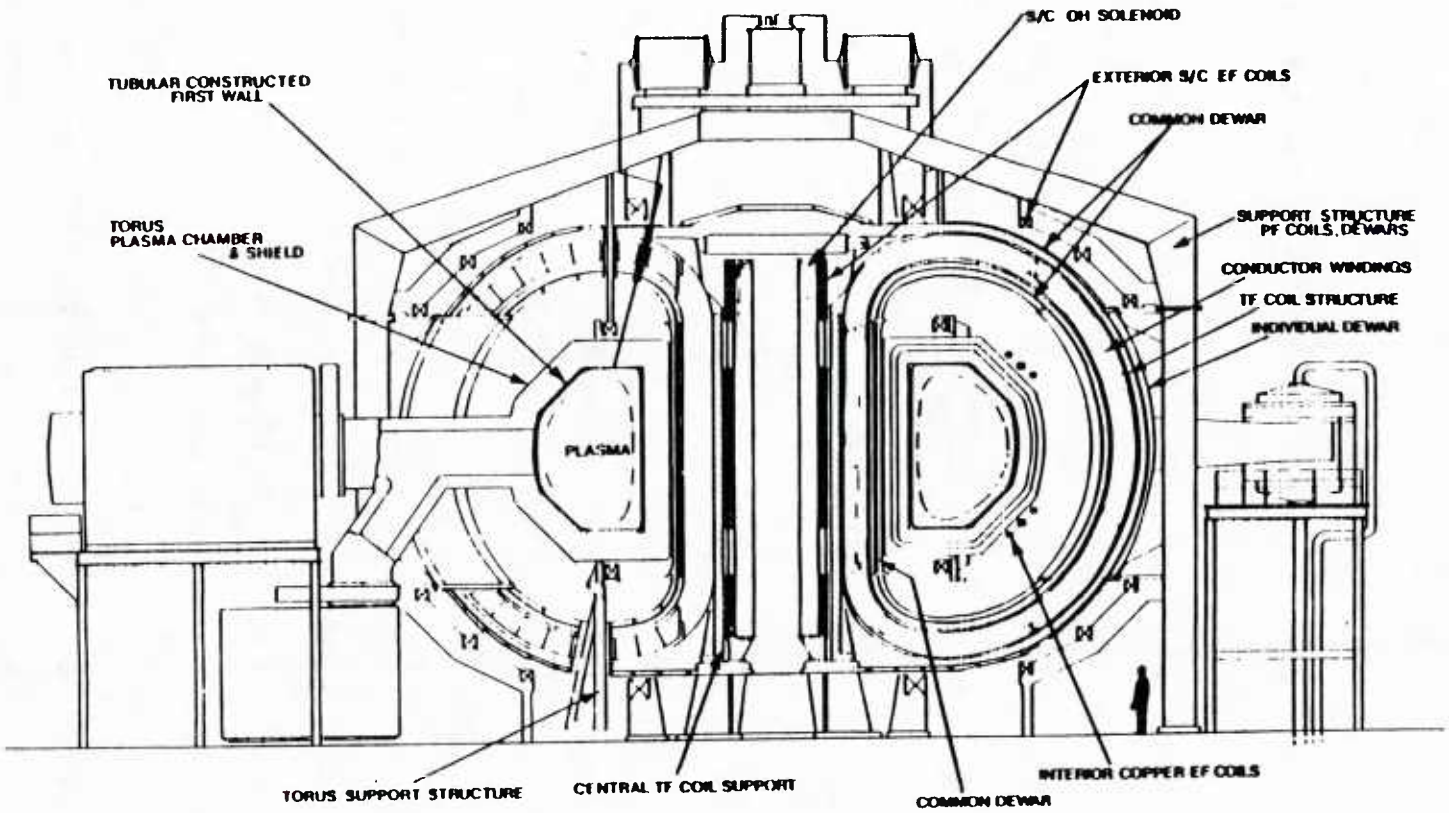

Figure 1.1 Illustration of the major components of the magnet for the fusion Engineering Test Facility

are nearly the same. The choice of superconducting coils for the next-step is being made largely by the need for the development of reliable overall systems which will be required when economic electricity production becomes a primary focus.

Mirror Fusion

The magnetic mirror program has been a major driving factor of superconducting magnet development, mainly because of its steady-state magnetic field. In 1980, the mirror program embarked on a tandem mirror, MFTF-B which will store some 3000 MJ of energy, a factor of nearly four larger than the 800 MJ stored by CERN, the largest of the superconducting bubble chamber magnets built in the late 1970's. The birdseye view of the magnet system is given in Figure 1.2 [Henning (1980)].

The MFTF is being built in two stages. The first will consist of one mirror end-cell and multi-coil central cell. The Yin-Yang mirror coil for an end of the large tandem has already been constructed and tested. The severe structural requirements are evident in the scale of this structure which has nearly twice the volume of the coil. The magnets were designed with a design stress of 550 MPa. The structural material is 304 LN which has a yield stress of 925 MPa. The coil was wound on a 2.5 cm thick case which was later inserted into a heavier case varying in thickness from 7.6 cm to 12.7 cm.

The conductor used in a superconducting magnet as large as MFTF must contain sufficient copper and helium coolant to prevent so-called unconditional thermal stability. To satisfy this stability condition, an arbitrarily long length of conductors must be able to recover from a temperature excursion which is above the critical temperature of the

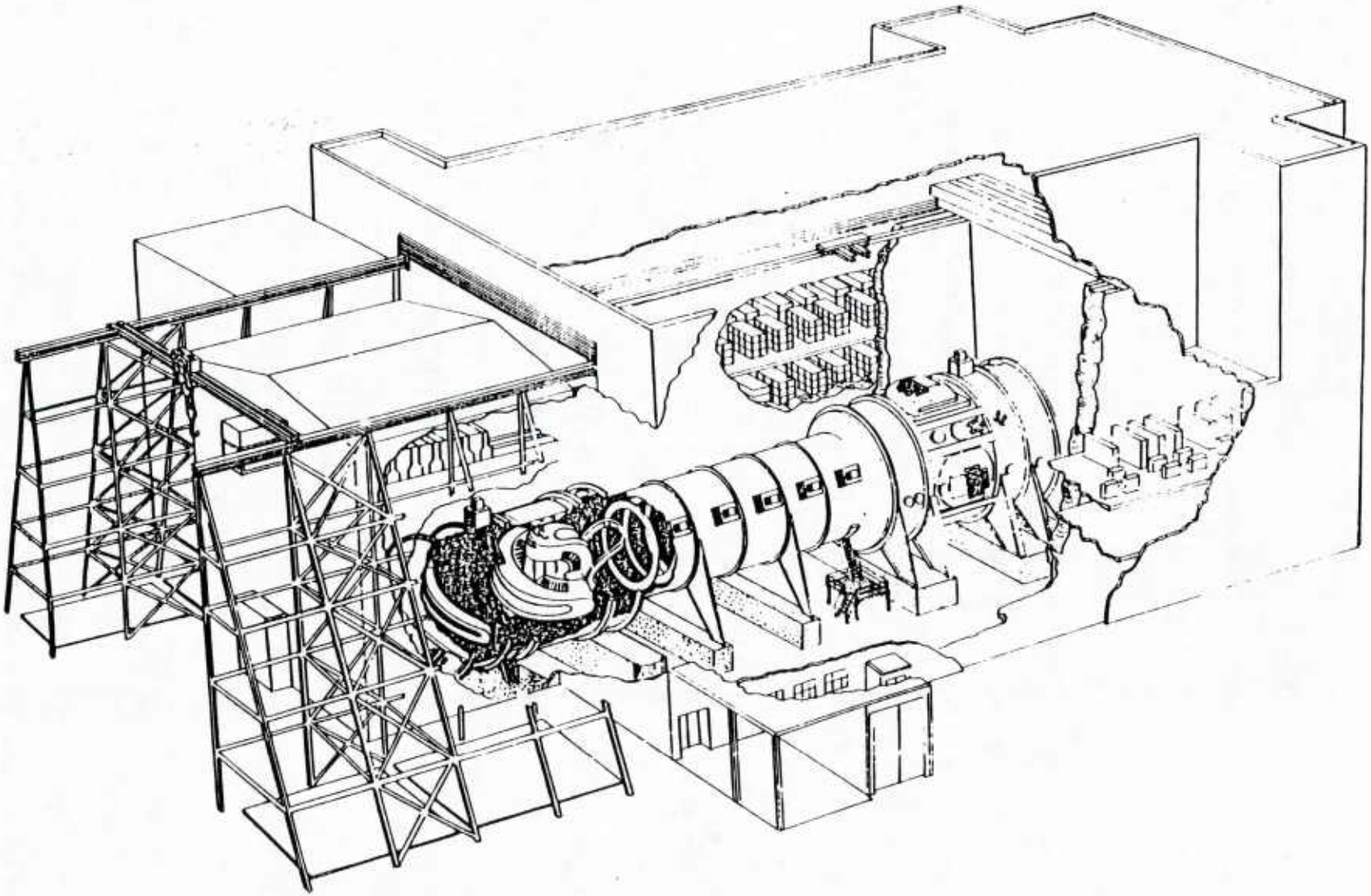

Figure 1.2 MFTF-B with cutaways to reveal arrangement of machine components and magnetic configuration in the building.

superconductor. This means that all the current will momentarily flow in the copper stabilizer, and that there must be sufficient cooling capacity to lower the temperature back to the operating point. For the MFTF conductor this requires that there be 6.7 times as much copper as NbTi, and that there be 8.17 cm^2 of cooling surface per centimeter of conductor length.

The conductor, were it a simple square 1.34 cm on a side, would only have 5 cm^2/cm of length, and hence a novel conductor with an extended surface has been chosen, which creates further complexity. However, there are certain disturbance inputs which are exceedingly difficult to simulate. For example, mechanical motion of the conductors within the housing generates heat through friction.

Because materials have very little heat capacity at helium temperature, even small friction heating can result in a significant temperature rise. If the heat input is large enough and occurs even a significant volume of the winding, it could vaporize a considerable amount of the coolant, leaving the winding without the means of recovery and consequently quenching of the system. The internal heating of windings inside the housing caused by structural motion of the windings is quite important and this is the main theme of this study.

1.1.4 Internal Buckling of Windings

As mentioned in previous sections, it is very important to analyze stress in large magnets because of their size and enormous amount of stored energy. This has been the main concern of magnet designers. However, structural devices are often load limited by the buckling of structural elements such as columns, plates and shells. The magnets and less-known cases of transformers are also load limited by buckling.

The example of the buckling of a transformer is given by Woodson and Melcher (1968). Figure 1.3 shows the primary and secondary windings of a distribution transformer which was intentionally subjected to currents in excess of its peak ratings. This is a step-down transformer with large secondary conductors on the outside and inside with primary windings sandwiched between. The secondary windings are constructed of sheets of aluminum which were originally wound in a rectangular shape. As shown in Figure 1.3, the excessive currents have distorted the secondary windings away from the primary windings. Although the result is not a gross mechanical failure of the structure, significant deformation of the insulation causes local damage that can lead to electrical breakdown and also decreases the transformer efficiency.

The internal buckling of the high field magnet was first reported by Daniels (1953). He was designing water-cooled solenoids to produce fields of up to 4 T continuously. He observed a mechanical breakdown in one of the solenoids. A picture of a damaged coil from his paper is reproduced in Figure 1.4. The waves observed in the picture show the buckling due to the inward body forces on the outer layers.

Another example is the original design of superconducting dipole magnets for ISABELLE at BNL. The magnets were to achieve 5 T and be the highest performance superconducting dipole magnets ever built. However, due to the internal movement of windings or braided conductors, the magnet could achieve only 4 T and quenched for the higher currents.

Internal buckling similar to that of Daniels was observed in this thesis by conducting a high current through a pancake coil. This experiment will be described later in Section 3.2.

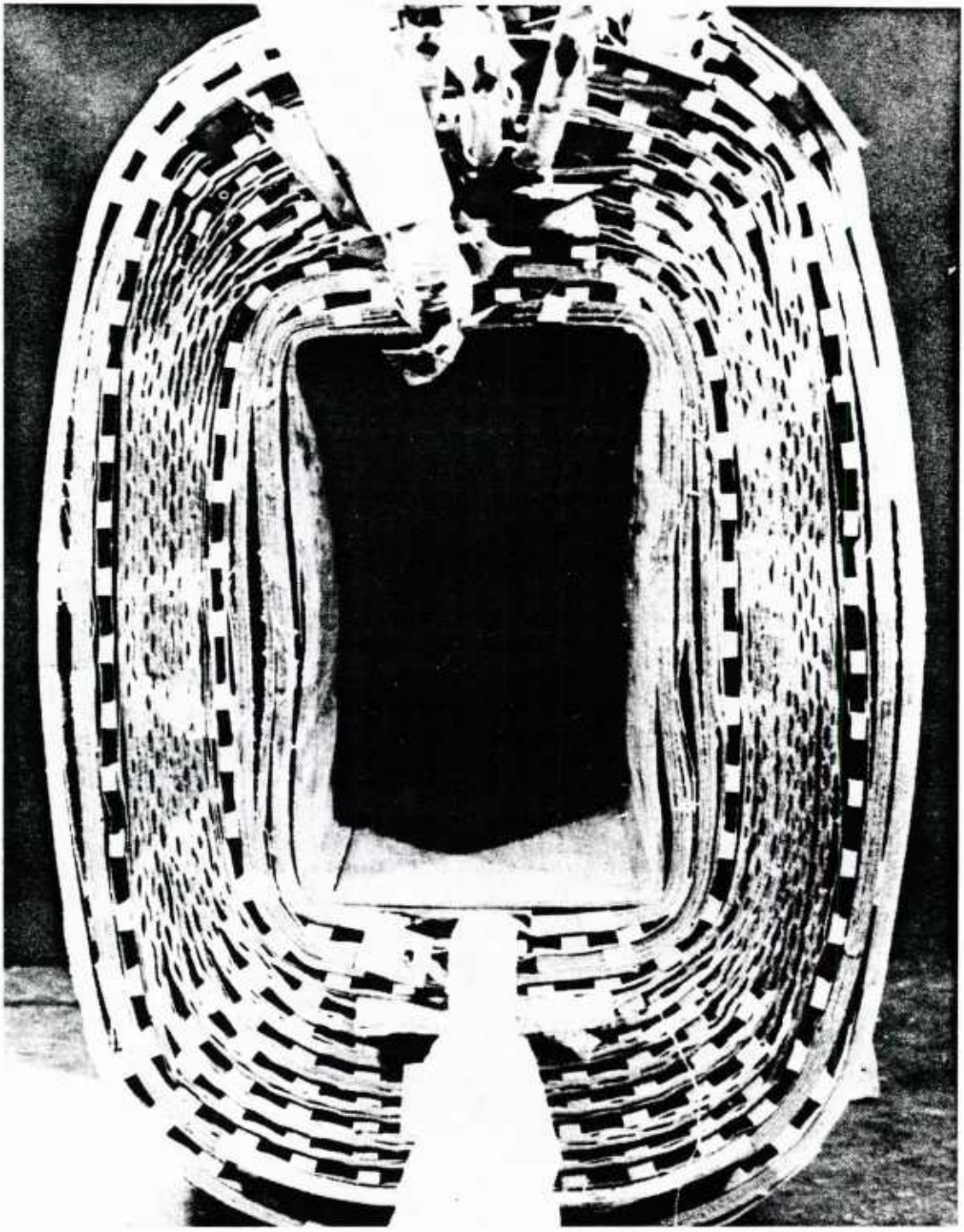

Figure 1.3 End view of rectangular distribution transformer coils with core removed after being subjected to short-circuit currents in excess design capability [Woodson and Melcher (1968)]

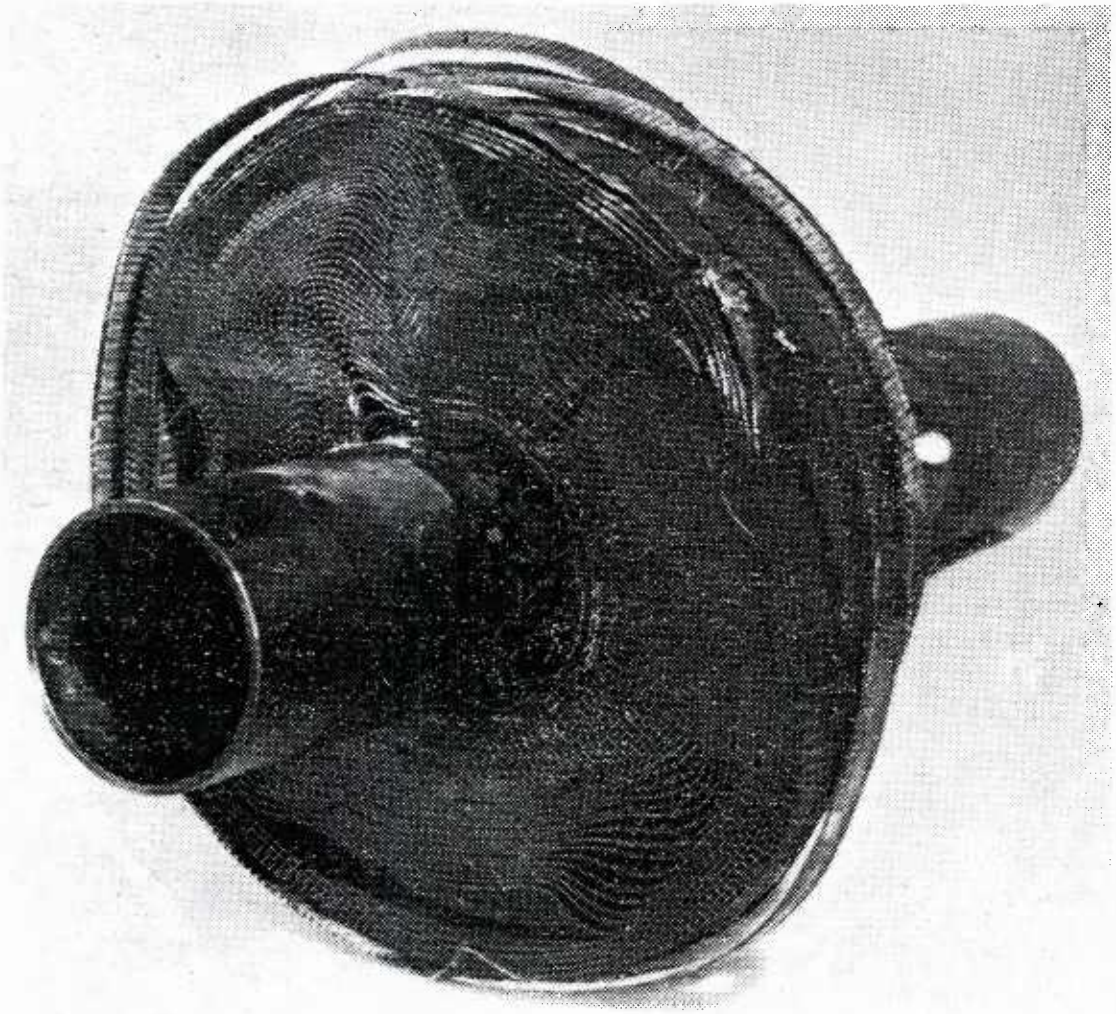

Figure 1.4 Part of the windings of a high-powered solenoid distorted through the action of electromagnetic forces. [Daniels (1953)]

This study seeks to explain and analyze this internal buckling of solenoidal magnets as well as the internal vibration of the coupled windings.

1.2 Literature Survey

Most studies on mechanics to this date have dealt with forces of mechanical origin. However, along with the engineering utilization of high magnetic fields, there has been some work on the effects of magnetic field on the motion of solid body. This study, known as electromagnetomechanics, encompasses the interaction of electromagnetism and Mechanics [Moon (1984)].

The interaction of the electromagnetic field with the solid medium has been examined by a number of authors. The work can be broadly classified into three categories:

1) Magnetization and strains in elastic magnetic bodies
2) Magnetic field with conducting elastic solids containing induced currents or eddy currents
3) Self magnetic fields of current carrying conductors and their deformation.

In the first category, or interaction of magnetic and strain field, one of the earliest works was performed by Kirchoff (1885), who calculated the change of shape of an iron sphere when magnetized by a constant magnetic field. Since then, many authors have worked on this subject. An important reference to the theoretical treatment of ferromagnetic solids is the work of Brown (1962). The application of theories of internal stresses to solve practical problems has remained very scarce in literature.

A new branch of this category was opened by Moon and Pao (1968). They pointed out that the moment on a ferromagnetic plate, when placed in a transverse magnetic field, is proportional to the rotational angle, and proved the existence of buckling both theoretically and experimentally. Known as the magnetoelastic buckling, this study gave basis for the buckling of current-carrying conductors. However, the theoretical critical magnetic fields obtained by them were larger than the experimental results by the factor of 2.

Miya, Hara et al. (1978) experimented with the buckling of a ferromagnetic plate by systematically changing the ratio of width to thickness, and showed that experimental and theoretical values are close when the ratio of width to thickness is large. Also, they calculated the concentration of magnetic field using the finite element method, and calibrated the experimental results.

Miya, Takagi et al. (1980) solved the out-of-plane deformation of plates and the magnetic field in them simultaneously using the finite element method, and showed the difference between experimental and theoretical results was in an error range of 25%. Recently Moon and Hara (1982) showed experimentally similar buckling with martinsitic stainless steel which is proposed to be used in fusion reactors.

The second category of problems, or currents induced in elastic conductors by magnetic fields, has a long history dating back to the work of Maxwell (1891). The work of Jeans (1925) followed the methods of Maxwell. Smythe (1968) presented solutions to a number of classic problems, including eddy currents in cylindrical and spherical bodies, and plane sheet conductors. The specialized monographs on the subject

of eddy currents were done by Lammeraner and Stafl (1966) and Stoll (1974). Most of the analytical methods are based on the magnetic field vector potential. The fields treated were mostly uniform and harmonically varying due to the limitation of analytical methods.

However, the recent development of numerical methods such as the finite element and boundary methods has sparked renewed interest in eddy current research. Miya and Hara (1980) solved the problem of the induced current in a cylinder due to a transient magnetic field, by the finite element method using the vector potential. They also compared the result with the experiment in which the strain was measured directly with a strain gauge. Yuan et al. (1981) has solved the problem of induced currents in two-dimensional plates by the finite element method using the stream function.

The last category, or the mechanics of current-carrying solids, includes the contents of this study.

The earliest work dealt with the total force and moment on the body. These include the work of Maxwell (1891), Jeans (1925) and Smythe (1968). The other works concerning magnetic forces due to electric currents include Hague (1929) and Dwight (1945).

However, it is the resulting stress distribution that is of interest to the designers of magneto-mechanical devices and to this author. Since even in self-equilibrated magnetic systems, large stresses exceeding yield stresses can be encountered, stress analysis is one of the main parts of magnet design. There are specialized monographs which deal with magnet design. These monographs were written by Brechna (1972), Montgomery (1980), and Thome and Tarrh (1982).

The survey of literature related to magnet windings or current induced stresses begins with Kapitza (1927) and Cockcroft (1928). In designing a pulsed magnet, they calculated the stress induced by currents. However, they neglected the circumferential stress in the equilibrium equation, which led them to an erroneous result of radial stress for a constant current density magnet.

Daniels (1953) discussed the cause of failure in high field solenoidal coils due to internal buckling of the turn. He used the energy method involving both the magnetic and elastic energies. However, he neglected the contribution of the compressive circumferential stress.

Furth et al. (1957) analyzed stresses in coils using the magnetic pressure concept. In Russia, Landau and Lifshitz (1960) gave a simple analysis of the stresses in a circular ring using the dependence of the inductance on the geometry of the ring. Kuznetsov (1960, 1961) presented a two-dimensional analysis of stresses in a solenoid.

An anisotropic analysis of wound coils was first given by Gersdorf et al. (1965). They introduced different Young's moduli for the circumferential and radial directions, and a filling factor, namely the percentage of conducting volume to total volume. Their method was used by Melvill and Mattocks (1972) to analyze the failure of a pulsed cylindrical coil of 16 tesla.

Recent studies have been further refined with the advancement in development of superconducting magnets. They include the winding prestress, thermal cooldown effects and magnetic body forces. Kokavec and Cesnak (1977) calculated all three effects and provided some

comparison with experimental results. Arp (1977) considered the cumulative effect of winding on a bobbin, bobbin removal, cooldown and magnetic forces for both constant and variable tension winding stress. He showed that a variable tension winding scheme can lead to a more uniform total stress across the radial dimension of the coil.

Johnson, Gray and Weed (1976) treated the cylindrical solenoid as a concentric set of rings separated by an insulation layer. Each conductor ring is modeled as anisotropic material. They showed the combined effect.

Bobrov and Williams (1980) treated the superconducting solenoid as a set of nested orthotropic rings. They presented stress states due to windings, cooldown, and magnetic forces. This study is one of the first to examine the radial vibration of such a composite coil. However, they did not take into account the effect of compression or tension on bending of the rings, and could not predict the buckling.

1.3 Objective and Scope of the Work

The turns in a high field superconducting solenoid magnet may move or eventually collapse due to the powerful magnetic field they produce. Significant deformations of the conductor and insulation deserve attention because they cause local damage that can lead to electrical breakdown. Linear stress analysis in some of these magnets has failed to predict high deflections and stresses, and in some cases failures of large superconducting magnets have occurred.

The objective of this work is to study the vibration and stability of cylindrically wound superconducting magnets. A superconducting solenoid magnet represents a nonhomogeneous mechanical system. Figure 1.5

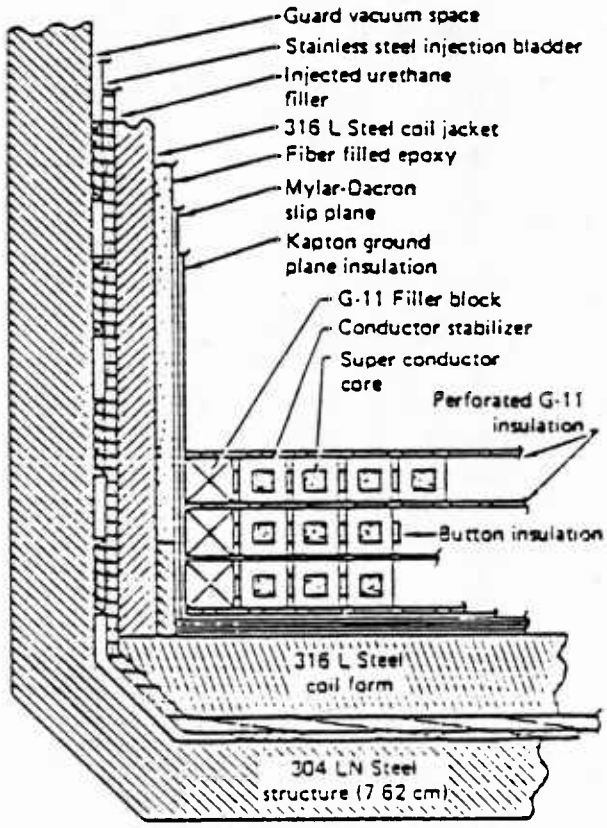

Figure 1.5 Typical cross-section of MFTF-B coil

shows the typical cross section of a superconducting magnet, in this case from MFTF-B [Horvath (1980)]. The elements included in the structure are supporting cores, active conductor and insulator layers, and layers of reinforcement. The strains and stresses arise in the magnet from conductor tension during the winding, from anisotropic differential contraction during cooldown, and from the Lorentz force. In this study, however, only the Lorentz force will be taken into account. In the experimental and analytical models, the helical winding of conductors are replaced by concentric rings, and the insulation is replaced by soft springs.

The effect of the magnetic field gradient, or magnetic stiffness, on the vibration and stability analysis will be extensively examined. The linearized theory of elasticity used in the previous studies fails to predict the buckling of a ring due to a uniform pressure on it, because the effect of compression or tension on bending of the ring is neglected. In this study the effect of the initial stress on the bending deformation in the rings will be taken into account.

The basic equations are provided in Chapter Two. The theory of electromagnetism and the linearized theory of elasticity are summarized to provide a proper background of the theory of magnetoelasticity for nonferrous conducting material. The magnetic field and its gradient due to a current carrying ring are discussed. On the mechanical side, ring theory is given in detail.

Chapter Three is devoted to the experiments. The experiment on the vibration and stability of superconducting rings will be treated first. One-turn and multi-turn superconducting rings are used to study

the vibration and stability. Both static and dynamic methods are used to determine the critical buckling currents. The dispersion of natural frequencies with increase in current are obtained. Then an internal buckling experiment of a normal pancake coil due to a high pulsed current will be described.

Chapter Four compares the analytical and experimental results. The magnetic field produced by multiple concentric rings will be discussed first. The equation of motion of a single ring in a transverse magnetic field with gradient is derived and the analytical results are compared with the experimental results. Finally the equations for the current carrying multiple ring model are derived. These results are also compared with the experimental results. This analysis is applied to general cases to predict the buckling and vibration of the system.

Conclusions on the results of the present study on the superconducting solenoid magnets are drawn in the last Chapter, together with some suggestions for further research in this area.

CHAPTER 2

GENERAL THEORY

2.1 Theory of Electromagnetism

Selected aspects of electromagnetic theory are reviewed in this section. Detailed, rigorous treatments are presented in standard texts on the subject [Jackson (1962) and Smythe (1968)].

2.2.1 Electromagnetic Field Equations

The electromagnetic fields are defined by four vectors, the electric field intensity $\underset{\sim}{E}$, the magnetic induction $\underset{\sim}{B}$, the electric displacement $\underset{\sim}{D}$, and the magnetic field intensity $\underset{\sim}{H}$, which satisfy the following set of equations known as Maxwell's equations:

(Faraday's Law)

$$\nabla \times \underset{\sim}{E} + \frac{\partial \underset{\sim}{B}}{\partial t} = 0 \tag{2.1.1}$$

(generalized Ampere's Law)

$$\nabla \times \underset{\sim}{H} - \frac{\partial \underset{\sim}{D}}{\partial t} = \underset{\sim}{J} \tag{2.1.2}$$

(conservation of magnetic flux)

$$\nabla \cdot \underset{\sim}{B} = 0 \tag{2.1.3}$$

(Gauss's Law)

$$\nabla \cdot \underset{\sim}{D} = \rho_e \quad . \tag{2.1.4}$$

Here, $\underset{\sim}{J}$ is the current density and ρ_e is the charge density.

Out of these four equations only the first two are independent. Equation (2.1.3) can be derived from equation (2.1.1), and also from equations (2.1.3) and (2.1.4),

$$\text{div}\ \underset{\sim}{J} + \frac{\partial \rho_e}{\partial t} = 0 \tag{2.1.5}$$

which is the equation of the conservation of charge.

These equations can be written in the form of balance laws, or integral forms as

(Faraday's Law)

$$\oint_C \underset{\sim}{E} \cdot d\underset{\sim}{\ell} = -\frac{\partial}{\partial t} \int_S \underset{\sim}{B} \cdot d\underset{\sim}{S} \tag{2.1.6}$$

(Ampere's Law)

$$\oint_C \underset{\sim}{H} \cdot d\underset{\sim}{\ell} = \int_S \underset{\sim}{J} \cdot d\underset{\sim}{S} + \frac{\partial}{\partial t} \int_S \underset{\sim}{D} \cdot d\underset{\sim}{S} \tag{2.1.7}$$

(conservation of magnetic flux)

$$\int_S \underset{\sim}{B} \cdot d\underset{\sim}{S} = 0 \tag{2.1.8}$$

(Gauss's Law)

$$\int_S \underset{\sim}{D} \cdot d\underset{\sim}{S} = \int_V \rho_e \, dV \tag{2.1.9}$$

In the first two expressions, the area S is enclosed by the closed curve C.

2.1.2 <u>Electromagnetic Constitutive Equations and Ohm's Law</u>

In a vacuum, the vectors $\underset{\sim}{D}$ and $\underset{\sim}{E}$, and the vectors $\underset{\sim}{B}$ and $\underset{\sim}{H}$ are related as

$$\underset{\sim}{D} = \varepsilon_o \underset{\sim}{E} \tag{2.1.10}$$

$$\underset{\sim}{B} = \mu_0 \underset{\sim}{H} \tag{2.1.11}$$

where ε_0 is the permitivity and μ_0 the permeability of the free space. In MKS unit systems they are related by the speed of light c as

$$c^2 = \frac{1}{\mu_0 \varepsilon_0} \quad . \tag{2.1.12}$$

In material media, on the other hand, the constitutive equations are more complicated, since material bodies are assumed to possess electrical polarization $\underset{\sim}{P}$ and magnetization $\underset{\sim}{M}$. These are defined by the equations as

$$\underset{\sim}{P} = \underset{\sim}{D} - \varepsilon_0 \underset{\sim}{E} \tag{2.1.13}$$

$$\underset{\sim}{M} = \frac{\underset{\sim}{B}}{\mu_0} - \underset{\sim}{H} \tag{2.1.14}$$

which are consistent with the definitions of $\underset{\sim}{D}$ and $\underset{\sim}{H}$ in a vacuum.

In classical linear theory, these equations take the form

$$\underset{\sim}{P} = \varepsilon_0 \eta \underset{\sim}{E} \quad \text{or} \quad \underset{\sim}{D} = \varepsilon_0 (1 + \eta) \underset{\sim}{E} = \varepsilon \underset{\sim}{E} \tag{2.1.15}$$

$$\underset{\sim}{M} = \chi \underset{\sim}{H} \quad \text{or} \quad \underset{\sim}{B} = \mu_0 (1 + \chi) \underset{\sim}{H} = \mu \underset{\sim}{H} \tag{2.1.16}$$

where η and χ are called the electric susceptibility and magnetic susceptibility. The additional constants ε and μ are the permittivity and permeability of the medium, respectively.

In a typical magnetic field system the conduction process accounts for the free current density in materials. The most common constitutive relationship in stationary materials is Ohm's Law:

$$\underset{\sim}{J} = \sigma \underset{\sim}{E} \tag{2.1.17}$$

where σ is the electrical conductivity. The conductivity is typically assumed to be constant within a region.

However, for moving materials, the Ohm's Law is modified as

$$\underset{\sim}{J} = \sigma(\underset{\sim}{E} + \underset{\sim}{v} \times \underset{\sim}{B}) \tag{2.1.18}$$

Thus a moving conductor in a stationary magnetic field will have induced currents even if the initial electric field $\underset{\sim}{E} = 0$.

2.1.3 Boundary Conditions

The differential equations given in the preceding sections govern the relationship between the field variables in any region of space. If several regions having different properties are involved, boundary conditions are required to determine how the fields cross the surface which separates one region from another. These boundary conditions can be derived using the integral form of the equations given earlier.

As to the magnetic field, two boundary conditions must be considered, one to specify the relationship between the components of the field normal to a boundary, and the other tangent to a boundary. First, equation (2.1.8) is applied to a small closed cylindrical surface placed so its faces are in two regions parallel to the boundary between regions, as shown in Figure 2.1.a. The dimensions of the cylinder are reduced about a point P located on the boundary, which is within the cylindrical surface. The result is a condition which requires that the component of $\underset{\sim}{B}$ normal to the boundary be continuous, which can be expressed as

$$\underset{\sim}{n} \cdot (\underset{\sim}{B}_1 - \underset{\sim}{B}_2) = 0 \tag{2.1.19}$$

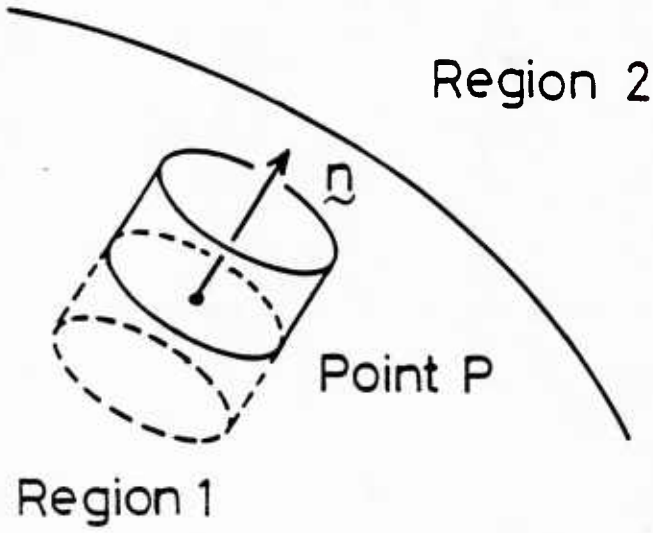

Cylindrical closed surface which surrounds a point P on the boundary between regions 1 and 2

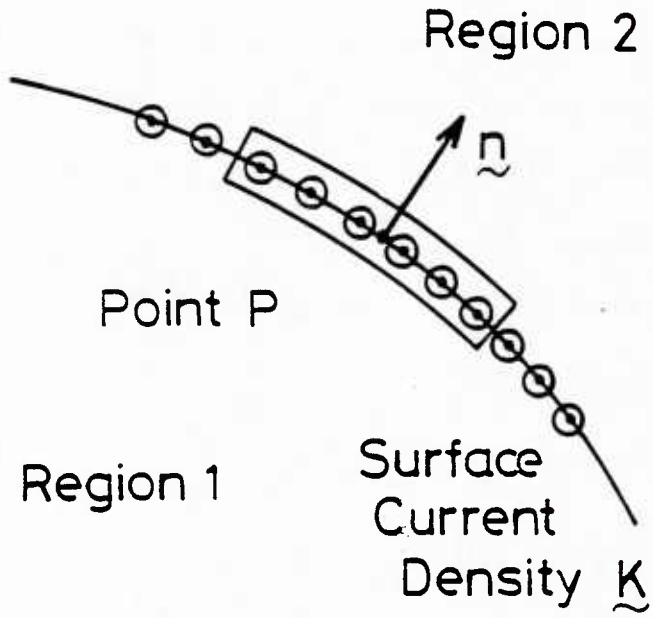

Closed contour in a plane perpendicular to a surface between regions 1 and 2. The surface carries a current sheet K.

Figure 2.1 Pillbox and circuit contour for the derivation of the boundary jump conditions

where $\underset{\sim}{B}_1$ and $\underset{\sim}{B}_2$ are the magnetic flux densities at P in regions 1 and 2, respectively, and $\underset{\sim}{n}$ is a unit vector at P normal to the boundary and directed from region 1 to region 2.

The second boundary condition can be found by applying equation (2.1.7) to a contour which surrounds a small plane perpendicular to the boundary between regions 1 and 2, as shown in Figure 2.1.b. If $\underset{\sim}{n}$ is again a unit vector at P defined the same as before, then shrinking the dimensions about P results in

$$\underset{\sim}{n} \times (\underset{\sim}{H}_2 - \underset{\sim}{H}_1) = \underset{\sim}{K} \tag{2.1.20}$$

where $\underset{\sim}{K}$ is a surface current density or current sheet which flows in the boundary. This is often absent in practical problems. This boundary condition requires that the component of $\underset{\sim}{H}$ tangential to the surface be discontinuous at the boundary if a current sheet exists, and that the discontinuity in $\underset{\sim}{H}$ be equal in magnitude to the surface current density and at right angle to it.

Two boundary conditions of the electric field can be derived in the same way. They are

$$\underset{\sim}{n} \cdot (\underset{\sim}{D}_2 - \underset{\sim}{D}_1) = \sigma_s \tag{2.1.21}$$

$$\underset{\sim}{n} \times (\underset{\sim}{E}_2 - \underset{\sim}{E}_1) = 0 \tag{2.1.22}$$

where σ_s is the surface charge density to the boundary surface.

The same technique derives the boundary condition on the current density given as

$$\underset{\sim}{J} \cdot \underset{\sim}{n} = 0 \tag{2.1.23}$$

on free boundary.

2.1.4 Potential Functions

Potential functions can be used to reduce the number of variables or otherwise simplify the process of finding a solution to the governing equation. The requirement of equation (2.1.3) that the divergence of $\underset{\sim}{B}$ be zero leads to the definition of a vector potential $\underset{\sim}{A}$ of the form

$$\nabla \times \underset{\sim}{A} = \underset{\sim}{B} \quad . \tag{2.1.24}$$

Though equation (2.1.24) alone is not sufficient to define $\underset{\sim}{A}$, by imposing

$$\nabla \cdot \underset{\sim}{A} = 0 \tag{2.1.25}$$

as a constraint, $\underset{\sim}{A}$ is fully defined.

Substituting equation (2.1.24) into equation (2.1.1) leads to

$$\nabla \times (\underset{\sim}{E} + \frac{\partial \underset{\sim}{A}}{\partial t}) = 0 \tag{2.1.26}$$

to the definition of a scalar potential ϕ. This scalar potential automatically satisfies equation (2.1.25), since the curl of the gradient of a scalar function is zero. Therefore,

$$\underset{\sim}{E} = - \nabla\phi - \frac{\partial \underset{\sim}{A}}{\partial t} \quad . \tag{2.1.27}$$

Equations (2.1.27) and (2.1.17) can be used with (2.1.6) to yield

$$\nabla \cdot \sigma \, (\nabla\phi + \frac{\partial \underset{\sim}{A}}{\partial t}) = 0 \tag{2.1.28}$$

where there is assumed to be no free charge. In addition, substituting (2.1.17), (2.1.16), (2.1.21) and (2.1.25) into equation (2.1.2) yields

$$(\nabla \times \frac{1}{\mu}\nabla \times A) + \sigma(\nabla\phi + \frac{\partial \underset{\sim}{A}}{\partial t}) = 0 \tag{2.1.29}$$

These two equations are the governing equations in terms of the two unknown potential functions $\underset{\sim}{A}$ and σ which can be used in place of the field equations for $\underset{\sim}{E}$ and $\underset{\sim}{B}$.

They are used in the following manner. If the current density distribution is known in a region and is the driver in the particular configuration, then the governing equation for the region becomes

$$\nabla \times \frac{1}{\mu} \nabla \times \underset{\sim}{A} = \underset{\sim}{J}_c \quad . \tag{2.1.30}$$

This equation drives the solution in the other regions, which are governed by equations (2.1.28) and (2.1.29).

In a region of constant permeability μ and no displacement current, equations (2.1.2) and (2.1.22) require that

$$\nabla^2 \underset{\sim}{A} = -\mu \underset{\sim}{J} \quad . \tag{2.1.31}$$

Each of the vector potential components must satisfy Poisson's equation, which has a solution of form

$$\underset{\sim}{A} = \frac{\mu}{4\pi} \iint \frac{\underset{\sim}{J}\, dV}{r_{pq}} \tag{2.1.32}$$

r_{pq} = distance from point p where $\underset{\sim}{J}$ is measured to point q where $\underset{\sim}{A}$ is measured.

where the integral takes over the entire region.

Equation (2.1.32) gives a physical interpretation of $\underset{\sim}{A}$. Consider a closed circuit of small cross-section wire which carries a current of density $\underset{\sim}{J}$. Outside the wire there is no contribution to the volume integral of equation (2.1.32), because $\underset{\sim}{J} = 0$. Inside the wire

$\underset{\sim}{J}\, dV = I\, d\underset{\sim}{s}$, where I is the current and the $d\underset{\sim}{s}$ is the element of length in the direction of $\underset{\sim}{J}$. Then equation (2.1.32) becomes

$$\underset{\sim}{A} = \frac{\mu}{4\pi} \oint \frac{I\, d\underset{\sim}{s}}{r_{pq}} \quad . \tag{2.1.33}$$

This implies the vector contribution to $\underset{\sim}{A}$ at a point by a current-carrying element in a closed circuit parallel to that element.

Equations (2.1.24) and (2.1.32) can be manipulated to

$$\underset{\sim}{B} = \frac{\mu}{4\pi} \iiint_V \frac{(\underset{\sim}{J} \times \underset{\sim}{i}_{pq})}{r_{pq}}\, dV \tag{2.1.34}$$

$\underset{\sim}{i}_{pq}$ = a unit vector directed from p to q.

This equation is well-known as Biot-Savart Law.

2.1.5 <u>Inductance and Vector Potential</u>

The mutual inductance between two circuits 1 and 2 can be thought of as the flux linked by circuit 2 per unit in circuit 1 with zero current in circuit 2. Equation (2.1.24) defines the vector potential

$$\nabla \times \underset{\sim}{A} = \underset{\sim}{B} \quad . \tag{2.1.35}$$

The integral form of this equation is

$$\oint_C \underset{\sim}{A} \cdot d\underset{\sim}{s} = \iint_S \underset{\sim}{B} \cdot \underset{\sim}{n}\, dS \tag{2.1.36}$$

where C is a closed contour, and the right-hand side is the flux through a simply connected area bounded by C. If the contour coincides with circuit 2 which has zero current and if the field $\underset{\sim}{B}$ and thus $\underset{\sim}{A}$ are generated by a current I_1 in circuit 1, then the right-hand side is the total flux generated by circuit 1 and linked by circuit 2 as follows:

$$\iint_S \underset{\sim}{B} \cdot \underset{\sim}{n}\, dS = \Phi_{12} \quad . \tag{2.1.37}$$

However, in linear systems

$$\Phi_{12} = M_{12} I_1 \tag{2.1.38}$$

where M_{12} is the mutual inductance between circuit 1 and 2. Therefore,

$$M_{12} = \frac{1}{I_1} \oint_2 \underset{\sim}{A}_1 \cdot d\underset{\sim}{s}_2 \quad . \tag{2.1.39}$$

The subscript is added to $\underset{\sim}{A}$ to indicate that the vector potential is generated by the current I_1 in circuit 1, although it is measured and integrated around circuit 2 which has zero current. This relationship can be used to obtain accurate inductance calculations through numerical integration.

However, the mutual inductance is defined by geometry only. Substituting equation (2.1.31) into (2.1.37) yields

$$M_{12} = \frac{1}{I_1} \oint_2 \left[\frac{\mu}{4\pi} \oint_1 \frac{I_1\, d\underset{\sim}{s}_1}{r_{12}} \right] \cdot d\underset{\sim}{s}_2 = \frac{\mu}{4\pi} \oint_1 \oint_2 \frac{d\underset{\sim}{s}_1 \cdot d\underset{\sim}{s}_2}{r_{12}} \quad . \tag{2.1.40}$$

This formula is used throughout this study.

2.1.6 <u>Magnetic Force and Magnetic Stiffness</u>

Electromagnetic forces between steady, current carrying conductors can be calculated by a method which uses the magnetic energy function. When the current distributions can be approximated by a set of circuits with currents $\{I_j\}$, the magnetic energy W can be written in the form

$$W = \frac{1}{2} \sum_i \sum_j L_{ij}\, I_i\, I_j \tag{2.1.41}$$

where L_{ij} is the mutual inductance when $i \neq j$, and L_{ii} $(i = j)$ is the

self inductance. Then the generalized magnetic forces F are represented by [Crandall et al. (1968)]

$$F_\alpha = \frac{1}{2} \sum_i \sum_j \frac{\partial L_{ij}}{\partial u_\alpha} I_i I_j \quad . \tag{2.1.42}$$

When the inductances are analytic functions of the displacements, one can further expand the L_{ij} in a Taylor series in the $\{u_\alpha\}$ so that F_α has the form

$$F_\alpha = F_\alpha^0 - \sum_\beta \kappa_{\alpha\beta} u_\beta \tag{2.1.43}$$

where $\kappa_{\alpha\beta}$ are called the magnetic stiffnesses and are defined by

$$\kappa_{\alpha\beta} = - \frac{1}{2} \sum_i \sum_j \frac{\partial^2 L_{ij}}{\partial u_\alpha \partial u_\beta} I_i I_j \tag{2.1.44}$$

where the derivatives are evaluated at $u_\alpha = 0$ [Chattopadhyay (1973)].

It should be noted that the magnetic stiffness depends on the currents and can be positive (restoring) or negative (destabilizing). F_α^0 represents the modal magnetic forces that do not depend on the displacements and are defined by

$$F_\alpha^0 \equiv \frac{1}{2} \sum_i \sum_j \frac{\partial L_{ij}}{\partial u_\alpha} I_i I_j \quad . \tag{2.1.45}$$

In stress analysis, it is convenient to consider the force on a differential element. The electromagnetic force per unit volume on the conductor with the current density $\underset{\sim}{J}$ in the magnetic field $\underset{\sim}{B}$ is expressed as

$$\underset{\sim}{f} = \underset{\sim}{J} \times \underset{\sim}{B} \quad . \tag{2.1.46}$$

The magnetic field may be expanded in a Taylor series in terms of the displacement of the conductor, $\{u_\alpha\}$, as followed

$$\underset{\sim}{B} = \underset{\sim}{B}_0 + \frac{\partial \underset{\sim}{B}}{\partial u_\alpha} u_\alpha + O(u_\alpha^2) \tag{2.1.47}$$

where $(\partial \underset{\sim}{B}/\partial u_\alpha)$ is evaluated at $u = 0$ and is the magnetic field gradient and functions equivalently to the magnetic stiffness.

2.1.7 Magnetic Field by a Circular Current Loop

One has to calculate the vector potential $\underset{\sim}{A}$ first to obtain the magnetic field by a circular current loop [Smythe (1968)]. A circular loop or radius a, centered at the origin, and carrying a current I is lying in the xy plane as shown in Figure 2.2. The current density $\underset{\sim}{J}$ has a component only in the ϕ direction. Since the geometry is cylindrically symmetric, the observation point may be chosen in the xz plane ($\phi = 0$) for purposes of calculation. Then the azimuthal integration in equation (2.1.32) is symmetric about the x axis and the x component of the current does not contribute. This leads only to the y component, which is A_ϕ. Thus,

$$A_\phi = \frac{\mu I}{4\pi} \oint \frac{ds_\phi}{r} = \frac{\mu I}{2\pi} \int_0^\pi \frac{a \cos\phi \; d\phi}{[a^2 + \rho^2 + z^2 - 2a\rho \cos \phi]^{\frac{1}{2}}} \quad . \tag{2.1.48}$$

This integral can be expressed in terms of the complete elliptic integral K and E:

$$A_\phi = \frac{\mu I}{\pi k} \left(\frac{a}{\rho}\right)^{\frac{1}{2}} [(1 - \tfrac{1}{2}k^2)K - E] \tag{2.1.49}$$

where the argument of the elliptic integral is

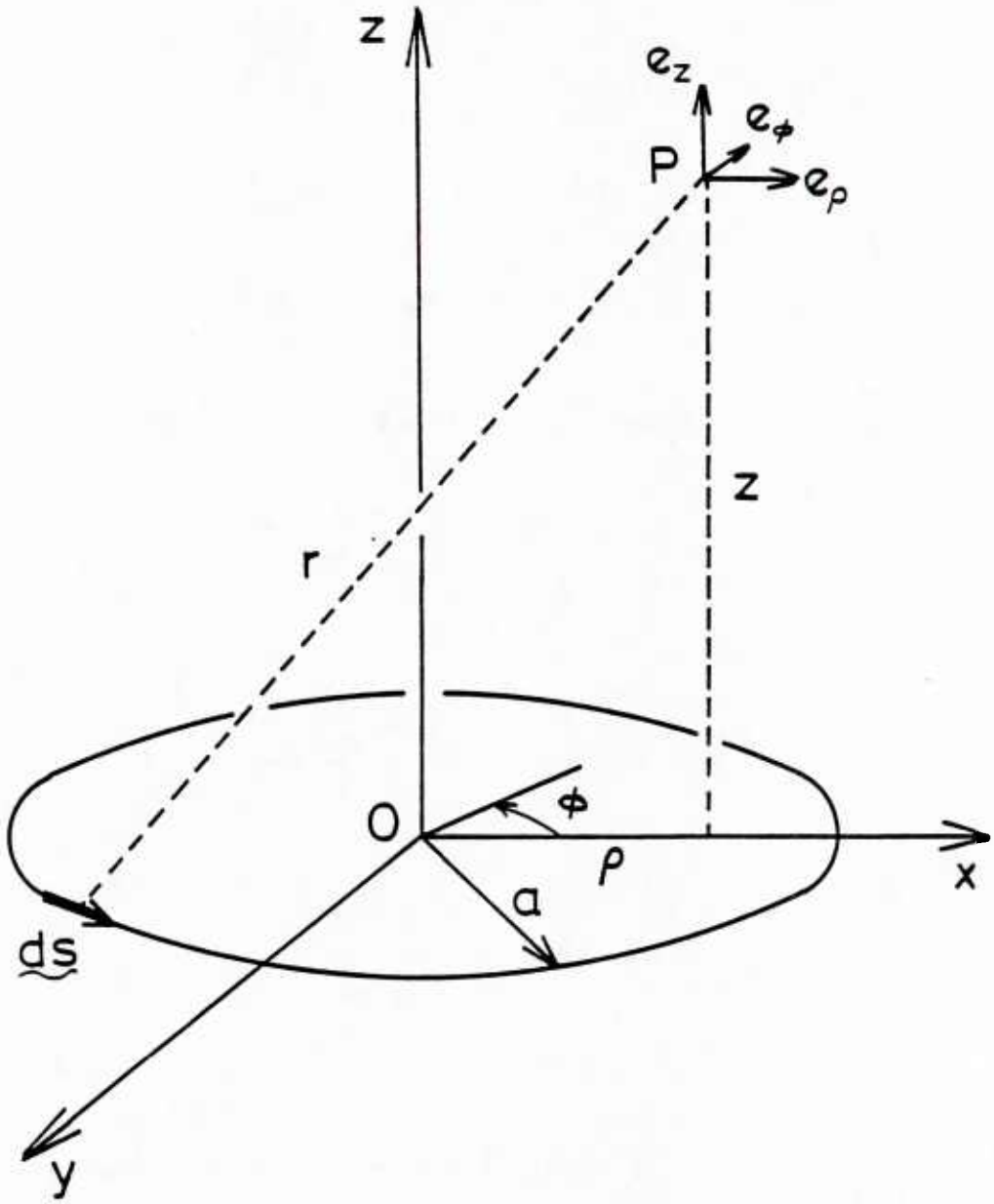

Figure 2.2 Current carrying loop located in the xy plane and point P where the magnetic field will be calculated

$$k^2 = \frac{4\ a\rho}{[(a + \rho)^2 + z^2]} \quad . \tag{2.1.50}$$

The components of the magnetic field

$$B_\rho = -\frac{1}{\rho}\frac{\partial}{\partial z}(\rho A_\phi) + \frac{1}{\rho}\frac{\partial}{\partial \phi}(A_z) = -\frac{\partial A_\phi}{\partial z} \tag{2.1.51}$$

$$B_\phi = \frac{\partial}{\partial z}(A_\rho) - \frac{\partial}{\partial \rho}(A_z) = 0 \tag{2.1.52}$$

$$B_z = -\frac{1}{\rho}\frac{\partial}{\partial \rho}(\rho A_\rho) + \frac{1}{\rho}\frac{\partial}{\partial \rho}(\rho A_\phi) = \frac{1}{\rho}\frac{\partial}{\partial \rho}(\rho A_\phi) \tag{2.1.53}$$

can also be expressed in terms of elliptic integrals:

$$B_\rho = \frac{\mu I}{2\pi}\frac{z}{\rho[(a + \rho)^2 + z^2]^{\frac{1}{2}}}\left[-K + \frac{a^2 + \rho^2 + z^2}{(a - \rho)^2 + z^2}E\right] \tag{2.1.54}$$

$$B_\phi = 0 \tag{2.1.55}$$

$$B_z = \frac{\mu I}{2\pi}[(a + \rho)^2 + z^2]^{-\frac{1}{2}}\left[K + \frac{a^2 - \rho^2 - z^2}{(a - \rho)^2 + z^2}E\right] \quad . \tag{2.1.56}$$

On the xy plane where z = 0, the magnetic field reduces to one component B_z, which is expressed as

$$B_z\Big|_{z=0} = \frac{\mu I}{2\pi}\left[\frac{K}{a + \rho} + \frac{E}{a - \rho}\right] \quad . \tag{2.1.57}$$

In the two-dimensional problem, in which there is only the z component of the magnetic field, the magnetic field gradient is calculated as

$$\frac{\partial B_z}{\partial \rho} = \frac{\mu I}{2\pi}\frac{1}{\rho(a + \rho)}\left[\frac{a^2 + \rho^2}{(a - \rho)^2}E - K\right] \tag{2.1.58}$$

$$\frac{\partial B_z}{\partial a} = - \frac{\mu I}{2\pi} \frac{2a}{(a + \rho)(a - \rho)^2} E \quad . \tag{2.1.59}$$

2.2 Theory of Elasticity

An elastic body has a natural undeformed state to which it returns when all external loads are removed. In this study, the current carrying elements are assumed to behave elastically according to the linearized theory of elasticity. The linearized theory of elasticity has been the subject of several treatises. In this study, the book by Sokolnikoff (1956) is the basic reference.

The equations governing the linearized theory of elasticity are presented in the following commonly used notation:

position vector	$\underset{\sim}{x}$	(coordinates x_i)	(2.2.1)
displacement vector	$\underset{\sim}{u}$	(components u_i)	(2.2.2)
strain tensor	$\underset{\approx}{\varepsilon}$	(components ε_{ij})	(2.2.3)
stress tensor	$\underset{\approx}{\tau}$	(components τ_{ij})	(2.2.4)

2.2.1 Deformation - Compatibility

The field defining the displacement of particles are denoted by $u(x,t)$. As a direct implication of the motion of a continuum, the deformation of the medium can be expressed in terms of the gradients of the displacement vector. In the manner of the linearized theory the deformation is described in a very simple way by the strain tensor $\underset{\approx}{\varepsilon}$, with components

$$\varepsilon_{ij} = \frac{1}{2}(u_{i,j} + u_{j,i}) \tag{2.2.5}$$

It is evident that $\varepsilon_{ij} = \varepsilon_{ji}$, i.e., $\underset{\approx}{\varepsilon}$ is a symmetric tensor of rank two.

2.2.2 Linear Momentum and the Stress Tensor - Equilibrium Equations

A basic postulate in the theory of continuum media is that the mechanical action of the material points which are situated on one side of an arbitrary material surface within a body upon those on the other side can be completely accounted for by prescribing a suitable traction on this surface. Thus if a surface element has a unit outward normal $\underset{\sim}{n}$ then the surface tractions T are defined as a force per unit area. The surface tractions depend on the orientation of $\underset{\sim}{n}$ as well as a location of the surface element.

Suppose a closed region V + S, where S is the boundary surrounding the body V. The surface S is subjected to a distribution of surface tractions $\underset{\sim}{T}(\underset{\sim}{x},t)$. Each mass element of the body may be subjected to a body force per unit volume, $\underset{\sim}{f}(\underset{\sim}{x},t)$. The principle of balance of linear momentum leads to the equation

$$\int_S \underset{\sim}{T}\, dS + \int_V \underset{\sim}{f}\, dV = \int_V \rho \ddot{u}\, dV \quad . \tag{2.2.6}$$

In magnetoelasticity the body force may be expressed as

$$\underset{\sim}{f} = \underset{\sim}{J} \times \underset{\sim}{B} + q\, \underset{\sim}{E} \quad . \tag{2.2.7}$$

for nonferromagnetic material. By means of the "tetrahedron argument," the equation (2.2.6) subsequently leads to the stress tensor $\underset{\sim}{\tau}$ with components $\tau_{k\ell}$, where

$$T_\ell = \tau_{k\ell}\, n_k \quad . \tag{2.2.8}$$

This equation is the Cauchy stress formula. Physically $\tau_{k\ell}$ is the component in the x_ℓ-direction of the traction on the surface with the unit

normal $\underset{\sim}{i}_k$.

Substitution of (2.2.8) into (2.2.6) and use of Gauss's theorem yields

$$\int_V (\tau_{k\ell,k} + \rho f_\ell - \rho \ddot{u}_\ell) dV = 0 \quad . \tag{2.2.9}$$

Since V may be an arbitrary part of the body, it follows that wherever the integral is continuous, one has

$$\tau_{k\ell,\ell} + \rho f_k - \rho \ddot{u}_\ell = 0 \quad . \tag{2.2.10}$$

This is the equation of equilibrium.

2.2.3 Balance of Angular Momentum

For the linearized theory, the principle of angular momentum states

$$\int_S (\underset{\sim}{x} \wedge \underset{\sim}{T}) dS + \int_V (\underset{\sim}{x} \wedge \underset{\sim}{f}) \rho dV = \int_V \rho \frac{\partial}{\partial t} (\underset{\sim}{x} \wedge \dot{\underset{\sim}{u}}) dV \tag{2.2.11}$$

if the body couple M is zero [Pao and Yeh (1973)]. By virtue of the equation of equilibrium, this equation reduces to

$$\int_V e_{k\ell m} \delta_{en} \tau_{nm} dV = 0 \tag{2.2.12}$$

or

$$e_{k\ell m} \tau_{\ell m} = 0 \quad . \tag{2.2.13}$$

This result implies that

$$\tau_{\ell m} = \tau_{m\ell} \tag{2.2.14}$$

i.e., the stress tensor is symmetric.

2.2.4 Constitutive Equations

For non-ferromagnetic, non-piezoelectric materials, the stress tensor is a function of the strain and temperature. When the thermal stress is neglected, the linear relationship between the components of the stress tensor and the components of the strain tensor is

$$\tau_{ij} = C_{ijkl}\,\varepsilon_{kl} \tag{2.2.15}$$

where

$$C_{ijkl} = C_{jikl} = C_{klij} = C_{ijkl} \tag{2.2.16}$$

because of the symmetry of stress and strain tensors. Thus, 21 of the 81 components of the tensor C_{ijkl} are independent. The medium is elastically homogeneous if the coefficients C_{ijkl} are constants. The material is elastically isotropic when there are no preferred directions in the material.

It can be shown that the elastic homogeneity and isotropy imply that the constants C_{ijkl} may be expressed [Sololnikoff (1956)] as

$$C_{ijkl} = \lambda\delta_{ij}\,\delta_{kl} + \mu(\delta_{ik}\,\delta_{jl} + \delta_{il}\,\delta_{jk}) \quad . \tag{2.2.17}$$

Then the constitutive equation, well known as the generalized Hooke's Law takes the form

$$\tau_{ij} = \lambda\varepsilon_{kk}\delta_{ij} + 2\mu\varepsilon_{ij} \quad . \tag{2.2.18}$$

The two elastic constants λ and μ contained in these equations are known as Lame's elastic constants.

Other elastic constants that often appear in linear elasticity are Young's modulus E and the Poisson's ratio ν. They are expressed in terms

of Lame's constants as

$$E = \frac{\mu(3\lambda + 2\mu)}{\lambda + \mu} \tag{2.2.19}$$

$$\nu = \frac{\lambda}{2(\lambda + \mu)} \quad . \tag{2.2.20}$$

2.2.5 Problem Statement in Dynamic Elasticity

The system of differential equations governing the motion of a homogeneous, isotropic, linearly elastic body consists of the equilibrium equations, the constitutive equations and the compatibility equations:

$$\tau_{ij,j} + f_i = \rho \ddot{u}_i \tag{2.2.21}$$

$$\tau_{ij} = \lambda \varepsilon_{kk} \delta_{ij} + 2\mu \varepsilon_{ij} \tag{2.2.22}$$

and

$$\varepsilon_{ij} = \frac{1}{2} (u_{i,j} + u_{j,i}) \tag{2.2.23}$$

respectively. In the analysis of a current carrying medium, the component of the body force is given as

$$f_i = (\underset{\sim}{J} \times \underset{\sim}{B})_i \quad . \tag{2.2.24}$$

If the compatibility equations are substituted into the constitutive equations and the expression of the stresses are subsequently substituted into the equilibrium equations, then the equation of motion is obtained as

$$\mu u_{i,jj} + (\lambda + \mu) u_{j,ji} + f_i = \rho \ddot{u}_i \tag{2.2.25}$$

Equations (2.2.21)-(2.2.23) and (2.2.25) must be satisfied at every interior point of the body.

On the surface S of the undeformed body, boundary conditions must be prescribed. The following boundary conditions are the most common:

(1) Displacement boundary conditions; the three components u_i are prescribed on the boundary.

(2) Traction boundary conditions; the three traction components T_i are prescribed on the boundary with unit normal $\underset{\sim}{n}$, through Cauchy's formula

$$T_i = \tau_{ji} n_j \quad . \tag{2.2.26}$$

In magnetoelasticity, this traction is zero on a free surface for a nonferrous media. But when magnetization is present it is sometimes expressed in terms of Maxwell's stress tensor [Brown (1962)].

(3) Mixed boundary conditions; displacement boundary conditions on part S_1 of the boundary and traction boundary conditions on the remaining part $S - S_1$.

Initial conditions must be defined to complete the problem statement; in the body, at time t = 0,

$$u_i(\underset{\sim}{x}, 0) = \overset{o}{u}_i(\underset{\sim}{x}) \tag{2.2.27}$$

$$\dot{u}_i(\underset{\sim}{x}, 0) = \overset{o}{v}_i(\underset{\sim}{x}) \quad . \tag{2.2.28}$$

2.3 Ring Theory

The linealized theory of elasticity in the preceding sections fails to predict the buckling of a ring due to a uniform pressure on it, because the effect of compression or tension on the bending of the ring is neglected in this theory. To take into account the effect of the initial stress on the deformation of the ring, the theory of thin rods as given by Love (1922) is adapted in this study.

To establish the formulae, the bending of a curved strip out of the ring which is assumed to be inextensional is considered and the differential equations of its bending are developed.

A differential element AB of a rectangular cross section cut out ring with its center line in the horizontal plane OAB is built in at A and is bent by a load distributed in an arbitrary way along the centroid AB (Figure 2.3). If the deflections are small, the deformed shape of the bar is completely determined by the displacement of the centroid of each cross section and the rotation of each cross section about the tangent to the center line. At any cross section of the bar defined by the angle θ a system of local rectangular coordinates is taken with the origin at the centroid P and directed so that x and y coincide with the principal axes of the cross section, while z coincides with the tangent of the center line. It is assumed that initially the plane xz coincides with the plane of curvature of the bar, that the positive direction of the x axis is toward the center of the curvature, and that z is taken positive in the direction corresponding to an increase of the angle θ.

2.3.1 Kinematics

The displacement of the centroid is resolved into three components, u, v, and w in the directions of the x, y, and z axes, respectively. The

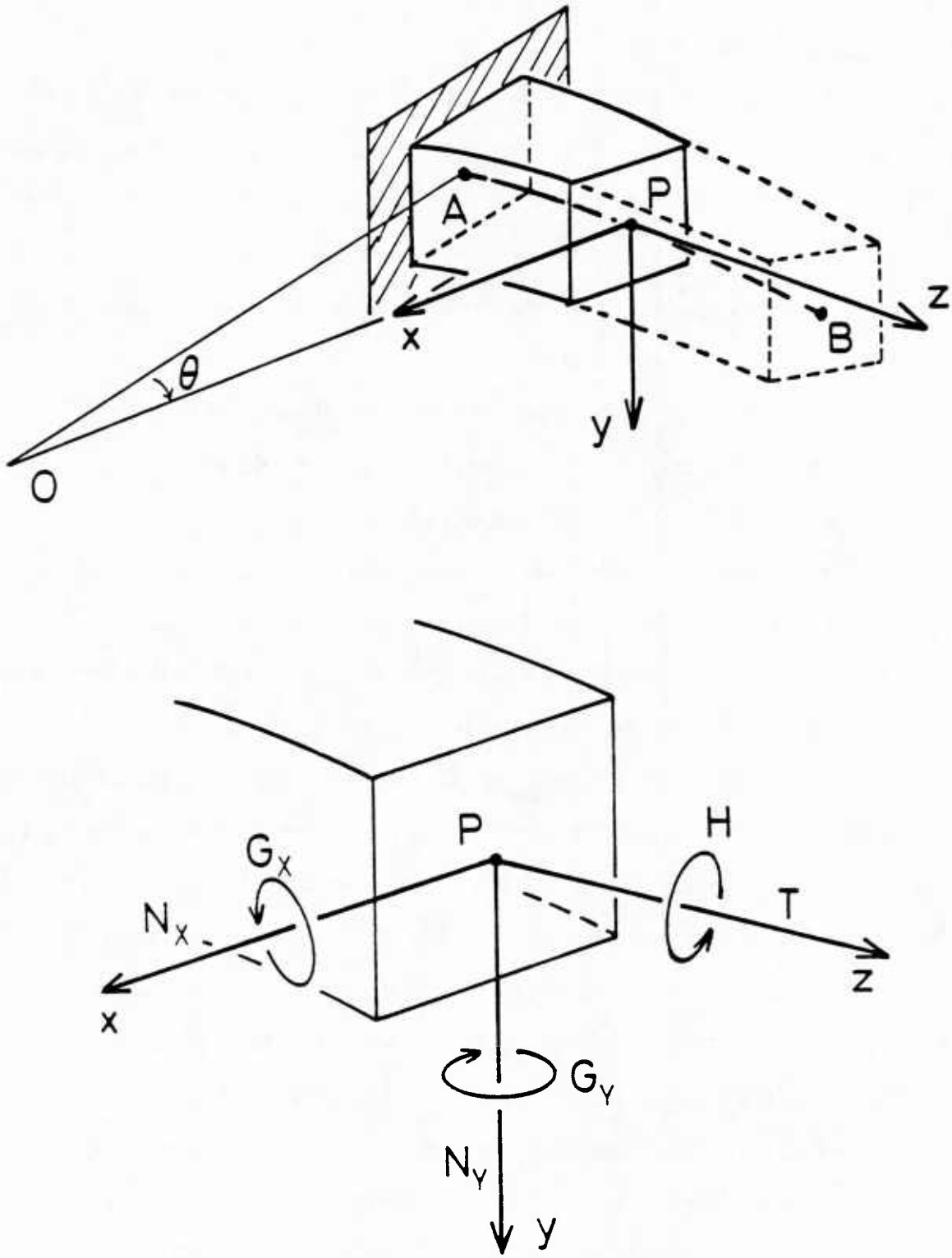

Figure 2.3 Differential element AB of a rectangular cross section cut out of the ring and orientation of the forces and moments at P

angle of rotation of the cross section about the z axis is called ϕ and is taken positive when rotation is clockwise about z axis as indicated in the figure. The deformation of an element of the ring cut out by two adjacent cross sections consists, generally, of bending in each of the two principal planes xz and yz and of twist about the z axis.

Let $\kappa_1 = 1/\rho_1$ and $\kappa_2 = 1/\rho_2$ be the curvatures of the center line at P after deformation in the principal planes xz and yz, respectively. For a circular ring the initial radii of curvature are $\rho_1 = R$ and $\rho_2 = 0$. And let τ be the angle of twist per unit length at the same point.

To obtain the differential equations for calculating displacements u, v, w and the angle ϕ, it is necessary to establish the expressions for the curvatures and the unit twist τ as functions of u, v, w and t. In the case of small displacements, one can consider separately each component of the displacements and obtain the final change in the curvature and unit twist by summing up the effects produced by the individual components.

The curvatures and twist of a ring after deformation are given, in the general case, by the following equations:

$$\kappa_1 = \frac{1}{R} + \frac{u}{R^2} + \frac{d^2u}{dz^2} \quad . \tag{2.3.1}$$

$$\kappa_2 = \frac{\phi}{R} - \frac{d^2v}{dz^2} \tag{2.3.2}$$

$$\tau = \frac{d\phi}{dz} + \frac{1}{R}\frac{dv}{dz} \quad . \tag{2.3.3}$$

Here, the condition of inextensional deformation of the ring

$$\frac{u}{R} = \frac{dw}{dz} \tag{2.3.4}$$

is included.

2.3.2 Equilibrium Equations

At the centroid P on the cross section the stresses can produce net transverse shear forces N_x, N_y as well as a tension T. The moments of the stresses about the centroid produce bending couples G_x, G_y about the x and y axes, respectively, and a twisting couple H about the centroidal z axis (Figure 2.3).

Using this notation, one can deduce two sets of equilibrium equations They are the equilibrium equations of linear momentum and of angular momentum:

$$\frac{\partial N_x}{\partial z} - N_y\tau + T\kappa_1 + f_x = m\frac{\partial^2 u_x}{\partial t^2} \tag{2.3.5}$$

$$\frac{\partial N_y}{\partial z} - T\kappa_2 + N_x\tau + f_y = m\frac{\partial^2 u_y}{\partial t^2} \tag{2.3.6}$$

$$\frac{\partial T}{\partial z} - N_x\kappa_1 + N_y\kappa_2 + f_z = m\frac{\partial^2 u_z}{\partial t^2} \tag{2.3.7}$$

$$\frac{\partial G_x}{\partial z} - G_y\tau + H\kappa_1 - N_y + c_x = 0 \tag{2.3.8}$$

$$\frac{\partial G_y}{\partial z} - H\kappa_2 + G_x\tau + N_x + c_y = 0 \tag{2.3.9}$$

$$\frac{\partial H}{\partial z} - G_x\kappa_1 + G_y\kappa_2 + c_z = 0 \tag{2.3.10}$$

In the above equations, $\underset{\sim}{c}$ represents an applied body couple and $\underset{\sim}{f}$ the body force. The magnetic body couple on the current carrying medium in the magnetic field is expressed as

$$\underset{\sim}{c}_{mag.} = \int_A r \times (\underset{\sim}{J} \times \underset{\sim}{B})\, da \quad . \tag{2.3.11}$$

Therefore, if the magnetic field or current is presumed to be distributed uniformly, then the couple may be neglected. Also diamagnetic effects and twisting of the filaments in the superconductor can lead to a nonzero body couple but are neglected here and $\underset{\sim}{c}$ is set to be zero.

In the analysis of the current carrying conductors under mechanical constraints, the body force is the Lorentz force. The mechanical constraints due to the springs connected to the ring are also treated as body force in this study. The electromagnetic body force is the integral of the Lorentz force over the cross sectional area:

$$\underset{\sim}{f}_{mag.} = \int_A \underset{\sim}{J} \times (\underset{\sim}{B}^0 + \underset{\sim}{B}^1)\, da \tag{2.3.12}$$

where $\underset{\sim}{B}^0$ is due to external source and B^1 is the self field. The mechanical stiffness is expressed in terms of the displacements as

$$\underset{\sim}{f}_{mech.} = -\underset{\approx}{k} \cdot \underset{\sim}{u} \tag{2.3.13}$$

where the $\underset{\approx}{k}$ is the mechanical stiffness tensor. In this study, $\underset{\approx}{k}$ is assumed to be diagonal. Then the total body force per unit length is

$$\underset{\sim}{f} = \int_A \underset{\sim}{J} \times (\underset{\sim}{B}^0 + \underset{\sim}{B}^1) - \underset{\approx}{k}\, \underset{\sim}{u} \quad . \tag{2.3.14}$$

2.3.3 Constitutive Equations

To complete this set of equations one requires a relation between the bending and twisting moments G_x, G_y, H and the deformation. They are

$$G_x = A\kappa_2 \tag{2.3.15}$$

$$G_y = D(\kappa_1 - \frac{1}{R}) \tag{2.3.16}$$

$$H = C\,\tau \quad . \tag{2.3.17}$$

$A = EI_x$ and $D = EI_y$ are the two principal flexural rigidities or bending stiffness and C represents the torsional rigidity of the ring. E is the Young's modulus and I_x and I_y are the moments of inertia about x and y axes, respectively.

2.3.4 <u>In-Plane Deformation</u>

For this case one can set $v = \phi = 0$. Also, it follows that $N_y = G_x = H = 0$. Therefore, there are five unknowns: u, w, N_x, N_z and G_y. The corresponding five differential equations are:

(equilibrium equations)

$$\frac{\partial N_x}{\partial z} + T\kappa_1 + f_x = m\frac{\partial^2 u}{\partial t^2} \tag{2.3.18}$$

$$\frac{\partial T}{\partial z} - N_x\kappa_1 + f_z = m\frac{\partial^2 w}{\partial t^2} \tag{2.3.19}$$

$$\frac{\partial G_y}{\partial z} + N_x = 0 \tag{2.3.20}$$

(constitutive equation)

$$G_y = EI_y(\kappa_1 - \frac{1}{R}) \tag{2.3.21}$$

$$= EI_y\left(\frac{u}{R^2} + \frac{\partial^2 u}{\partial z^2}\right) \tag{2.3.22}$$

(compatibility equation)

$$\frac{\partial w}{\partial z} = \frac{u}{R} \quad . \tag{2.3.23}$$

The equation of in-plane motion of a ring or multi-rings will be derived later in Chapter 4.

2.3.5 Out-of-Plane Deformation

In this case one can assume $u = f_x = f_z = 0$. Also, it can be shown $w = N_x = G_y = 0$. Therefore, there are the following five differential equations for the five unknowns: v, ϕ, N_y, G_x and G_z.

(equilibrium equations)

$$\frac{\partial N_y}{\partial z} - T\kappa_2 + f_y = m\frac{\partial^2 v}{\partial t^2} \tag{2.3.24}$$

$$\frac{\partial G_x}{\partial z} + \frac{H}{R} - N_y = 0 \tag{2.3.25}$$

$$\frac{\partial H}{\partial z} - \frac{G_x}{R} = 0 \tag{2.3.26}$$

(constitutive equations and kinematic equations)

$$G_x = A\kappa_2 = A\left(\frac{\phi}{R} - \frac{\partial^2 v}{\partial z^2}\right) \tag{2.3.27}$$

$$H = C\,\tau = C\left(\frac{\partial \phi}{\partial z} + \frac{1}{R}\frac{\partial v}{\partial z}\right) \quad . \tag{2.3.28}$$

The equation of out-of-plane motion of a ring can be derived by using the same technique adapted for the in-plane motion, but will not be discussed further in this study.

CHAPTER 3

EXPERIMENT

3.1 Buckling and Vibration of Superconducting Rings

3.1.1 Purpose

While the superconducting magnet produces a high magnetic field, each current carrying element is exposed to the magnetic field produced by the magnet itself, which consequently causes a high magnetic force on it. If any vibration or buckling occurred in the real size magnet, it could cause a quench of the system, or in the worst case, a collapse of the magnet.

The superconducting magnet system has a complex structure as shown in Figures 1.5 and 3.1. The coil pack is made up of alternate layers of superconductor and insulator. According to the MFTF magnet design [Horvath (1980)], the transverse stiffness is quite soft as compared to the circumferential stiffness. The first purpose of this experiment is to make a simplified and generalized model of superconducting magnets which includes the characteristics mentioned above, and to observe the existence of the buckling and the change of the natural frequencies due to the conduction currents. The effect of the difference of the stiffness in the transverse and circumferential directions will be verified also.

Moreover, it is quite important to develop an analytical method to simulate the inner vibration and buckling of multi-layered solenoidal

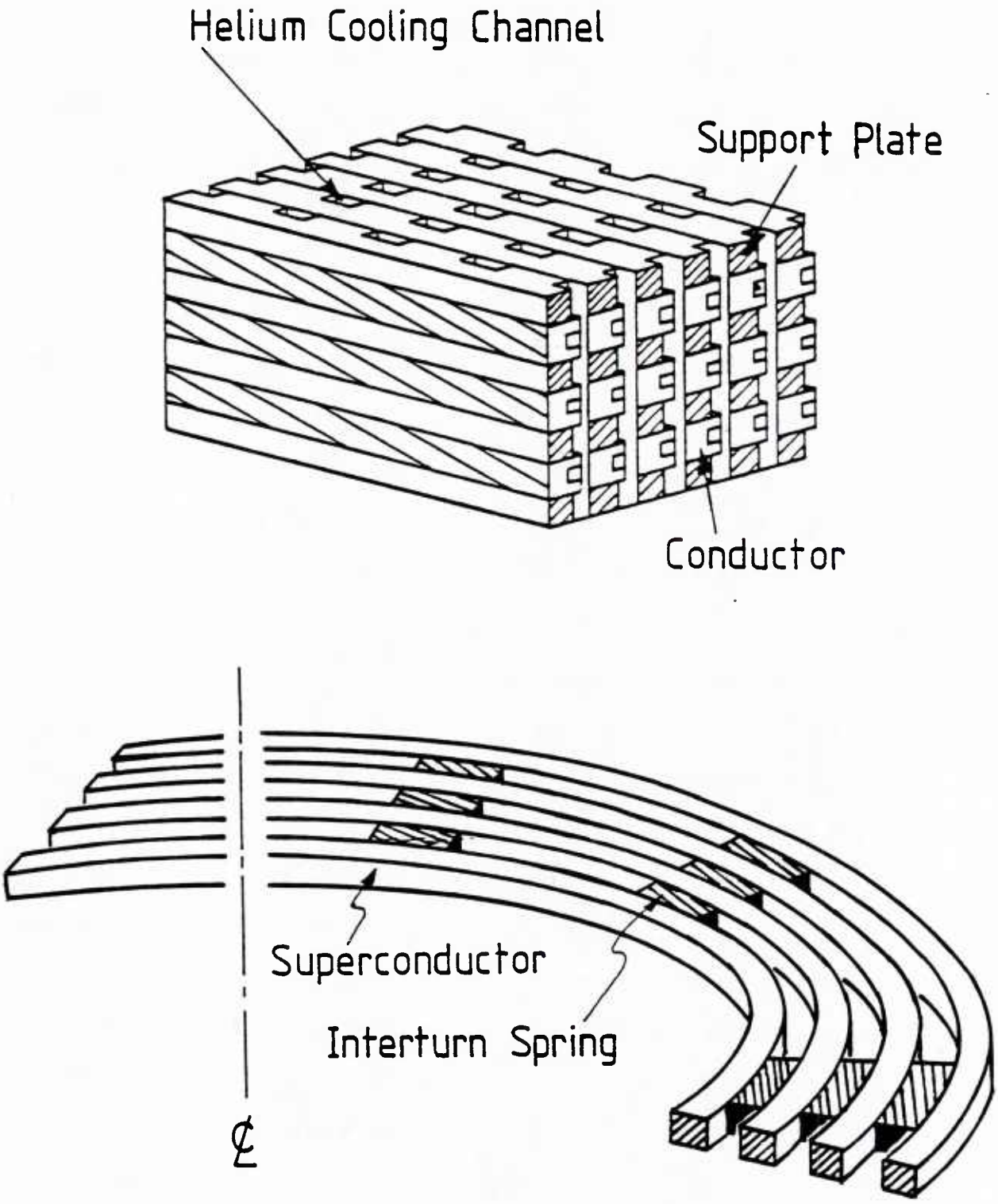

Figure 3.1 Internal structure of superconducting solenoid magnets and experimental model

magnets. It is the second aim of this experiment to obtain the natural frequencies for various currents and the critical buckling currents in the modeled system in order to verify the analytical method. The verified analytical method will be applicable to the real size magnets.

3.1.2 Experimental Model

As shown in Figure 3.1, the typical coil pack for superconducting magnets consists of layers of superconductors separated by perforated insulation. The perforation is for the liquid helium path for the cooling of the system. The pack is placed in the structural jacket.

Any superconducting magnet has multi-layers of superconductors in the radial direction with multi-turns in each layer. The numbers of the layers and turns depend on the size and performance of the magnet.

Although the actual magnet is a three-dimensional structure, a two-dimensional analysis is adapted in this study. So, here we consider a pancake type magnet which has multi-layers in the radial direction but only one turn in the axial direction. To retain some of the structural details of the conductor and insulation, a concentric ring model is used.

In this model, the helical winding of the pancake magnet is replaced by a series of concentric rings. Each ring is connected to neighboring rings by mechanical springs which attempt to simulate the insulation with soft stiffness (Figure 3.1). It is reported by Horvath (1980) that the compressive response of the superconductor coil pack exhibited soft elastic behavior for low pressure followed by a stiff linear behavior (high modulus) for higher pressure.

The rings were made of NbTi superconductor and the experiments were conducted in liquid helium. This superconductor was chosen because of its high current density and small cross section. To enhance the magnetic

field on the rings the ambient field coils were made and placed inside the rings to simulate the inner layers of the pancake magnets.

Four different models were used to measure the change of frequencies due to the conduction currents (dynamic test) and the critical buckling currents (static test).

1) One-ring model without springs: In this model a superconducting ring of radius 11 cm was placed around a 100 turn ambient field coil of mean radius 10 cm in the same plane. The ring was supported by two pins on opposite sides of the ring to prevent any rigid body motion. The schematic view is given in Figure 3.2.

2) One-ring model with springs: The ambient field coils and the ring have the same specifications as above. However, they were connected to each other by 16 equally placed brass shim springs.

3) Two-ring model with springs: Two rings of radii 11 and 12 cm were placed around the same ambient field coil and supported by two pins. Each space between the rings and between the ambient field coil and 11 cm ring had 16 brass shim springs.

4) Three-ring model with springs: In this model three rings of radii 11, 12 and 13 cm were used. The top view is shown in Figure 3.2, too.

In each experiment, the current directions in the rings and ambient field coil were the same so that the rings had the inward body forces. The experimental structure with structural platform is shown in Figures 3.3 and 3.4. Three experiments were conducted at the same time to save expensive liquid helium. In these pictures, they are one ring model without springs, two ring model and three ring model from the top, respectively.

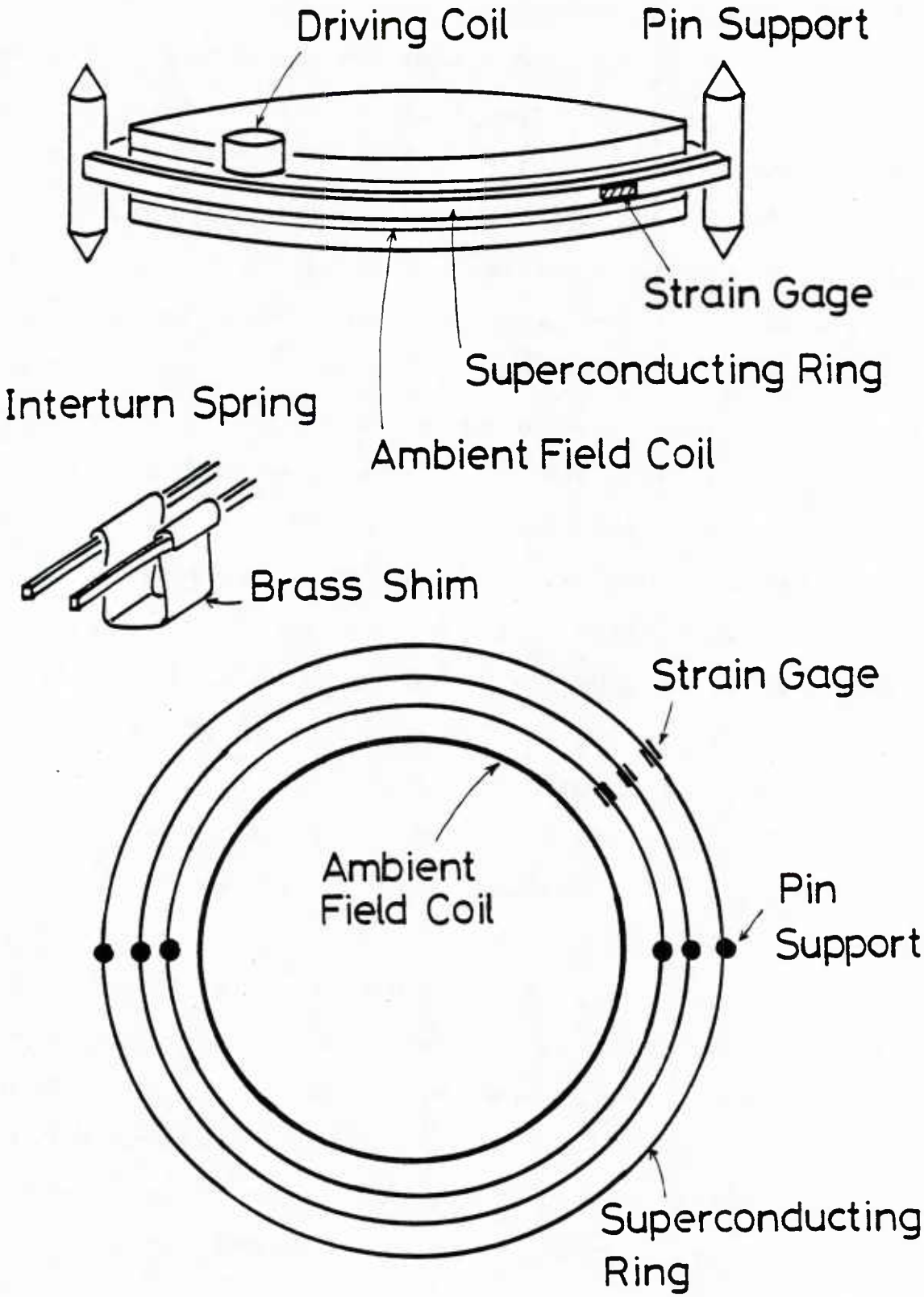

Figure 3.2 Schematic of one-ring model experiment and top view of three-ring experiment

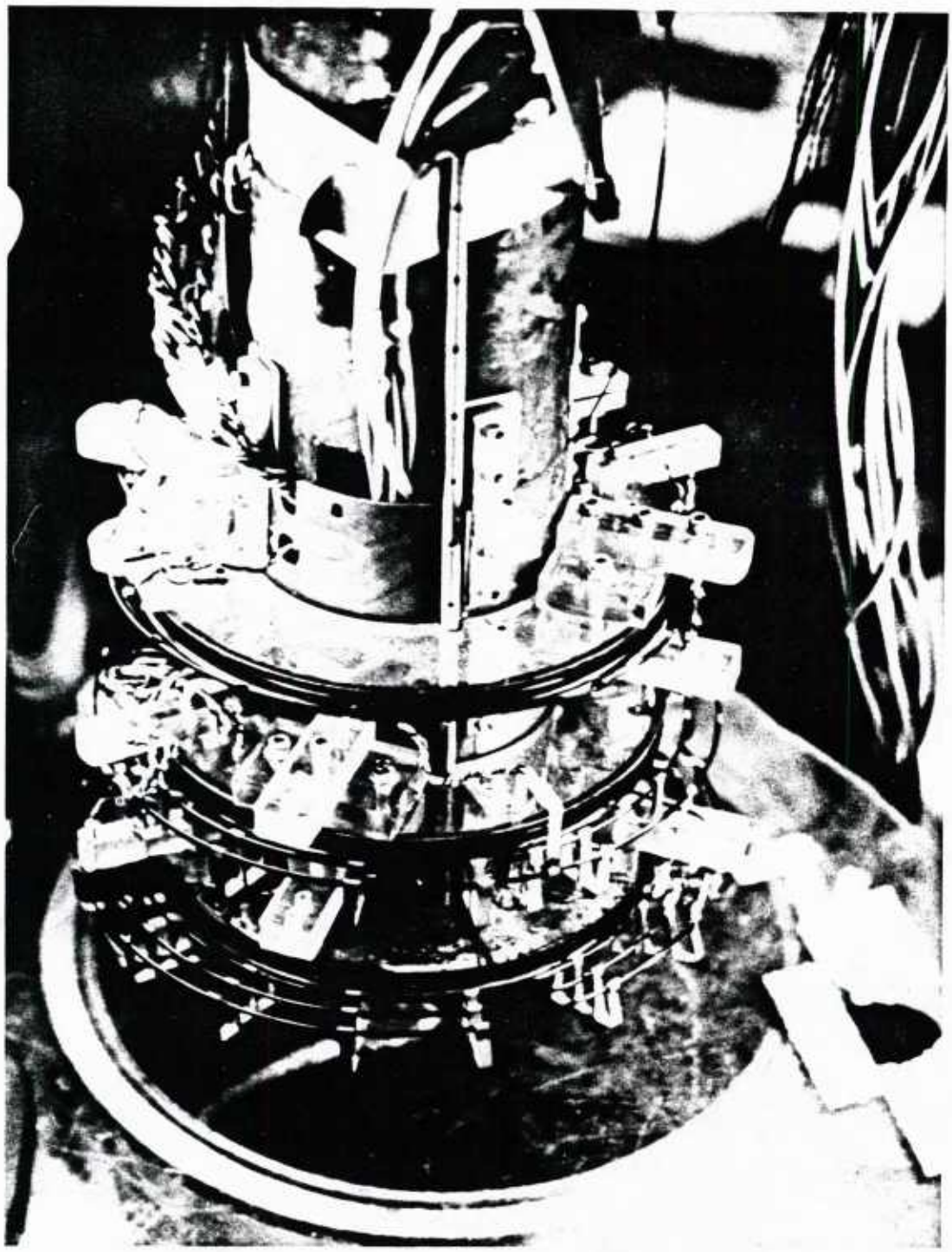

Figure 3.3 Experimental apparatus for one-ring, two-ring, and three-ring experiments

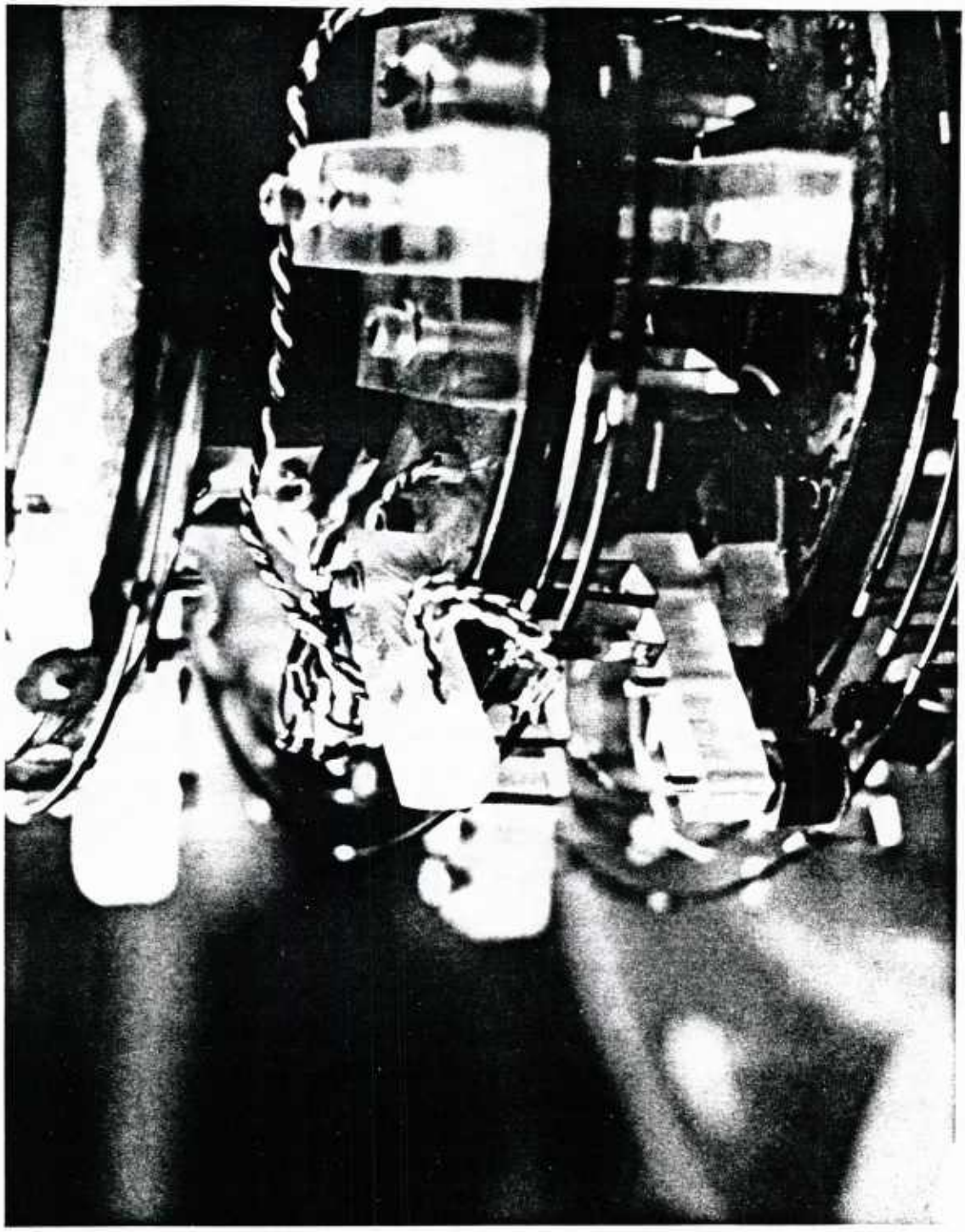

Figure 3.4 Close up of experimental apparatus showing interturn springs, strain gauges, and driving coils

3.1.3 Experimental Apparatus

The experimental apparatus consists of superconducting rings, an ambient field coil, springs, a driving coil, cryostat, an electric power supply and measurement system.

Superconducting Rings

The rings were made by NbTi superconducting wire. It was 2040 NbTi filaments molded in copper stabilizer with a copper/NbTi ratio of 1.8. The wire is insulated by formvar. Its cross section is 1 mm x 2 mm and the moment of inertia about the in-plane bending is 1.67 x 10^{-13} m^4. The mass density is 0.017 kg/m^3.

The Young's modulus was measured by a tensile test at room temperature to be 88.2 MPa. Though the Young's moduli of most materials tend to increase several percent in liquid helium temperature, this value was used throughout the analysis in this study.

The pin supports of each ring were made of stainless steel. At one end the support worked as a clamp to keep the wire in a circular ring. Because of the overlap at this end, the actual radius of the ring differs ±1 mm around this clamp.

Ambient Field Coil

The ambient field coil was made by 0.38 mm diameter NbTi superconducting wire. This wire was wound in 100 turns over the groove carved on the edge of a circular polycarbonate (Lexan) plate. The coil was potted in epoxy resin to prevent any motion due to Lorentz forces. Though the ambient field coil has finite dimensions (mean radius: 10 cm, thickness: 4 mm and height: 8 mm), in this analysis it was considered to

be a one turn ring of radius 10 cm with a hundred times more current than in the ring.

Brass Shim Springs

These springs were made by the 0.2 mm thickness brass shim, because brass is nonferromagnetic and not affected by the magnetic field. They are U-shaped and can be seen in Figure 3.4.

The spring constant of each spring in the radial direction (opening mode of the spring) is measured to be 170 N/m. This value was verified by frame analysis. Although in the experiment 16 springs were discretely placed, they were treated as a uniform elastic spacer of spring constant 4100 N/m^2 in the analysis.

The spring constant in the circumferential direction, which is the shearing mode of the spring, is 295 N/m in each spring, and 7150 N/m^2 as a uniform spacer. The springs were designed to simulate the soft transverse stiffness of helically wound coils.

Driving Coil

This coil is also called a magnetic shaker, and used to measure the resonance frequencies. This coil was wound from a copper wire of size #30. It has 300 turns and potted in epoxy resin. The mean radius is 5 mm and the height is 12 mm. The driving coils were placed just over each ring (Figure 3.4) to give sinusoidal perturbation of the vertical magnetic field. The input was provided by a frequency generator through an amplifier. The amplifier used in this experiment, however, had poor gain for frequencies lower than 50 Hz, and we had difficulty measuring the resonance in that range.

Cryostat

The experiments must be performed in a pool of liquid helium to obtain superconductivity. A schematic drawing of the cryostat used as a liquid helium dewar is shown in Figure 3.5. In order to prevent heat leaks, the cryostat has a carefully considered structure.

The insulated space between the inner cylindrical liquid helium dewar and the outer cylindrical dewar is kept at a high vacuum. Moreover, a liquid nitrogen reservoir surrounds the liquid helium dewar. The inner cylindrical dewar and liquid nitrogen reservoir are laminated several times with super insulators made of evaporated aluminum mylar to prevent heat radiation into the inner dewar.

To fill the dewar with liquid helium, the inner vessel was precooled to 78°K with liquid nitrogen. After the LN_2 is removed, liquid helium was transferred from a storage dewar to the test dewar via a vacuum-jacketed transfer tube. About 60 liter of liquid helium was necessary to perform the experiment.

During the experiment, heat leak and a subsequent loss of helium is inevitable. The main sources are heat conduction and radiation. To prevent heat conduction, a glass fiber wound-epoxy cylindrical tube was used as a structural support platform for test models. Also vapor-cooled current leads were used to minimize the heat leak through the leads. Styrofoam with a heat reflecting metal plate was used to minimize the heat radiation.

3.1.4 Measurement System

The measurement system consisted of strain gauges and amplifier, a current meter and a helium meter. In dynamic tests, the frequencies

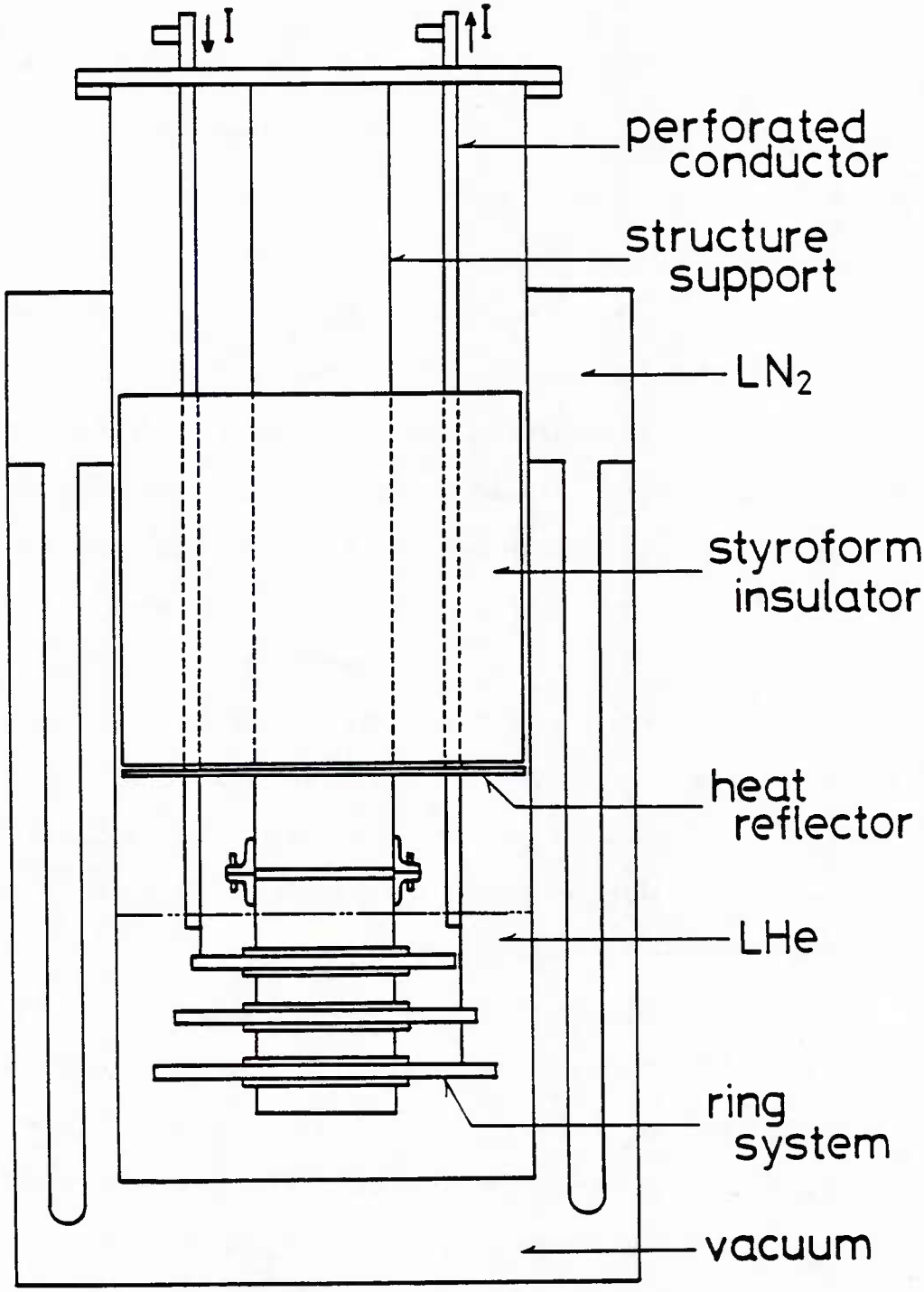

Figure 3.5 Cut away diagram of experimental set up

of the driving coil was measured by a pulse counter. The diagram of the system is shown in Figure 3.6.

Strain Gauges

The bending deformation of the rings were measured by foil strain gauges. The gauge for low temperature (WK-06-062AP-350 by Micro Measurement) was chosen. The gauge position was at 45° from one of the pins, where it was supposed to have the largest deformation for the lowest bending mode. Two gauges were attached directly on both sides of each superconducting ring after its coating was scraped off (Figure 3.4). The used glue was two-component, solvent-thinned epoxy-phenolic adhesive (M-bond 610 by the same company).

Since the actual bending strain was not the focus of this experiment, the gauge output was not calibrated. Miya and Takagi (1980) reported that the gauge factor of the similar gauges increased about 4% at liquid helium temperature. Also, Walstrom (1975) reported that the effect of magnetoresistivity on the gauge output is not significant if the magnetic field is less than one tesla. In this experiment, however, the two gauge method was adapted and the difference of the change strain gauges was measured through a differential high gain amplifier in order to cancel out these effects if there were any.

Current Meter

The current conducted through the system was measured by a current meter which uses a non-contact probe. This probe consists of a magnetic core and a hall generator, and measures the magnetic field around the current. The magnetic field is then converted to a current using Ampere's Law.

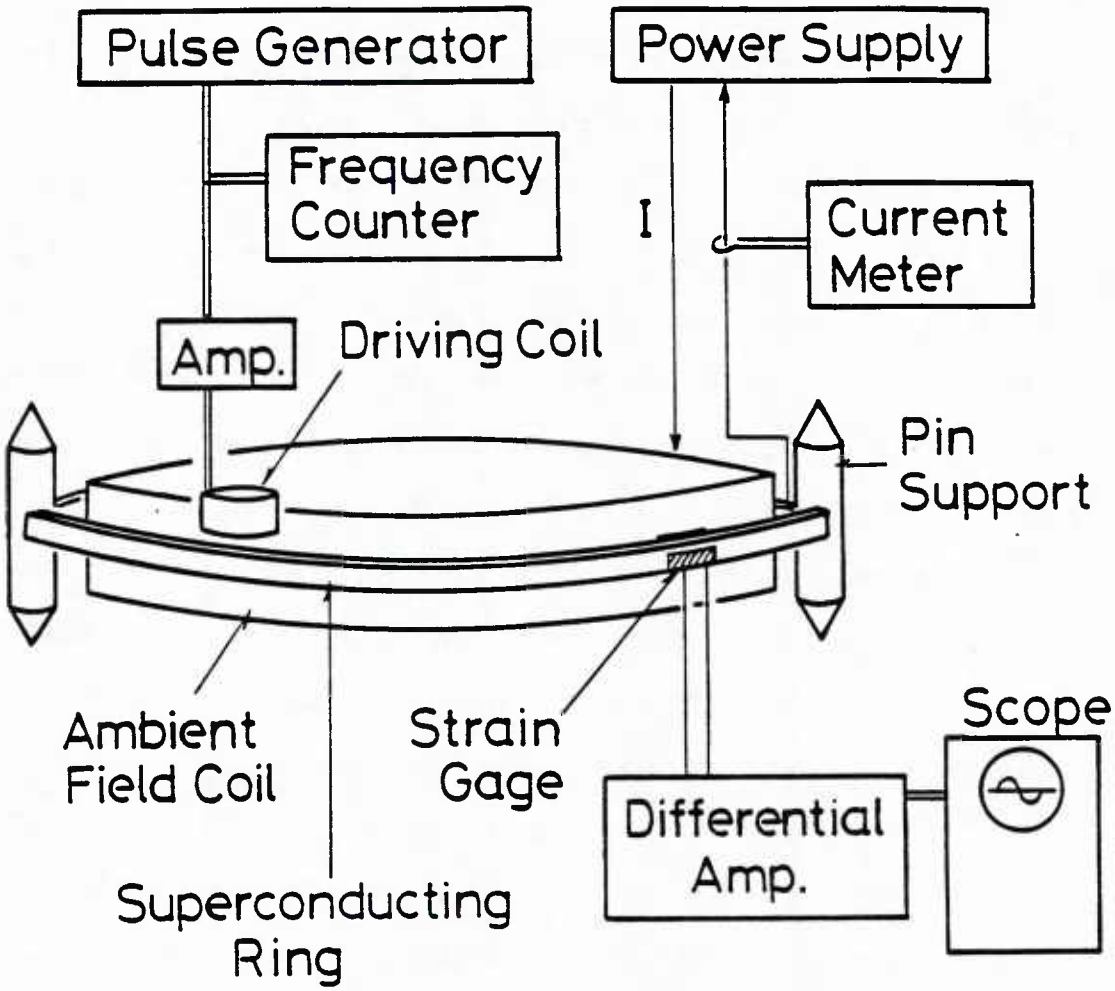

Figure 3.6 Electrical power and data collection system

Helium Meter

To assure that the rings were covered by liquid helium, a helium meter was used to measure the liquid helium surface. The probe of this meter is made by a NbTi superconductor and the change of its resistance was indicated as the change of the helium surface.

3.1.5 Procedure

The experiments were performed through the following sequence:

1) Manufacturing rings and coils
2) Strain gauge attachment
3) Assemblage of the system
4) Connection of the leads
5) Pre-cooling of cryostat by LN_2
6) Pump out the LN_2 cooled N_2 gas
7) Pour in LHe into cryostat
8) Measurement.

Since initial distortion can cause an error in the buckling experiment, great attention was paid to the assemblage of the system. If the experiment assemblage is too close to the helium tank wall or the LN_2 for precooling is not removed fast enough, the remaining LN_2 can turn into an ice bridge which causes a large heat leak when LHe is poured in through the transfer tube. This causes evaporation of LHe and one is unable to obtain a LHe pool for the experiment. Careful attention must be paid in this procedure.

After it was confirmed that LHe covered the whole system, the following two tests were conducted for each ring model.

Static Test

In this test the bending strain was measured as the current was increased. Near the buckling current the bending became large which indicated possible magnetoelastic buckling of the rings.

Dynamic Test

The natural frequencies of the rings were measured as the current was increased. By changing the frequency of the perturbating magnetic field by the driving coil, the resonance frequencies of the rings were obtained for different currents conducted through each model.

3.1.6 Experimental Result

The experimental results are shown in Figures 3.7-3.17. They are divided into four groups as mentioned in section 3.1.2. Each group has two different test results; static and dynamic.

Static Test: In this test the static bending strain of the ring was measured as a function of the current. This measurement is sensitive to misalignments and imperfections of the system. Since magnetoelastic buckling is similar to Euler buckling, there should be a distinctive deflection vs. force curve, which has a large deflection near the critical buckling force. For each static result, the bending strains were plotted against the current squared, which is proportional to the magnetic force. The other method, particularly when misalignments or imperfections are significant, is a Southwell plot [Southwell (1932)]. In this method the current-deformation relation is approximated by the equation

$$\delta(I^2 - I_c^2) = k \qquad (3.1.1)$$

or

$$\delta = I_c^2 \frac{\delta}{I^2} + \frac{k}{I^2} \tag{3.1.2}$$

where I_c is the critical buckling current and k is a constant. If the deflection δ is plotted against δ/I^2, then the slope of this line is the square of the critical current.

Dynamic Test: The frequency-current dispersion relations were obtained experimentally in this test. When the current in the system is less than a critical buckling value, the total stiffness in the system is softened or stiffened as the current changes. When the softening occurs, the natural frequency decreases as the current increases. In the linear analysis this is shown as

$$\omega_n^2 = \omega_{on}^2 \left(1 - \frac{I^2}{I_o^2}\right) \tag{3.1.3}$$

where ω_{on} is the frequency of the nth mode with zero magnetic coupling in the system. The negative sign is replaced by a positive sign when the system stiffness hardens. Therefore, ω_n/ω_{on}^2 was plotted against I^2 in this experiment. Then the experimental buckling currents were obtained from the slopes of the curves.

One Ring Model Without Springs

The force vs. deflection curves obtained from the static test are shown in Figure 3.7. The different curves were obtained from a series of two experiments. Because of the imperfections and misalignments of the system, the curves do not indicate a sharp buckling. A

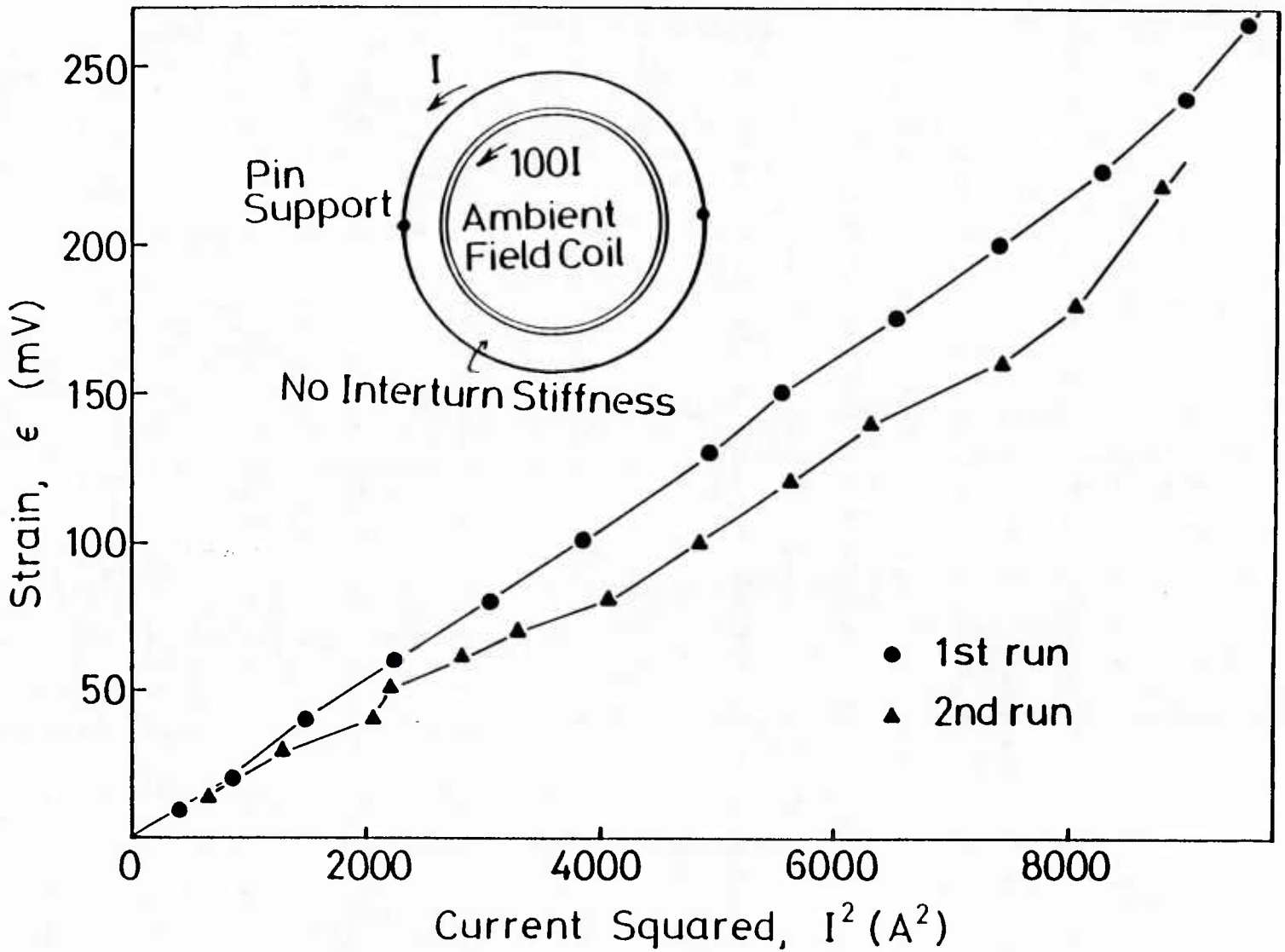

Figure 3.7 Experimental strain vs. current squared (proportional to magnetic force) curves for one-ring model without interturn springs

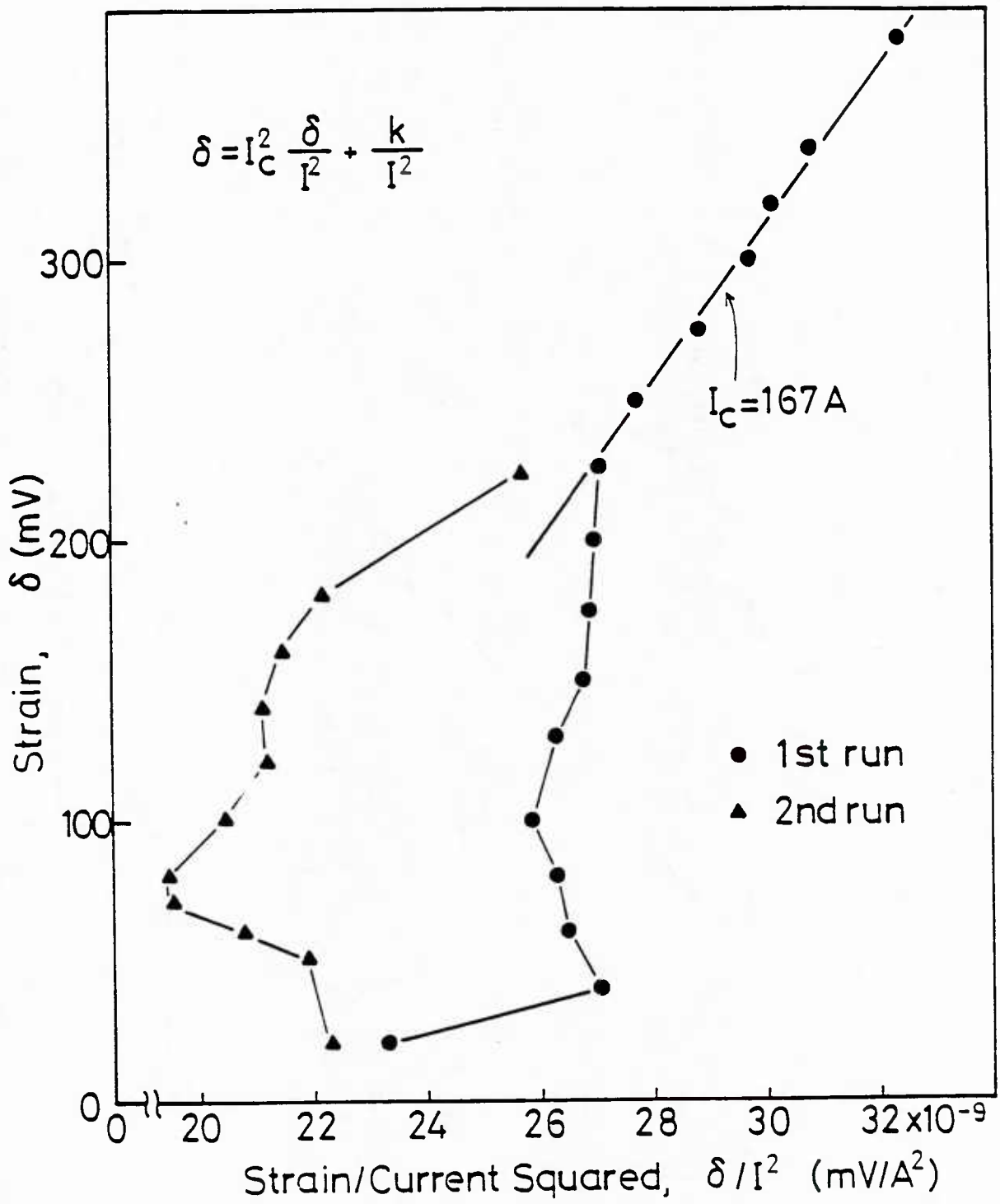

Figure 3.8 Southwell plot of static data for one-ring model without interturn springs

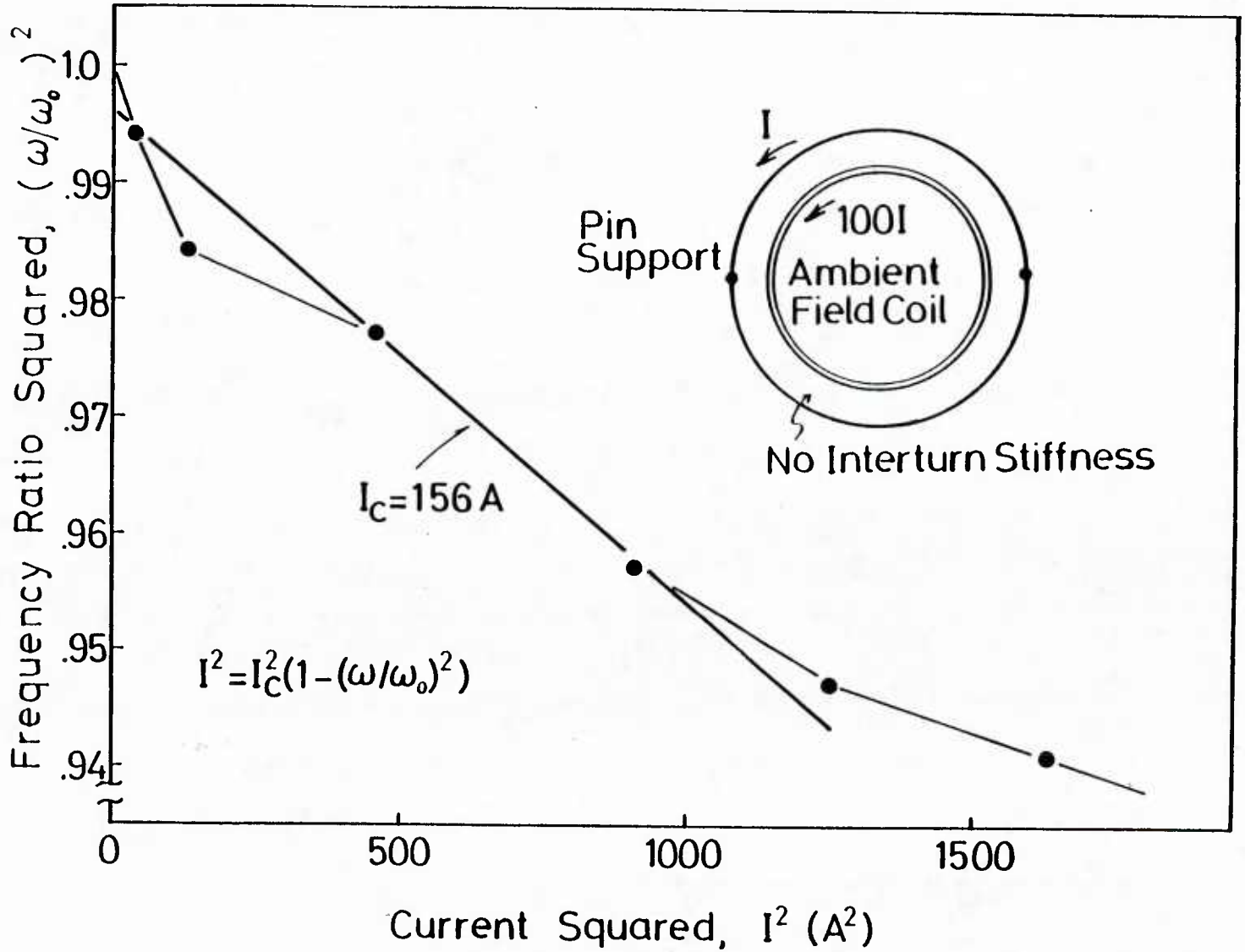

Figure 3.9 Experimental current - frequency dispersion curve for one-ring model without interturn springs

buckling current of 167 A was obtained from the Southwell plot (Figure 3.8).

The results of the dynamic test is shown in Figure 3.9. Only the resonance around the natural frequency 80 Hz was obtained in the experiment, though the natural frequencies of 38 and 80 Hz were obtained by the free vibration test in the room temperature. The two frequencies correspond to the second and third circumferential modes, respectively. The pictures of these circumferential modes are drawn in Figures 3.8 and 3.9. The reason the resonance around 39 Hz could not be observed is thought to be because the perturbed magnetic field was not large enough due to the characteristic of the frequency amplifier used. The critical buckling current obtained from this experiment was 156 A and close to the value from the static test.

One-Ring Model With Springs

Figure 3.10 shows the relationship between the deflection and the applied force or current squared. In this case, too, no significant buckling curve was observed. The Southwell plot from these data is given in Figure 3.11. There are observed two slopes in this graph. They represent two different critical buckling currents, 159 A and 225 A. Since 16 springs were placed between the ring and the ambient field coil, they correspond to the second and fourth radial modes, respectively. The pictures of these radial modes are drawn in Figure 3.11. The comparison between these experimental values and the theoretical values is given in the later chapter.

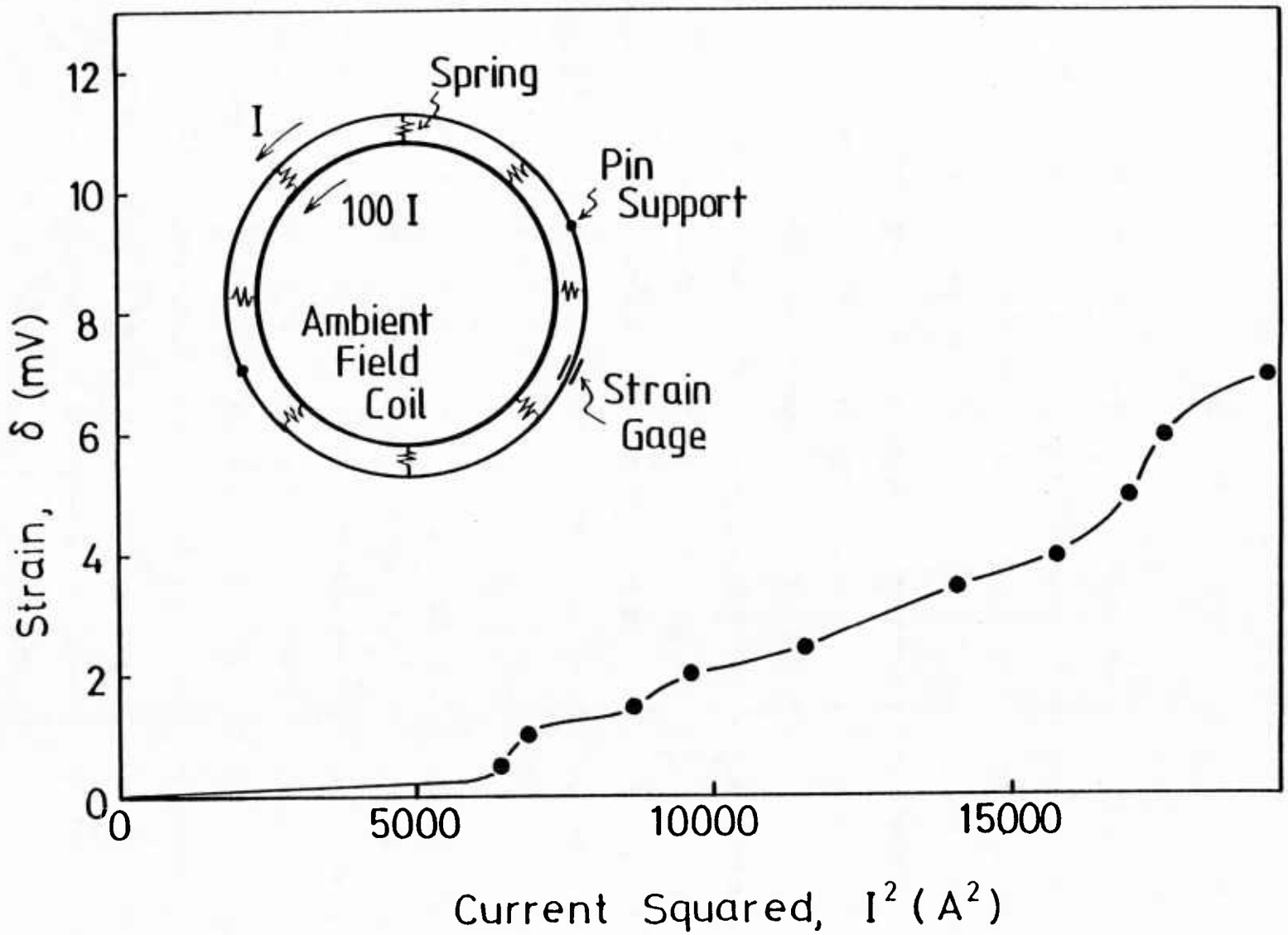

Figure 3.10 Experimental strain vs. current squared curve for one-ring model with interturn springs

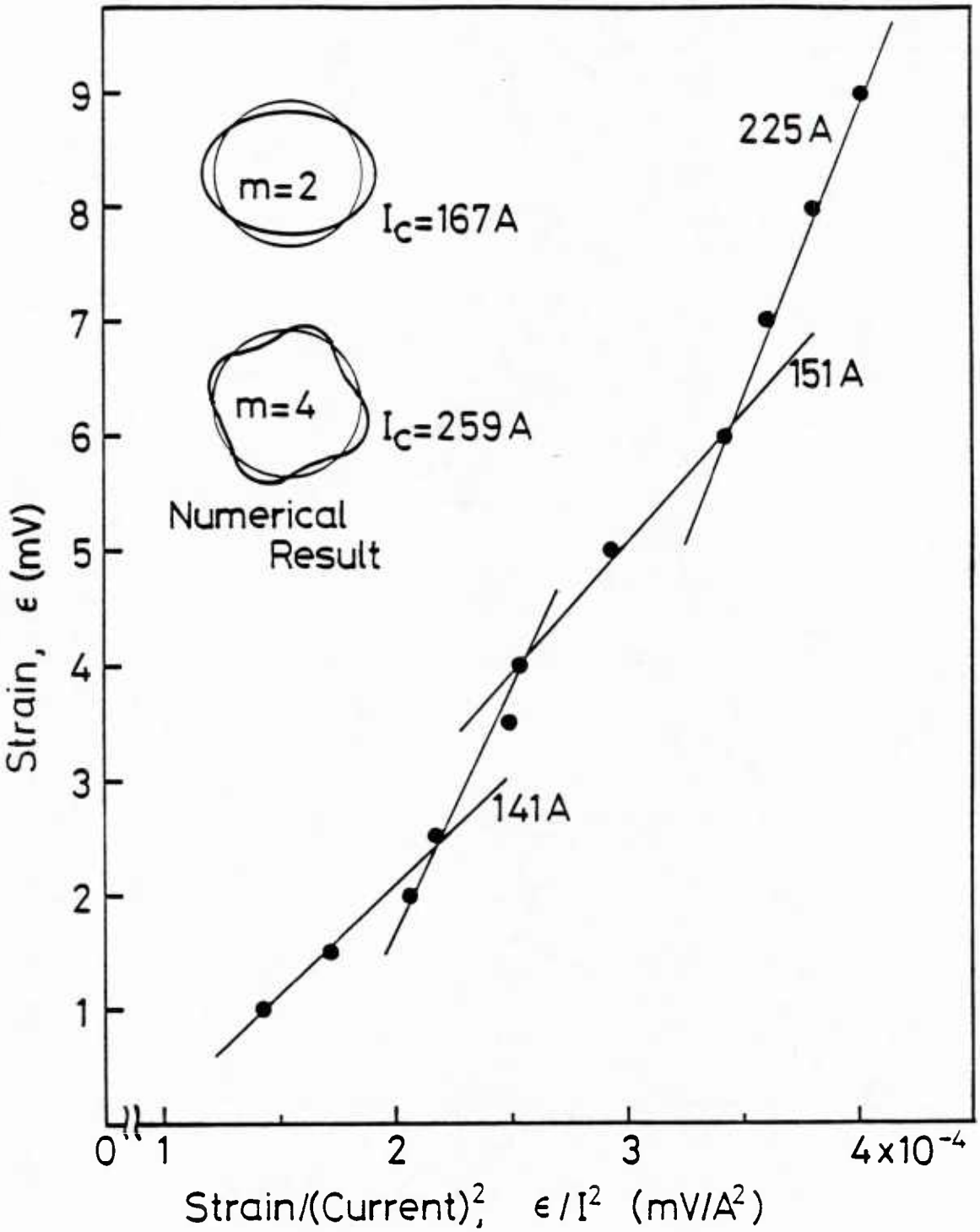

Figure 3.11 Southwell plot of static data for one-ring model with interturn springs

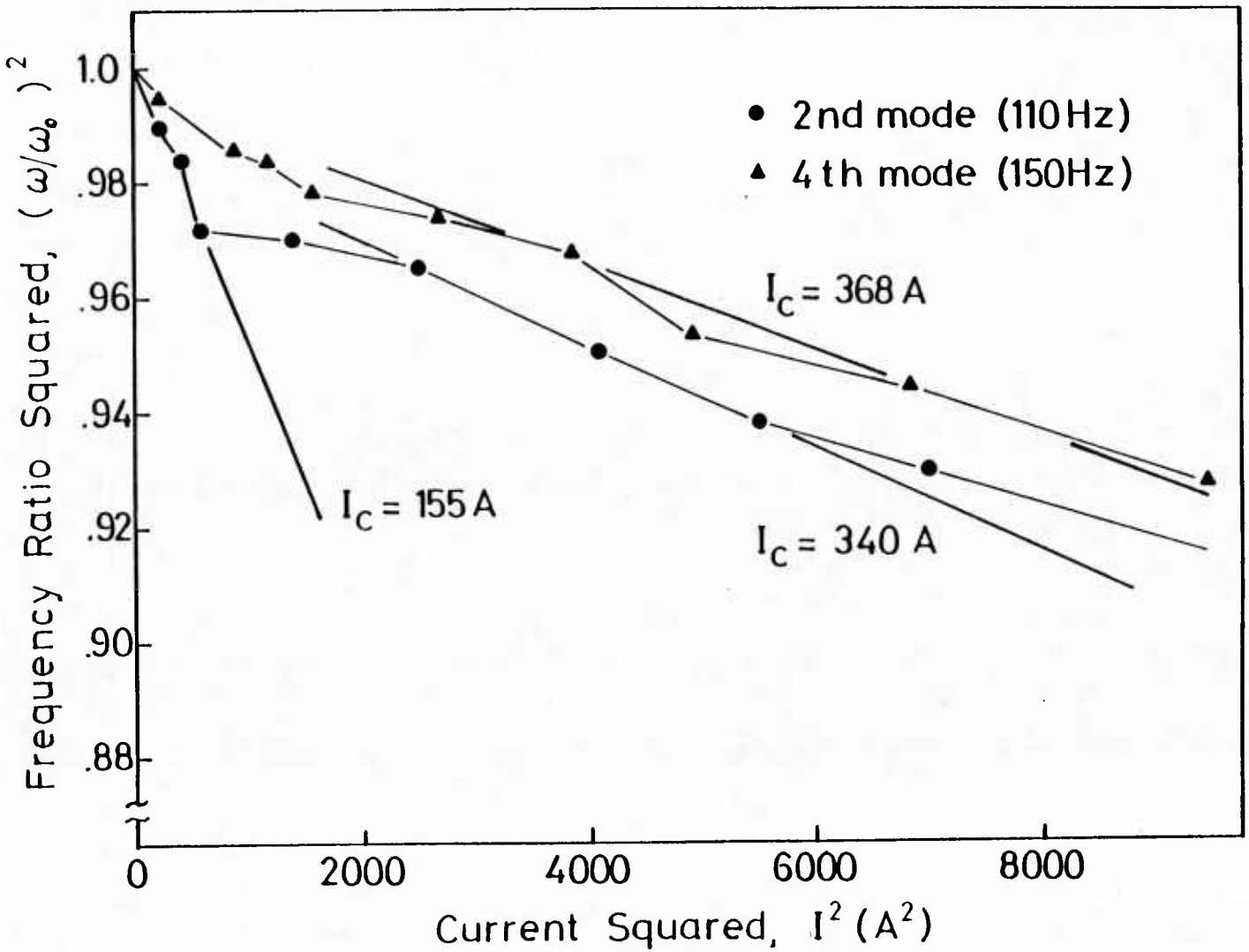

Figure 3.12 Experimental current - frequency dispersion curves for one-ring model with interturn springs

The frequency-current dispersion curves are shown in Figure 3.12. Two different circumferential modes, which have natural frequencies of 110 and 150 Hz, were observed here. The decrease in the natural frequency with the increase in the increase in the current shows the relaxation of the stiffness due to the magnetic field.

Two-Ring Model

The bending deflections of both the inner and outer rings were measured as a function of the current. In the deflection-force curves shown in Figure 3.13, circles and triangles represent the bending of the inner and outer rings, respectively. The typical curves, which are the increase of the deflection as the current increases, were obtained. Both rings bent in the same direction. Interestingly, the deflection of the outer ring was larger than that of the inner ring, though the magnetic field applied on it was smaller. It is considered that there was a lateral deformation in the inner ring, since the deflection here was smaller compared to that of the three ring experiment. The sharp buckling was not observed, and the Southwell plot did not have any significant slope, or the plotted points were scattered.

The result of the dynamic data is given in Figure 3.14. Three natural frequencies were obtained for different circumferential or radial modes. The curves corresponding to the frequencies 70 and 130 Hz showed the destabilization. In these cases both rings moved or bent in the same direction, which is defined as the first radial mode. In this mode the two rings behave as a single mass. On the other hand, the third mode showed the stabilization, in which the frequency increased as the current increased. Contrary to the

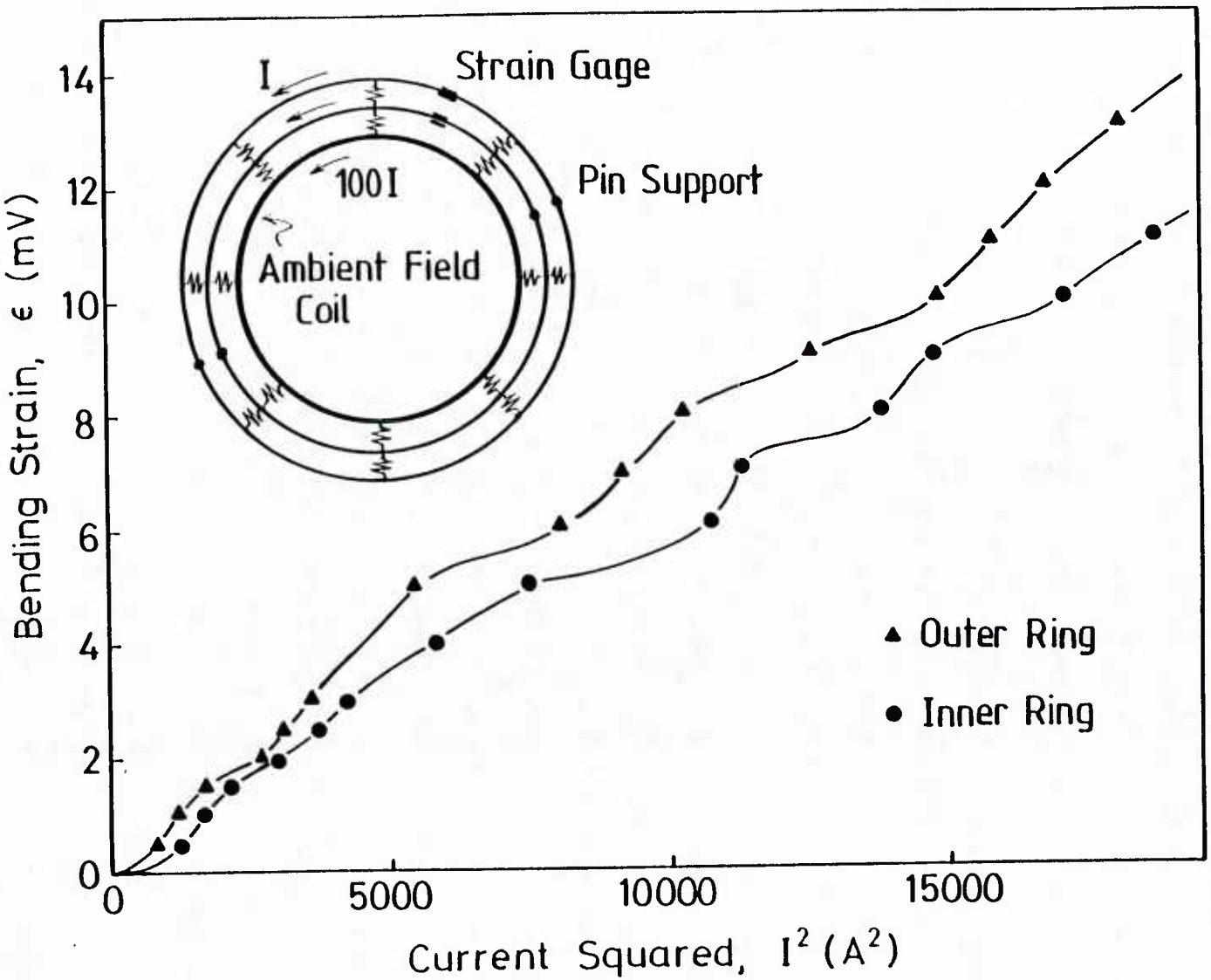

Figure 3.13 Experimental strain vs. current squared (proportional to magnetic force) curves for two-ring model with interturn springs

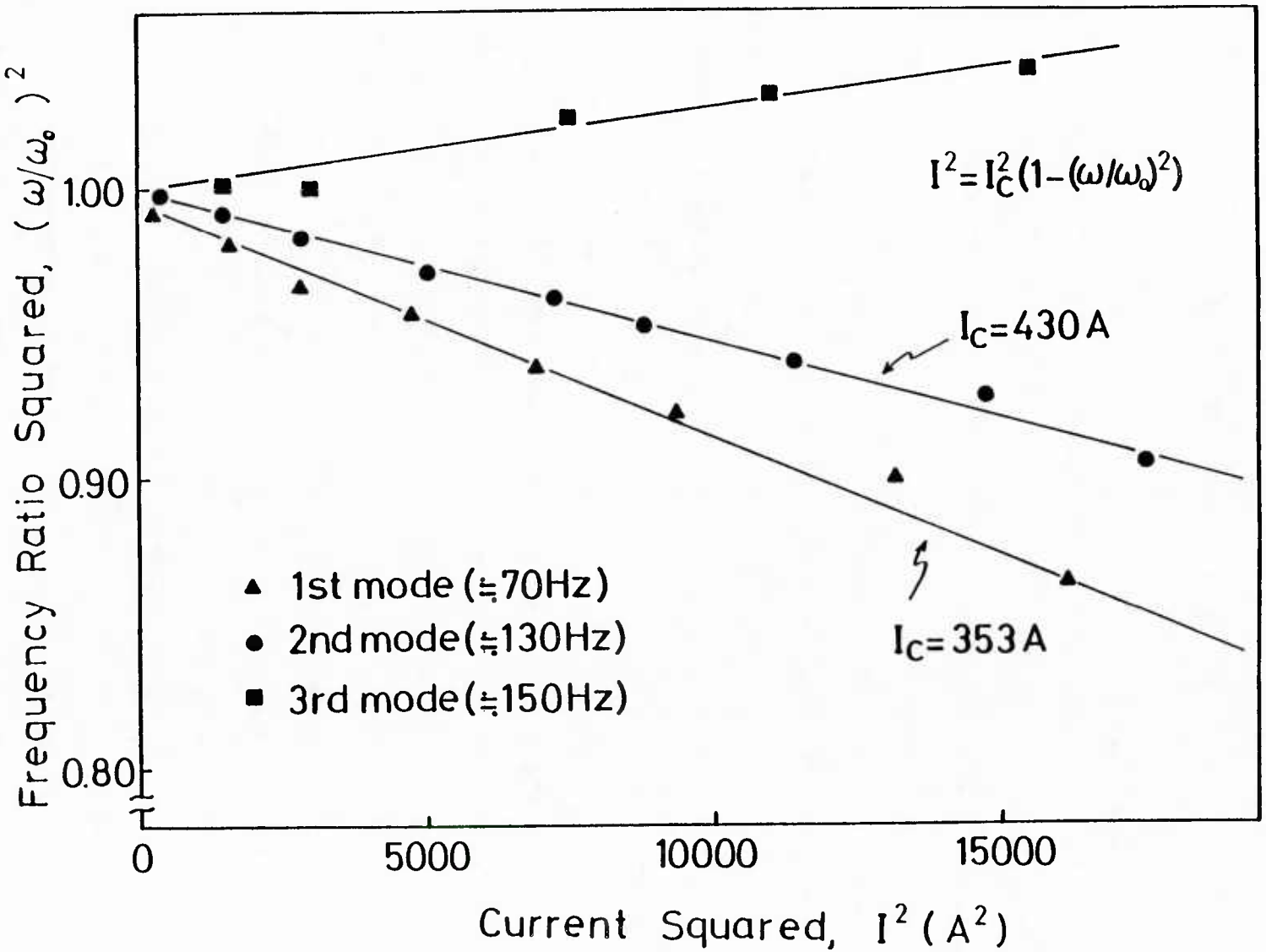

Figure 3.14 Experimental current - frequency dispersion curves for two-ring model with interturn springs

other modes, the magnetic stiffness was stiffened with increase in the magnetic field in this case. Also in this mode, the two rings' deflection were in the opposite direction radially.

Three-Ring Model

The static test showed the increase in the deflection of all three rings as the current increased (Figure 3.15). In this model the deflections are larger for the inner ring than the others. The outer ring did not deform further for current more than 80 A. The deflection of the middle ring was similar to one obtained in the two ring model, while the deflection of the inner ring was much larger compared to the preceding model. The deflection vs. force curve for the middle ring is a typical buckling curve with the misalignments or imperfection.

The Southwell plot for the middle ring is shown in Figure 3.16. The data from two experiments were plotted here. The slopes of both results coincide and give the critical buckling current 195 A. However, the Southwell plots from the inner ring data (Figure 3.17 gave different results. In this figure, too, two sets of data were plotted. The first set showed the critical buckling current of 134 A, while 223 A was obtained from the second set. The slopes of these plots, though, are not as clear as that of the middle ring.

Figure 3.18 shows the frequency-current dispersion curves for the three ring model. The natural frequencies measured 50, 66, 87 and 110 Hz, and all showed the decrease in frequency with increase in the current. The natural frequencies were measured at room temperature

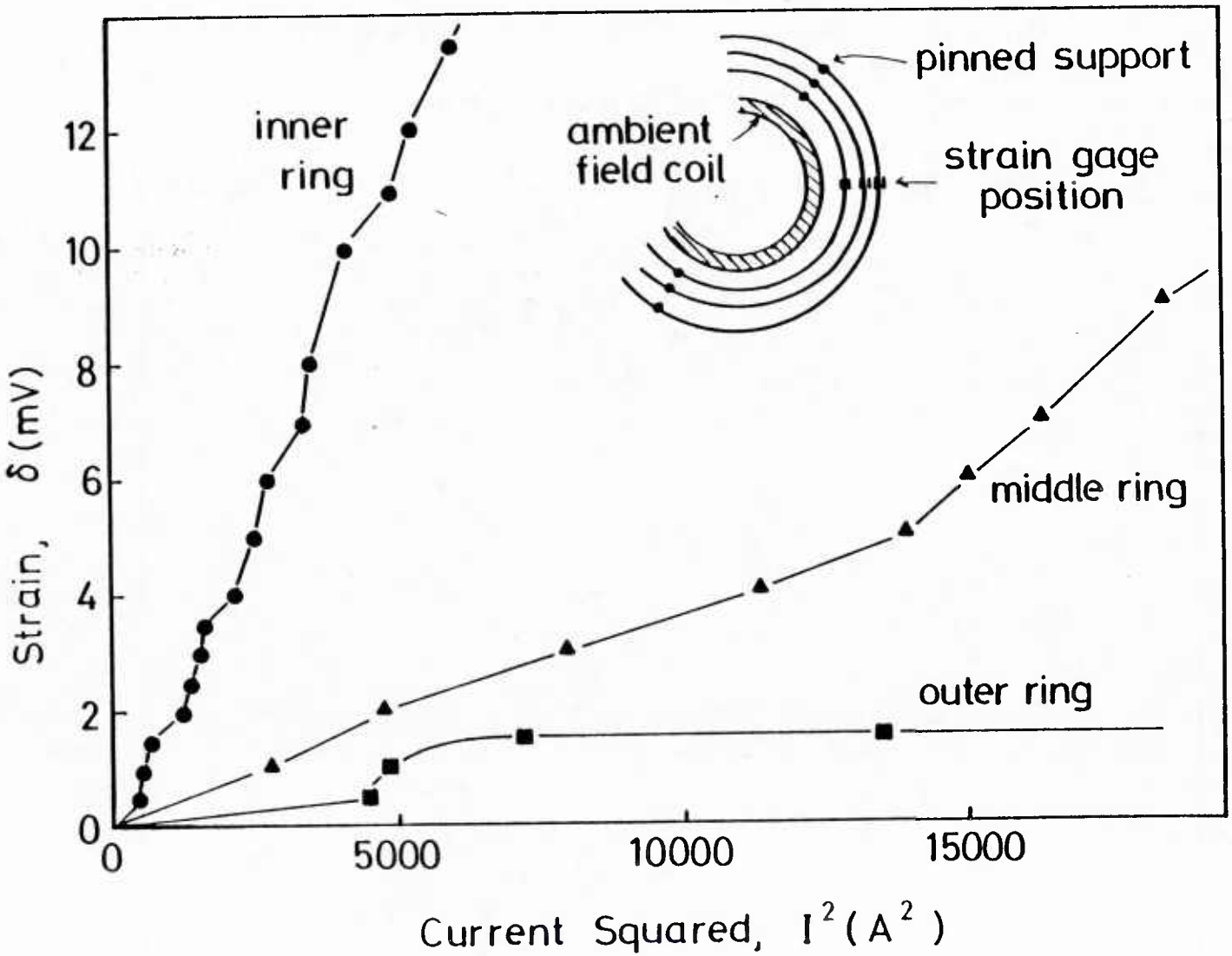

Figure 3.15 Experimental strain vs. current squared curves for three-ring model with interturn springs

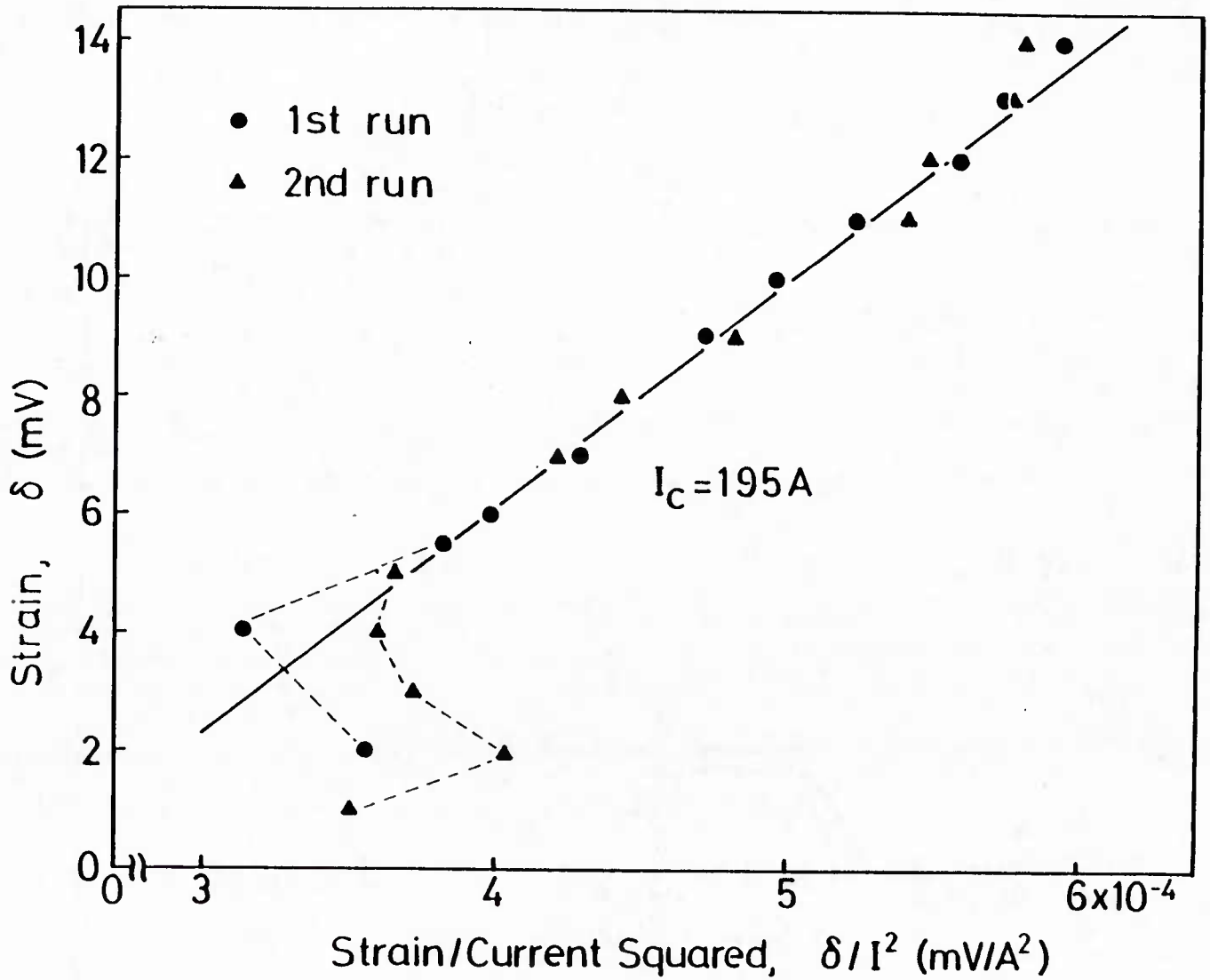

Figure 3.16 Southwell plot of middle ring for three-ring model with interturn springs

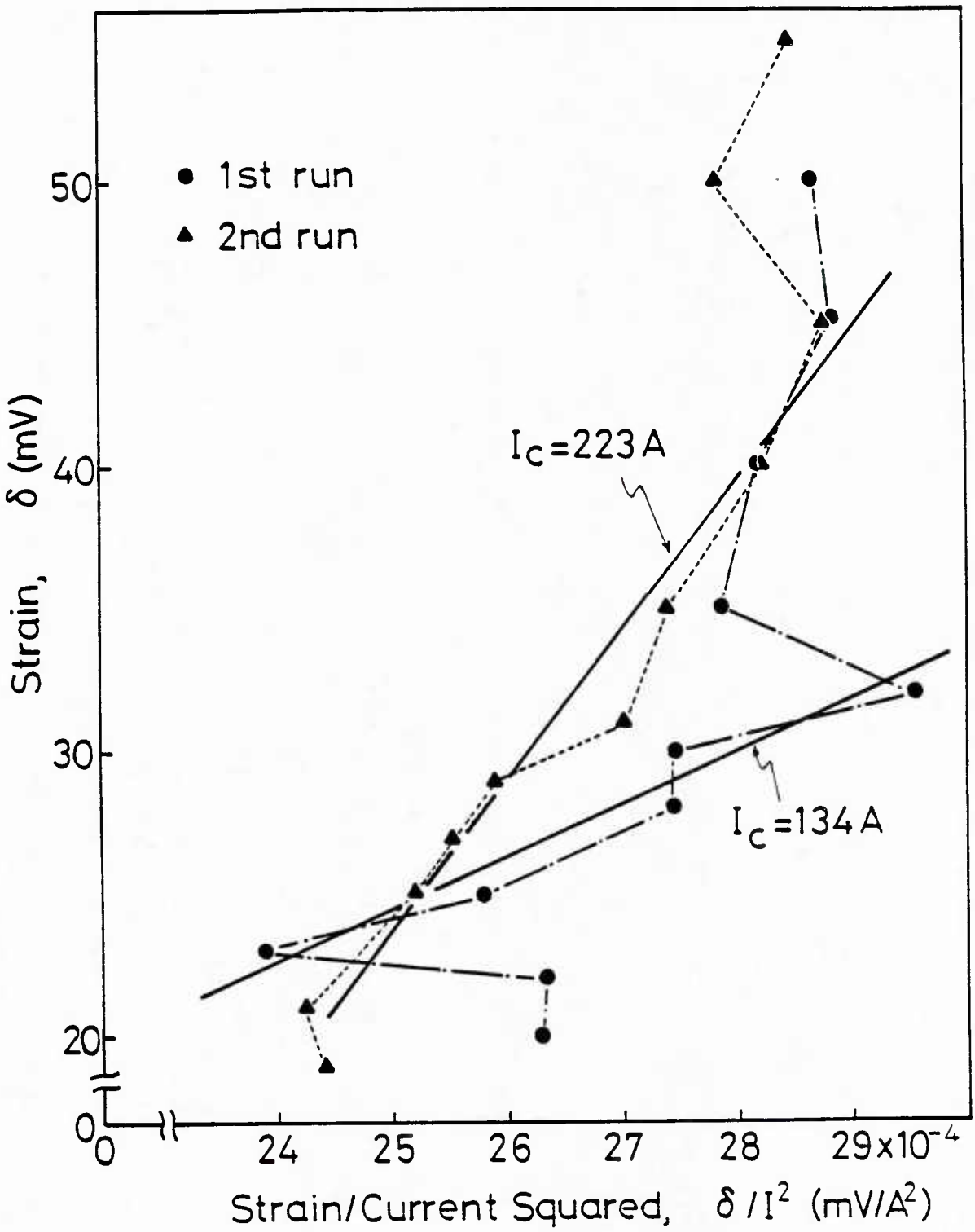

Figure 3.17 Southwell plots of inner ring for three-ring model with interturn springs

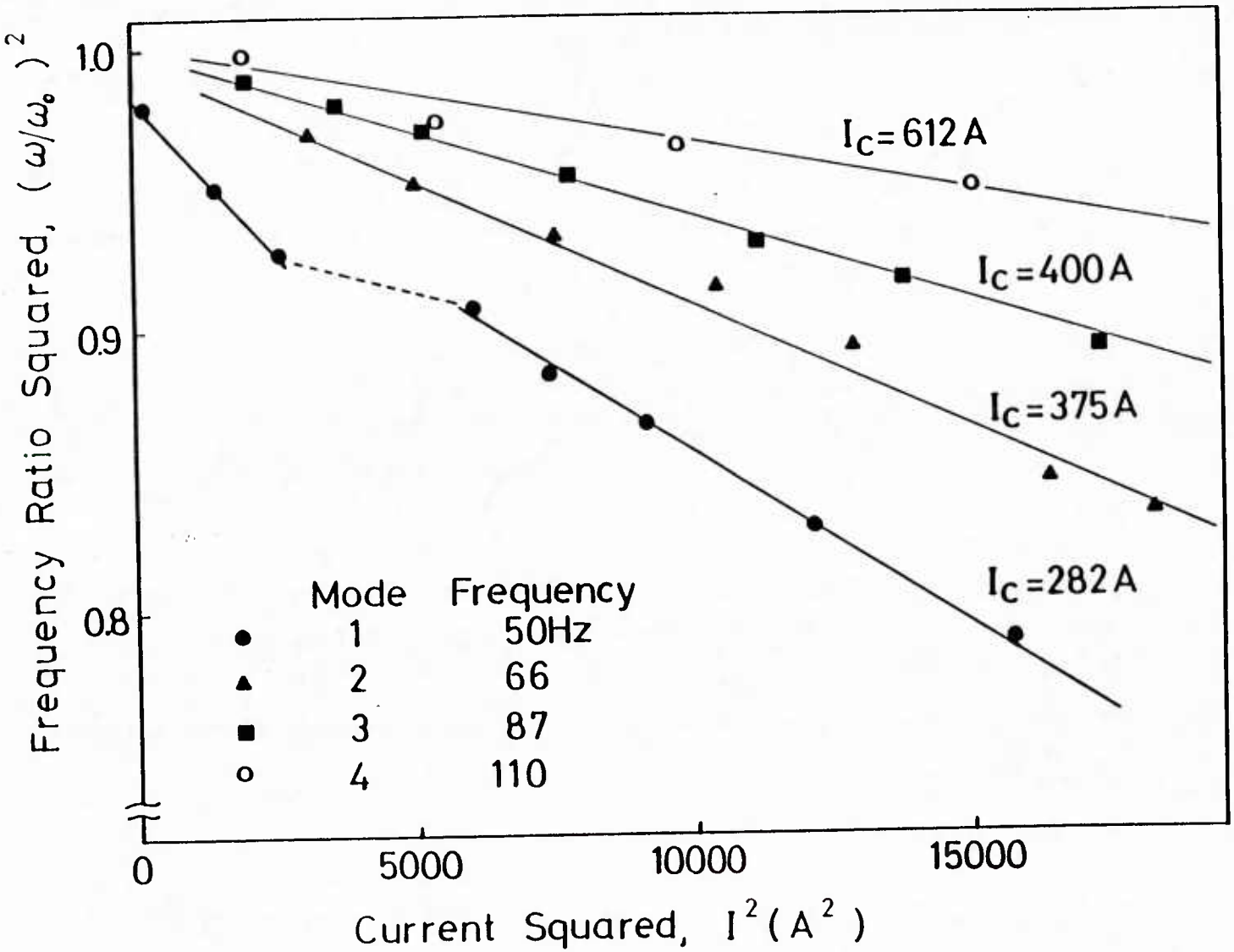

Figure 3.18 Experimental current-frequency dispersion curves for three-ring model with interturn springs

in the air. They were 93, 105, 122 and 155 Hz of which 105 had the highest resonance.

3.2 Buckling of Pancake Winding by a High Current Pulse Discharge

3.2.1 Description of Experiment

In solenoid magnets, the current flows at right angles to the magnetic field, and the Lorentz force interaction between the current and the field results in stresses within the coil. The force at the inner winding is the largest and the direction of force is outward. This force is the major concern of the magnet designers because the force might burst the coil radially outward. On the other hand, the magnetic force on the outer winding has the inward direction, though the force is smaller than that on the inner turn.

To observe the effect of the inward force on the outer winding, a pancake coil was wound and a high pulse current was conducted through the coil. A copper wire of diameter 1.4 mm was used as a conductor. The wire was wound helically around a bakelite core of diameter 10 cm and thickness 1.5 mm without pretension, or loosely. The pancake coil was sandwiched by polycarbonate plates to prevent any lateral movement. In the first experiment, plexiglass plates were used instead. However, they fractured due to the large lateral force and because of the brittleness of the material.

Both ends of the pancake coil were connected to a high power capacitor bank (Figure 3.19). After the capacitors were charged to 3 kV, the current was discharged through the coil. The current was measured by a Rogowski coil.

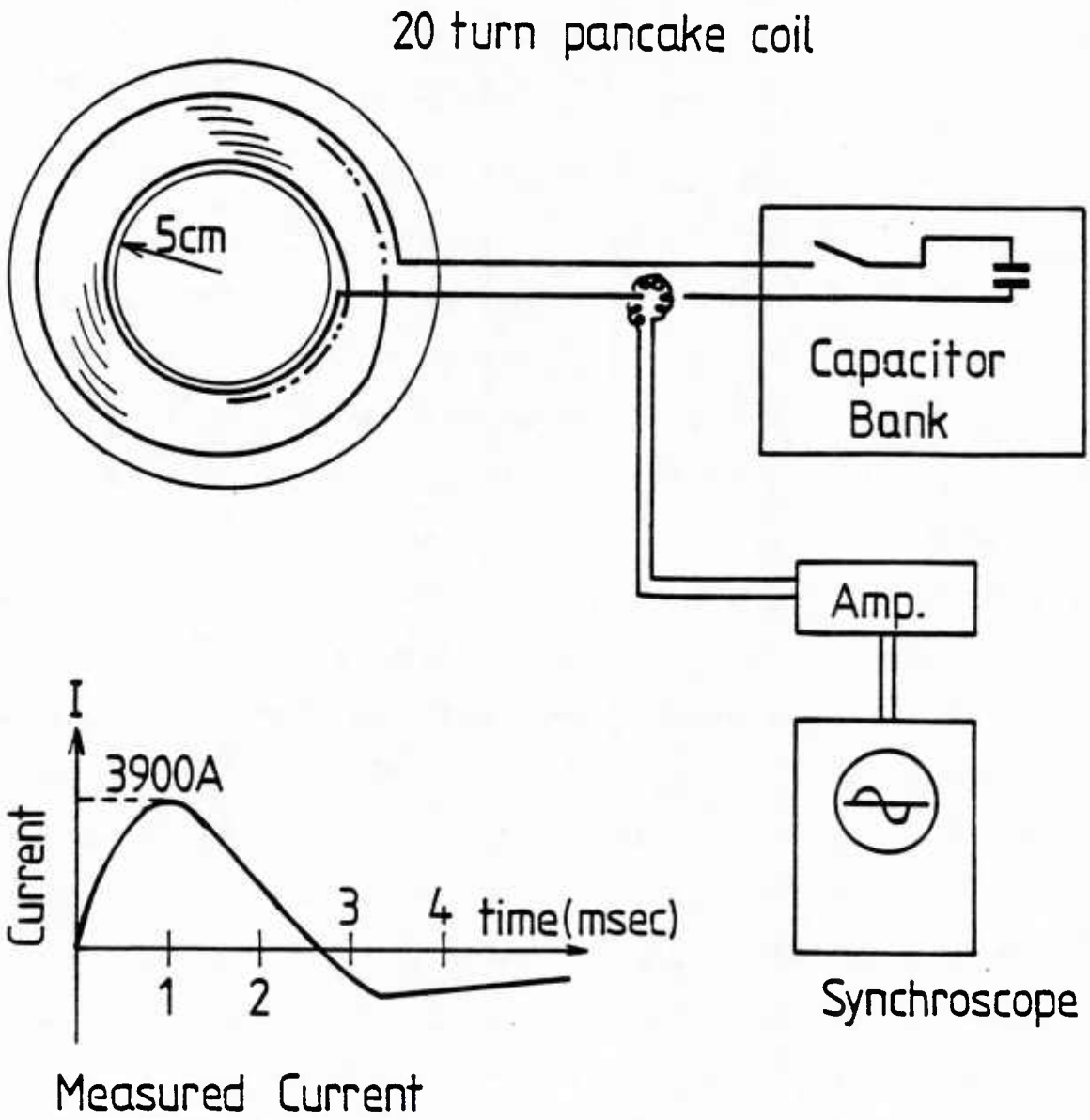

Figure 3.19 Set up for buckling of pancake winding experiment and measured current

3.2.2 Experimental Result

The measured current is shown in Figure 3.19. The current reached its peak at 3900 A in 1 msec, decreased and reversed the direction. The kink at t = 3.3 msec is due to the polarity of the capacitors. The current is equivalent to one with the frequency of 1 kHz and the magnitude of 3900 A.

The deformed pancake coil is shown in Figures 3.20 and 3.21. Figure 3.21 is a close up of the upper section of the coil. Originally the inner turn was at the edge of the bakelite core. It moved plastically about 7 mm outward due to the radial magnetic force, or 14% of plastic elongation was observed.

The deformation in the outer layers is of particular interest. The typical deformations of buckled rings were observed not only in the very outer layers where the magnetic force is inward but also in the middle layers where the magnetic force is outward. The circumferential buckling mode was observed to be 12, which means there were 12 sinusoidal waves along the circumferential direction. The deformation mode depends on the magnitude and frequency of the applied current and also the mechanical constraints of the system. Since the maximum radius of the outer layer remained the same, the overlaps of the layers were observed even though a mechanical restriction was imposed laterally.

The polycarbonate plates were screwed together with 12 screws to prevent lateral deformation of the coil. Six of them were placed outside of the pancake as seen in Figure 3.20. Near these constraints the radius of the outer layer stayed the same, while the layer moved inward between these points.

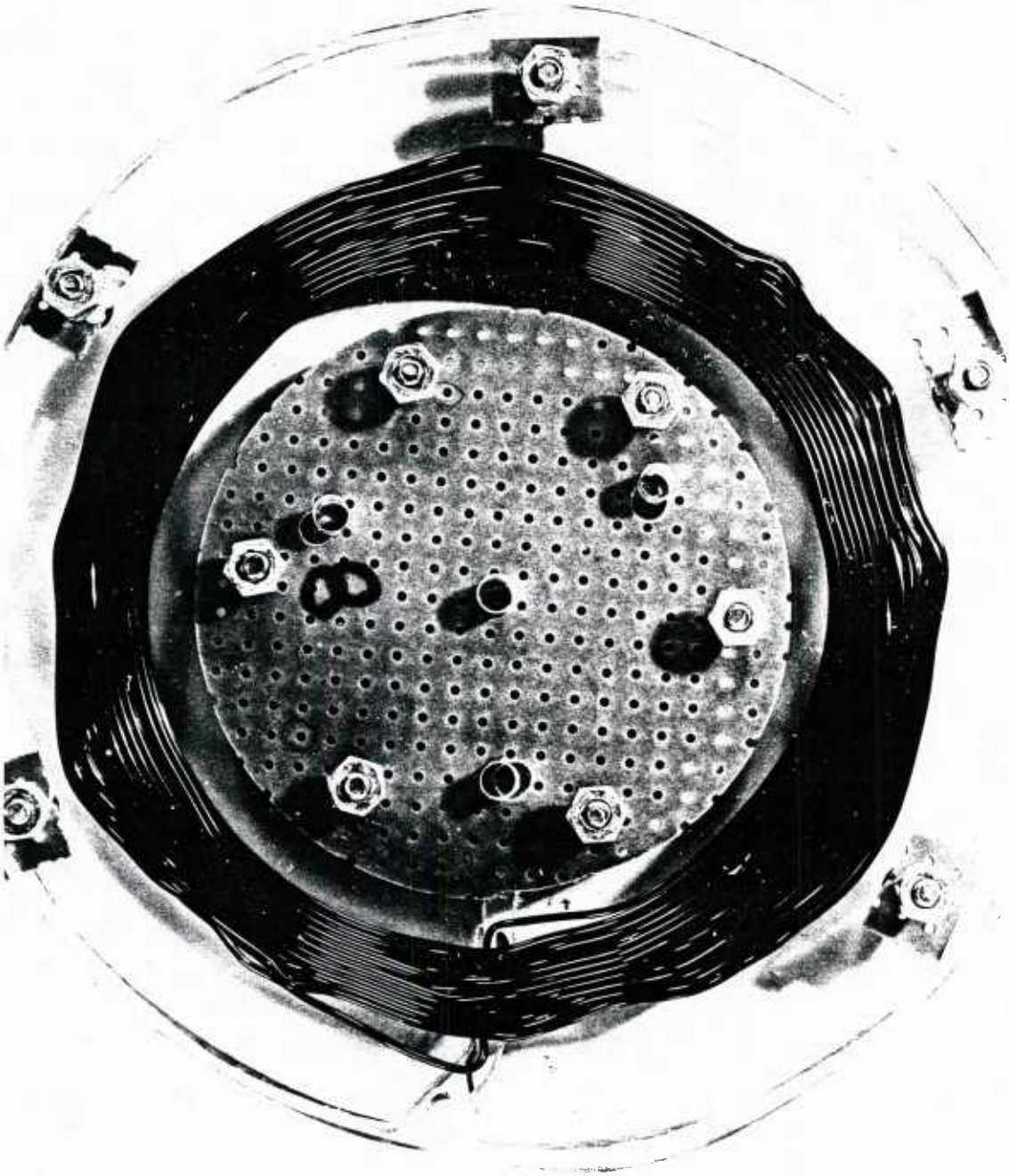

Figure 3.20 Pancake winding buckled by pulsed high current (r = 5cm)

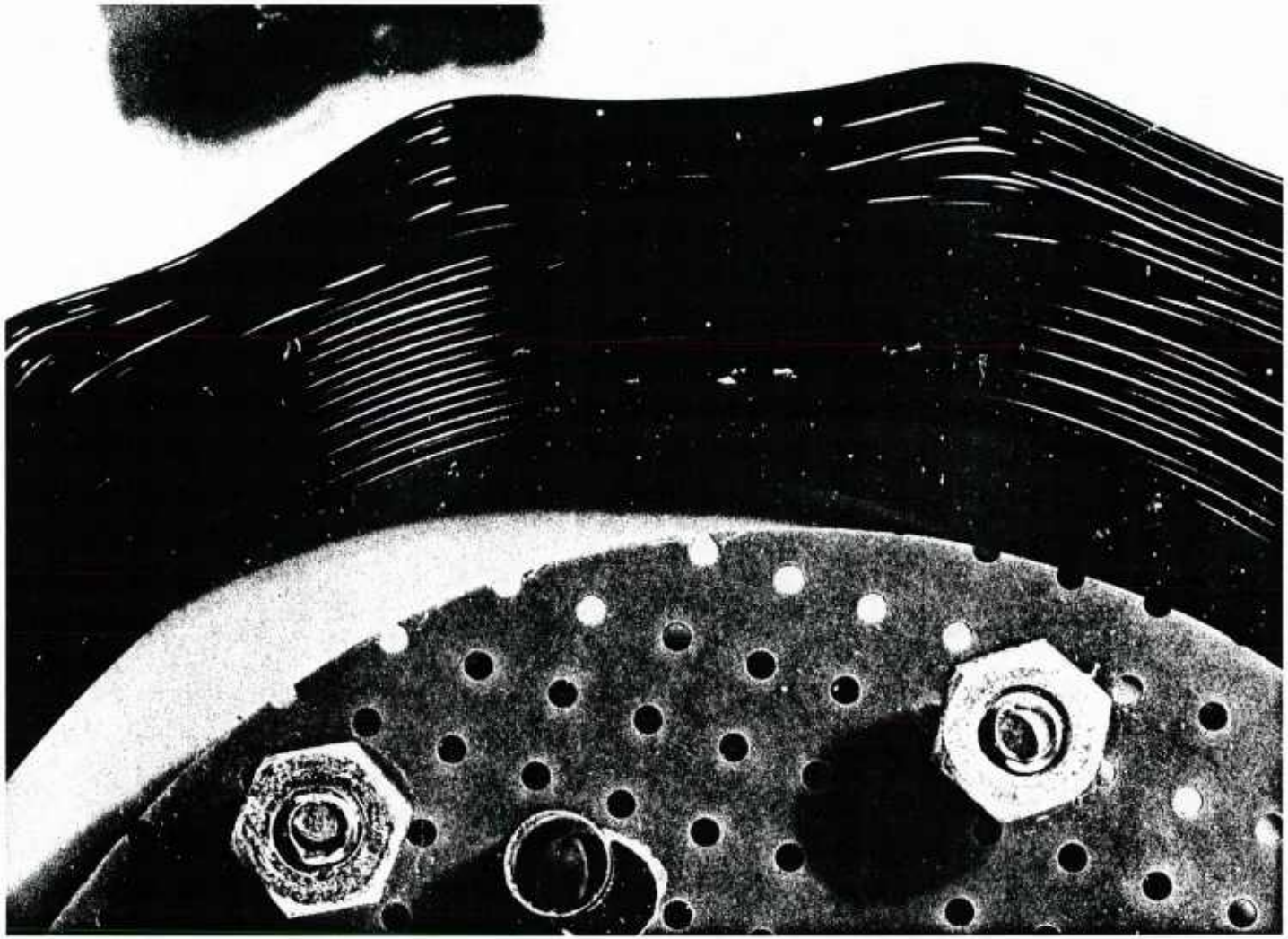

Figure 3.21 Close up of buckled pancake winding showing expansion inside and deformation outside due to compression (ℓ/λ = 15)

It is observed in Figure 3.21 that the seven outer layers buckled, while the other layers deformed uniformly outward. There are overlaps in those layers. This is because the inner layer gets more force, which results in more deformation. The ratio between perimeter and wavelength (ℓ/λ) in this particular retion is 15.

CHAPTER 4

THEORETICAL ANALYSIS AND COMPARISON WITH EXPERIMENTAL RESULTS

4.1 Magnetic Field in the Concentric Ring Model

The magnetic field for a finite length solenoid can be calculated by numerical methods. The extensive studies on this subject were made by Brown et al. (1962). Their result shows that for a constant current density the axial magnetic field drops to zero almost linearly through the thickness and a small reversed field near the outer radius is observed.

In this section the magnetic field produced by multiple concentric rings will be discussed. The concentric ring model preserves the characteristic of the magnetic field in the superconducting magnets. However, this model neglects the out-of-plane force caused by the actual helical winding of magnets. This is because the helical winding produces an out-of-plane force due to the radial component of current and the magnetic field gradient in the circumferential direction, and it becomes a coupled problem on in-plane and out-of-plane motion.

The magnetic field produced by a current carrying ring on the same plane as the ring is expressed by eqn. (2.1.57) and is shown in Figure 4.1. The direction of the field changes outside the ring. When there is more than one ring, the magnetic field is given by superposing the field produced by each ring. For example, the magnetic field of 10 rings, whose radii range from 11 cm to 20 cm, is shown in Figure 4.2.

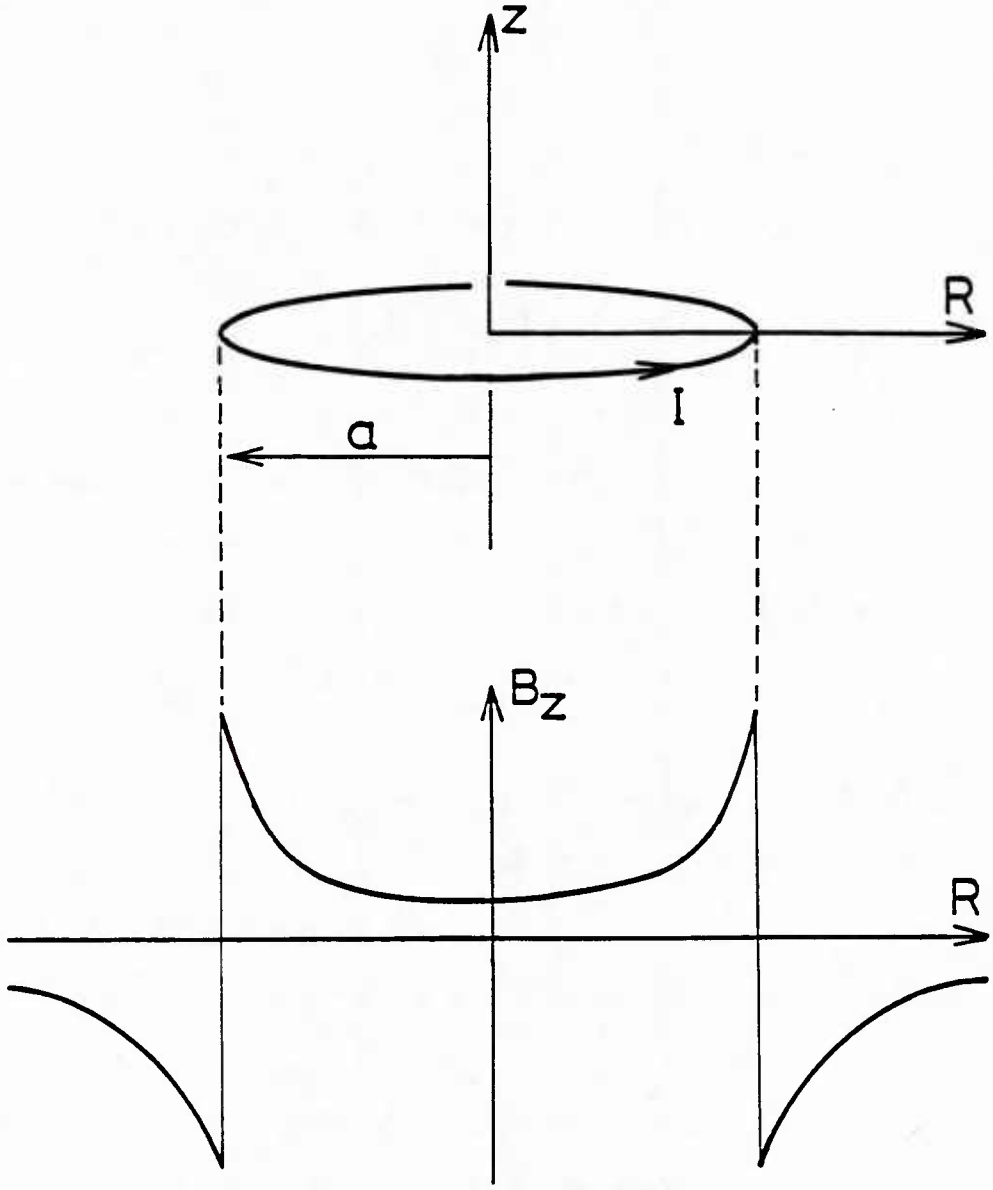

$$B_z = \frac{\mu I}{2\pi a}\left(\frac{K}{a+R} + \frac{E}{a-R}\right)$$

Figure 4.1 Circular current loop and z component of its magnetic field

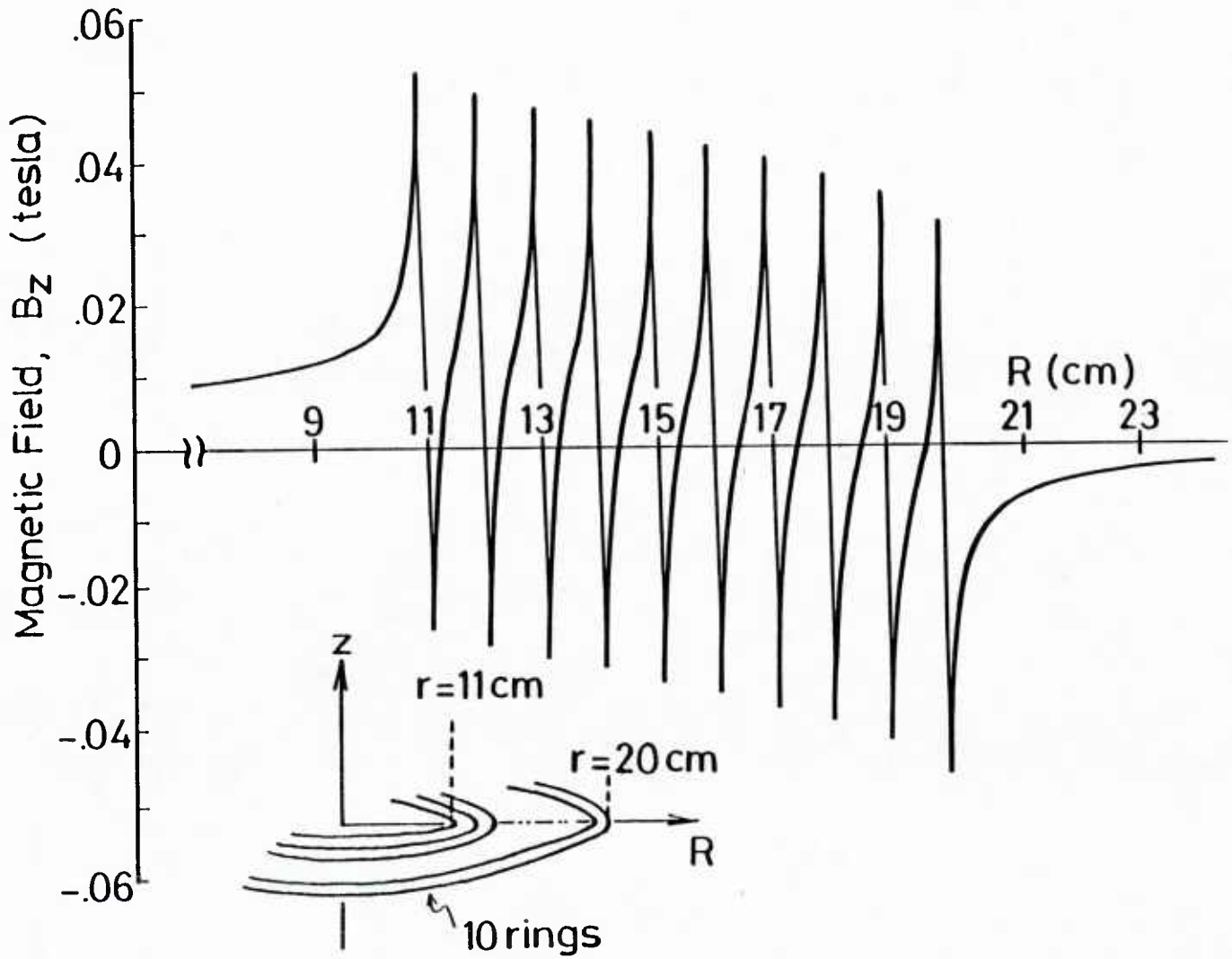

Figure 4.2 Z component of magnetic field produced by 10 concentric copolanar rings (r = 11 - 20 cm)

In this case, the conducted current is assumed to be 200 A. The results of the buckling and vibration analysis of this model will be given later in section 4.3.3.

At the position where the ring exists the magnetic field shows the singularity. However, since any ring has finite width, it is feasible to assume that the magnetic field changes linearly through the width.

When the magnetic force on a ring is considered, the applicable magnetic field may be divided into two parts; the field produced by itself and the field produced by the rest of the rings. The field produced by the rest of the rings is

$$B_{other} = \frac{\mu I}{4\pi} \sum_{\substack{j=1 \\ j \neq i}}^{N} \left[\frac{K}{r_j + r_i} + \frac{E}{r_j - r_i} \right] \tag{4.1.1}$$

where K and E are the complete elliptic integrals and N is the total number of the rings. The self field is substantially smaller than the field produced by the rest of the rings (see Section 4.2.1 for discussion). Therefore, the applicable magnetic field for the magnetic force calculation is defined as the field produced by the rest of the rings.

For example, if the force on the 14 cm ring is of interest, the magnetic field due to the rest of the rings gives the profile of the field acting on the ring (Figure 4.3). In this case the field is 0.0081 tesla. Similarly the force on the outer or 20 cm ring is given by the magnetic field produced by the inner 9 rings (Figure 4.4). The field is -0.0073 tesla, which places this ring under compression.

The magnetic field on each ring in the 10 ring case is plotted in Figure 4.5. The transverse field does not change linearly, particularly

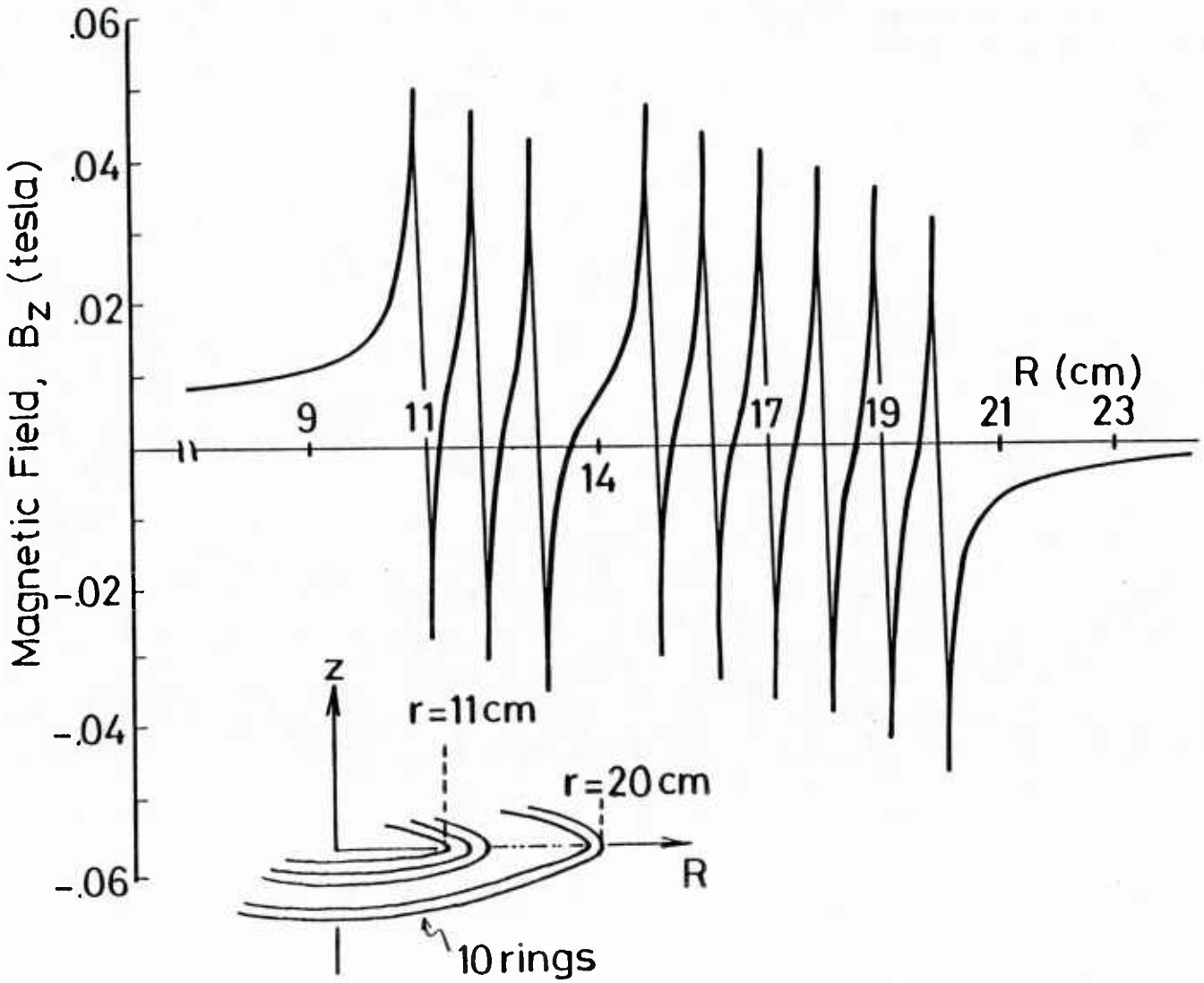

Figure 4.3 Z component of magnetic field acting on 14 cm ring calculated by removing the 14 cm ring

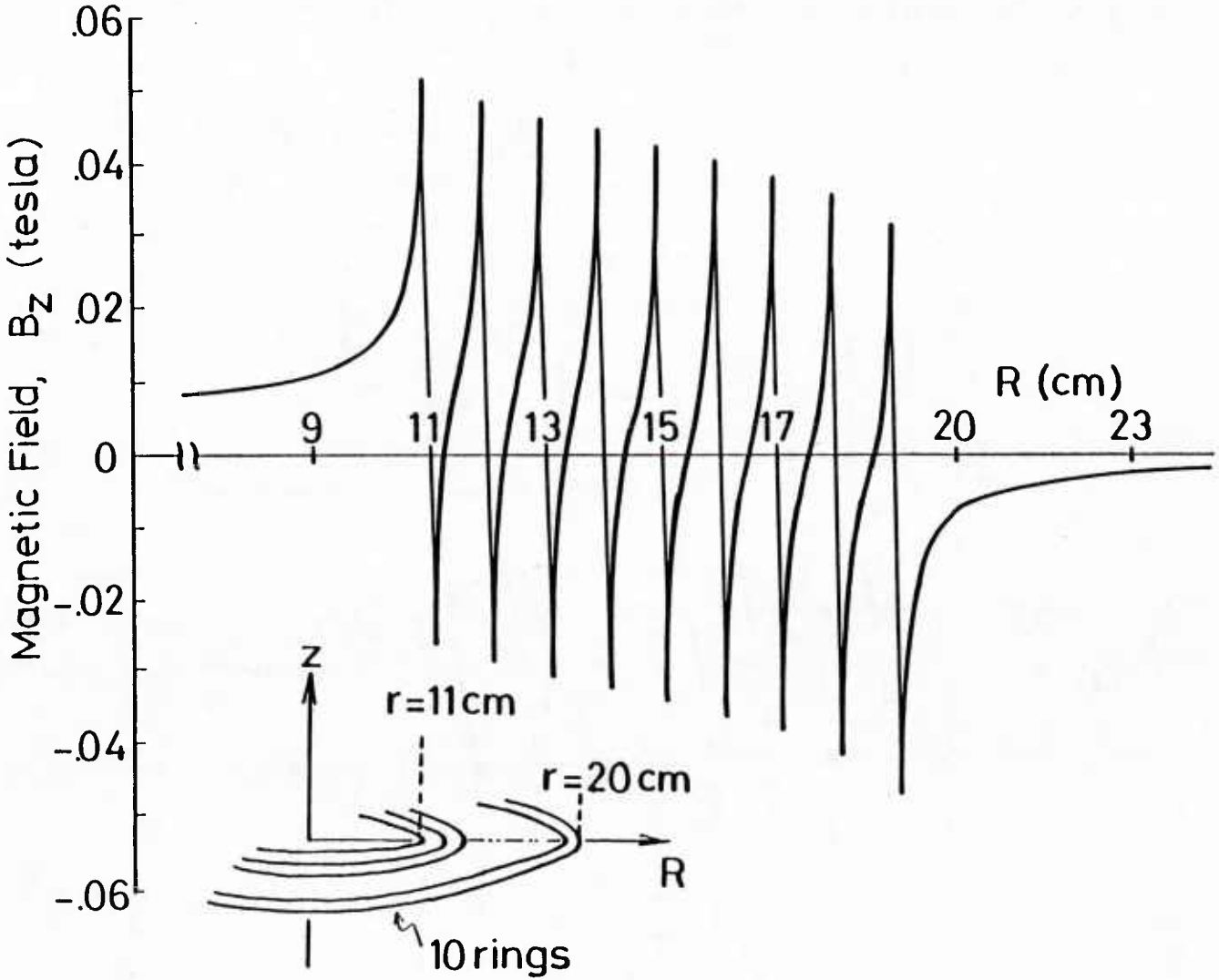

Figure 4.4 Z component of magnetic field acting on 20 cm ring calculated by removing the 20 cm ring

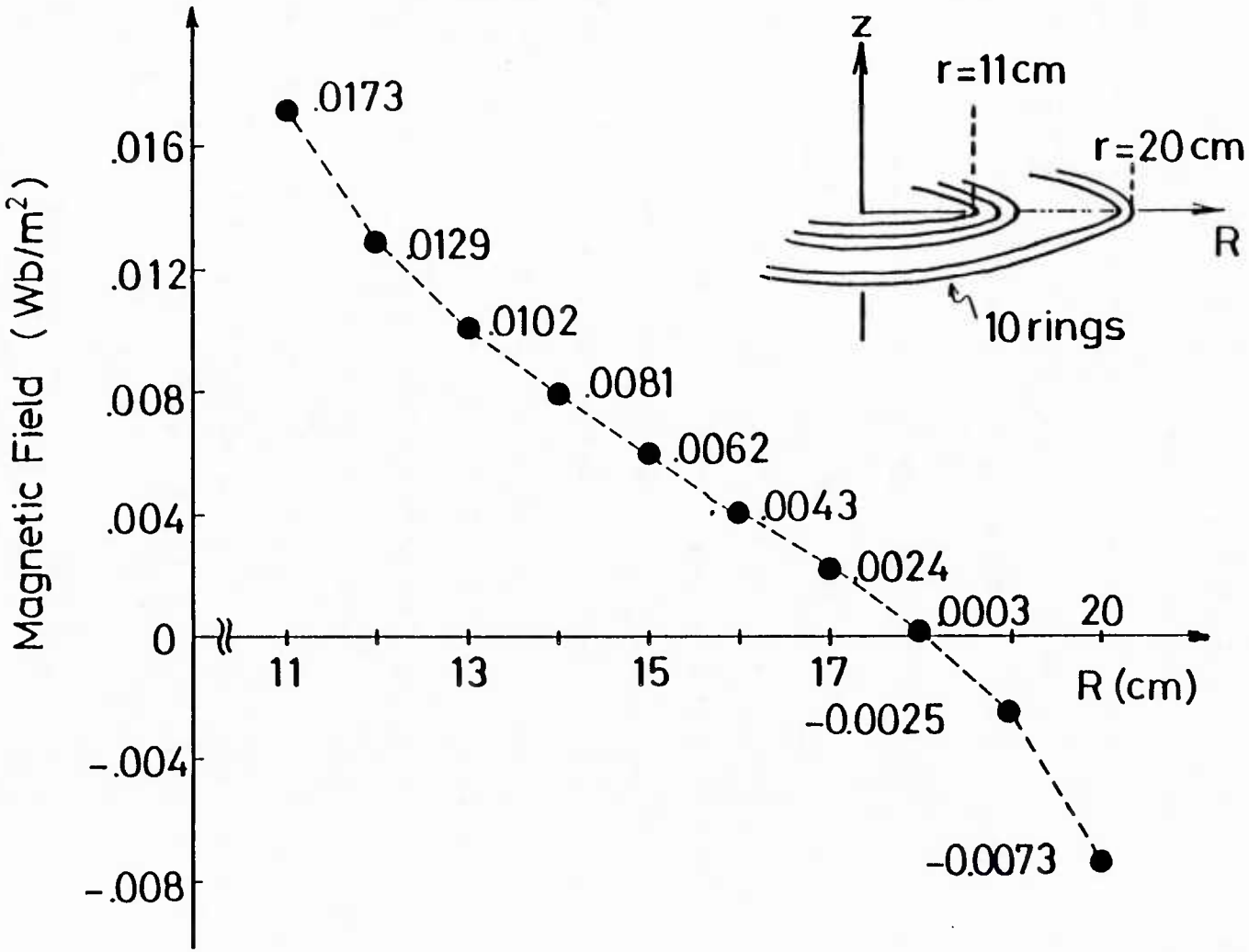

Figure 4.5 Magnetic field acting on each ring produced by other rings

near the outer and inner turns. Also the reversed magnetic field is about 40% of the maximum field and is not necessarily small.

The magnetic stiffness applied to each ring is determined by the magnetic field gradient. In this example, the gradient on the 14 cm ring is larger than that of the 20 cm ring, which implies that the 14 cm ring is more susceptible to the magnetic stiffness.

4.2 Single Ring in the Transverse Magnetic Field

4.2.1 Derivation of Equation

In this section the equations are derived for the buckling and vibration of a single circular ring placed in a vertical magnetic field. This problem was analyzed by Daniels (1952) who observed such a failure in a normal conductor solenoid. However, in his analysis he did not include the effect of the initial tension due to the magnetic force on the current.

To examine the elastic stability, the body force is divided into initial and deformation dependent terms and the equilibrium equations are linearized [Moon (1984)]. The initial stress state in the circular flat ring is expressed by the circumferential tension given by

$$T_o = f_o R \tag{4.2.1}$$

where f_o is the Lorentz force (eqn. 2.3.11) in the unbent configuration. For a coil with circular cross section with radius a, T_o is given by

$$T_o = \frac{\mu_o I_o^2}{4\pi}\left[\ln\frac{8R}{a} - \frac{3}{4}\right] + I_o B_y R \tag{4.2.2}$$

The current I_o is positive when its direction is in the positive z axis. If the ring is in a large enough magnetic field, then the value of the first term is considerably smaller than that of the second term. Therefore, T_o may be expressed as

$$T_o = I_o B_y R \quad . \tag{4.2.3}$$

There is an associated radial displacement due to the tension or compression. However, the radial displacement u is assumed to be due to in-plane bending only, in this analysis.

Then the linearized equilibrium equations in the in-plane deformation (section 2.3.4) take the following form [Love (1922)]

$$\frac{\partial N_x}{\partial z} + T_o(\kappa_1 - \frac{1}{R}) + \frac{T_1}{R} + f_x = m \frac{\partial^2 u}{\partial t^2} \tag{4.2.4}$$

$$\frac{\partial T_1}{\partial z} - \frac{N_x}{R} + f_z = m \frac{\partial^2 w}{\partial t^2} \tag{4.2.5}$$

$$\frac{\partial G_y}{\partial z} + N_x = 0 \quad . \tag{4.2.6}$$

In these equations T_1 is the added tension due to the bending, and f is the distributed force, which will be discussed later. The other governing equations are

$$G_y = EI_y(\kappa_1 - \frac{1}{R}) = D(\kappa_1 - \frac{1}{R}) \tag{4.2.7}$$

$$\kappa_1 = \frac{1}{R} + \frac{u}{R^2} + \frac{\partial^2 u}{\partial z^2} \tag{4.2.8}$$

$$\frac{\partial w}{\partial z} = \frac{u}{R} \quad . \tag{4.2.9}$$

Substitution of equation (4.2.8) into equation (4.2.4) yields

$$\frac{\partial N_x}{\partial z} + T_o\left(\frac{u}{R^2} + u''_x\right) + \frac{T_o}{R} + f_x = m\,\frac{\partial^2 u}{\partial t^2} \quad . \tag{4.2.10}$$

After differentiating by z and substituting into equation (4.2.5),

$$N''_x + T_o\left(\frac{u}{R^2} + u''\right)' + \frac{1}{R}\left(\frac{N_x}{R} + m\,\frac{\partial^2 w}{\partial t^2}\right) + f'_x - \frac{f_z}{R} = m\,\frac{\partial^2 u'_x}{\partial t^2} \tag{4.2.11}$$

where the primes are differentiations by z. The final equation of the motion is given by substituting equations (4.2.6) and (4.2.7) into equation (4.2.11)

$$-D\left(\frac{u}{R^2} + u''\right)''' + T_o\left(\frac{u}{R^2} + u''\right)' - \frac{D}{R^2}\left(\frac{u}{R^2} + u''\right)' + f'_x - \frac{f_z}{R}$$
$$= m\,\frac{\partial^2}{\partial t^2}\left(u' - \frac{w}{R}\right) \quad . \tag{4.2.12}$$

Now one assumes that all variables vary as $e^{j\omega t}$, where $j = \sqrt{-1}$. Then equation (4.2.12) yields

$$-D\left(\frac{u}{R^2} + u''\right)''' + T_o\left(\frac{u}{R^2} + u''\right)' - \frac{D}{R^2}\left(\frac{u}{R} + u''\right)' + f'_x - \frac{f_z}{R}$$
$$= -m\omega^2\left(u' - \frac{w}{R}\right) \quad . \tag{4.2.13}$$

The force term $(f_x' - f_z/R)$ may be divided into two components; the perturbed magnetic force components and the mechanical stiffness. The discussion on each component will be given in the following paragraphs.

<u>The perturbed magnetic force:</u> The perturbed magnetic force is a consequence of three effects. Two of them are due to the ring movement in the uniform magnetic field [Moon (1984(]. First if $u' \neq 0$, the direction of $\underset{\sim}{I} \times \underset{\sim}{B}$ is no longer radial. The inward, radial component of $\underset{\sim}{I}$ produces a circumferential force component $f_z = IB_o u'$. The second perturbed force results from the fact that when $u \neq 0$ the actual length of the differential element becomes $R(1 - u/R)d\theta$ instead of $Rd\theta$ in terms of first order in u. Thus the difference between the actual and initial radial force is $f_x = IB_o u/R$. This term is required in order for the buckling behavior to be independent of rigid body translation in the plane of the ring. With these assumptions one has

$$\underset{\sim}{f}_{min,mag} = \frac{IB_o u}{R} \underset{\sim}{e}_x + I_o B_o u' \underset{\sim}{e}_z \tag{4.2.14}$$

and

$$\frac{\partial f_x}{\partial z} - \frac{\partial f_z}{R} = 0 \quad . \tag{4.2.15}$$

Thus the perturbed magnetic forces due to the ring movement in the uniform magnetic field do not affect the buckling or vibration directly.

The last effect is due to the magnetic field gradient. In linear analysis, if Γ is the first derivative of the magnetic field about the radial deflection, then the force due to the magnetic gradient is given by equation (2.1.47) as

$$f_{mag,grad.} = \Gamma I\ u \qquad . \tag{4.2.16}$$

This is defined as the force due to the magnetic stiffness.

<u>The mechanical stiffness</u>: In this analysis the ring has mechanical constraints by linear springs. These effects can be expressed as

$$f_{mech.x} = -k_x u \tag{4.2.17}$$

$$f_{mech.z} = -k_z w \tag{4.2.18}$$

where k_x and k_z are linear spring constants per unit length in the x (radial) and z (circumferential) directions, respectively.

Now the total distributed force on the ring is expressed by summing equations (4.2.15) to (4.2.18)

$$f_x' - \frac{f_z}{R} = (-k_x u)' + (\Gamma\ I\ u)' - \left(-\frac{k_z w}{R}\right)$$

$$= (-k_x + \Gamma I)u' + \frac{k_z w}{R} \qquad . \tag{4.2.19}$$

Then the governing equation of the ring is

$$-D\left(\frac{u}{R^2} + u''\right)''' + T_o\left(\frac{u}{R^2} + u''\right)' - \frac{D}{R^2}\left(\frac{u}{R^2} + u''\right)' + (-k_x + \Gamma I)u'$$

$$+ \frac{k_z w}{R} = -m\omega^2\left(u' - \frac{w}{R}\right) \qquad . \tag{4.2.20}$$

By applying the equation of inextensibility (4.2.9), the governing equation becomes a function of w only as to the deformation. Now we impose the circumferential deformation mode

$$w = w_o e^{jn\theta} \quad \text{or} \quad u = jnw \tag{4.2.21}$$

where $z = R\theta$ and $j = \sqrt{-1}$.

into the governing equation. Here w_o is the magnitude of the deformation in the z direction. The deformation mode is expressed by n which is integer (n = 0, 1, 2, 3, ...). n = 0 and 1 implies the rotational and translational rigid body motions of the ring, respectively (Figure 4.6). For n larger than 1, the ring exhibits bending deformation. When n = 2 the ring performs the fundamental mode of bending deformation. In this mode the circular ring changes into an ellipse at the extreme position. When n = 3 the ring changes into a rounded triangle. In general, the deformed ring shows the n waves on its circumference in the n-th mode. The extreme positions of the ring during the deformation are shown in Figure 4.6 by dotted lines.

Substituting equation (4.2.21) into equation (4.2.20) yields the characteristic equation

$$-D\left(\frac{n^4}{R^5} + \frac{n^6}{R^5}\right) + T_o\left(-\frac{n^2}{R^3} + \frac{n^4}{R^3}\right) - \frac{D}{R^2}\left(-\frac{n^2}{R^3} + \frac{n^4}{R^3}\right) + (-k_x + PI)\frac{-n^2}{R} + \frac{k_z}{R} = -m\omega^2\left(-\frac{n^2}{R} - \frac{1}{R}\right) \tag{4.2.22}$$

or

$$\frac{D}{R^4} n^2(n^2 - 1)^2 - \frac{B_o I}{R} n^2(n^2 - 1) + (n^2 k_x + k_z - \Gamma I n^2) = m\omega^2(n^2 + 1) \tag{4.2.23}$$

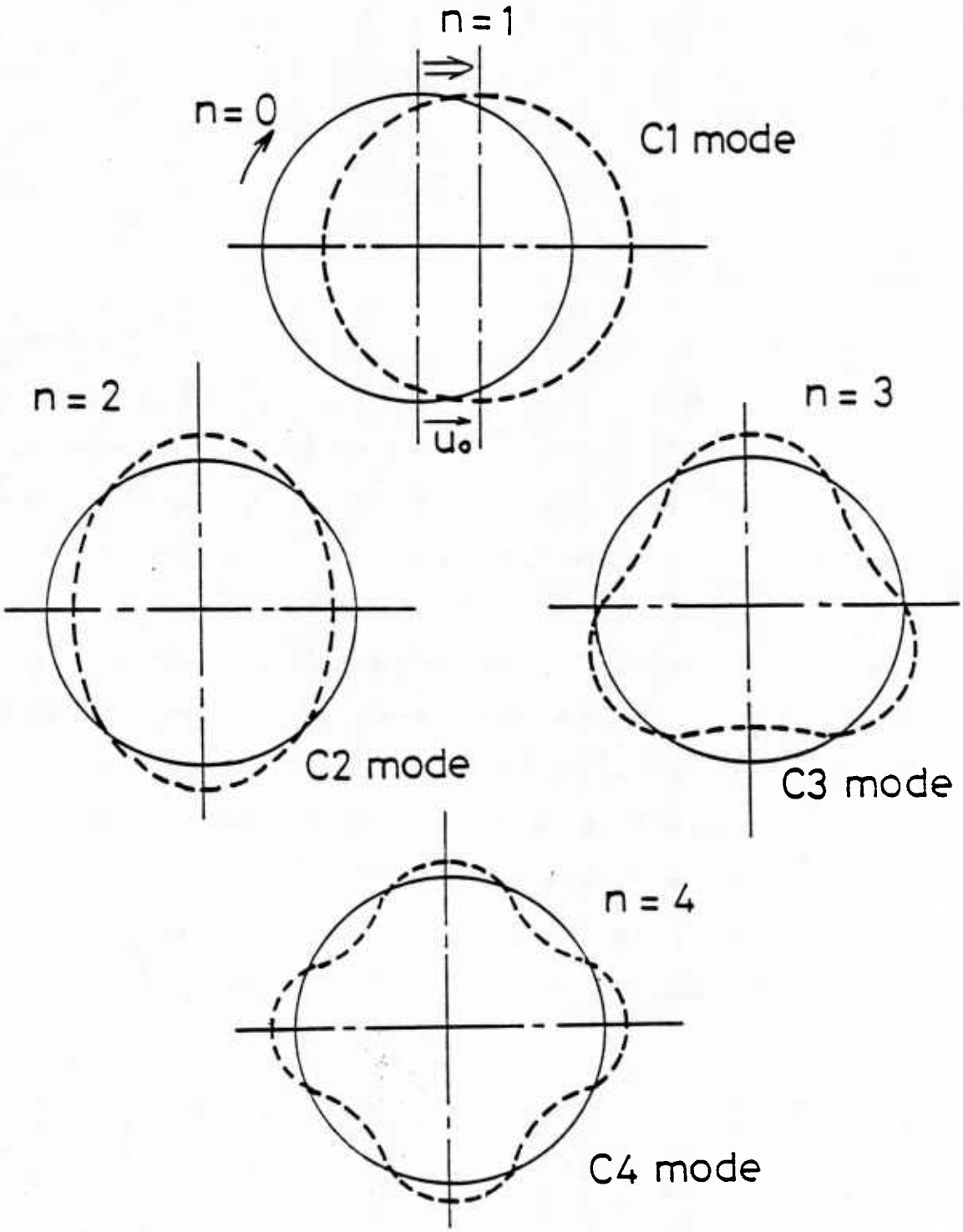

Figure 4.6 Inplane rigid body motion (n = 0 and 1) and bending deformation (n = 2, 3, 4, ...) of circular ring

The critical buckling current for the given magnetic field, spring constants and the magnetic field gradient can be obtained by putting $\omega = 0$. The natural frequency for the given condition is obtained from this equation, too.

4.2.2 Comparison Between Theory and Experiment

When the experiment is simulated, the magnetic field B_o and its gradient Γ in equation (4.2.23) is produced by the ambient field coil. The ring and the ambient field coil were connected directly and had the same current. Therefore, the field and its gradient are calculated using equations (2.1.57) and (2.1.58):

$$B_o = \frac{\mu_o}{2\pi}\left[\frac{K}{a + R} + \frac{E}{a - R}\right] \cdot mI = \alpha I \tag{4.2.24}$$

$$\Gamma = \frac{\mu_o}{2\pi}\,\frac{1}{R(a + R)}\left[\frac{a^2 + R^2}{(a - R)^2}E - K\right] \cdot mI = \gamma I \tag{4.2.25}$$

where R and a are radii of the ring and ambient field coil, respectively, m is the number of turns in the ambient field coil, and K and E are the complete elliptic integrals. For convenience, the magnetic field and the magnetic gradient coefficients α and γ are introduced.

Then the critical buckling current is given as

$$I^2 = \frac{(D/R^4)n^2(n^2 - 1)^2 + n^2k_x + k_z}{(\alpha/R)n^2(n^2 - 1) + \gamma n^2} \tag{4.2.26}$$

The frequency of the ring under the given current I is obtained from the equation (4.2.23), too, and

$$\omega^2 = \frac{1}{m(n^2 + 1)}\left[\frac{D}{R^4}n^2(n^2 - 1)^2 + n^2k_x + k_z - \left(\frac{n^2(n^2 - 1)}{R} + \gamma n\right)I^2\right] . \tag{4.2.27}$$

The square of the frequency is a linear function of the current squared in the one-ring model.

One-Ring Model Without Springs

The critical buckling current and the natural frequencies were calculated from equations (4.2.26) and (4.2.27), using the material constants given in section 3.1.3. The spring constants k_x and k_z were set to zero in the simulation of this model.

The theoretical results are listed in Table 4.1 along with the experimental results. The current-frequency dispersion curves are shown in Figure 4.7. These curves were obtained by calculating the change of the frequency as a function of current in the system. In this figure Cn stands for the circumferential n-th mode of the deflection. For example, in C2 mode the circular ring changes to an ellipse. Since the out-of-plane deformation of the ring was prevented by pin supports in the experiment, the comparison is given only for the in-plane motion. The comparison shows that the experimental buckling current of about 160 A and the frequency 80 Hz are of the third mode instead of the lowest second mode. This was due to the misalignments and imperfections of the system in the static test. In the dynamic test the natural frequency 34 Hz for the second mode was not excited because the amplifier used for the driving coil has poor gain in the range below 50 Hz.

One-Ring Model With Springs

The effects of the initial tension and the magnetic stiffness will be discussed in the analysis of this model. Table 4.2 shows the critical buckling current of the ring obtained from the experiment and theory

Table 4.1 Experimental and theoretical values of buckling constants and natural frequencies for one-ring model without springs

Circumferential Mode	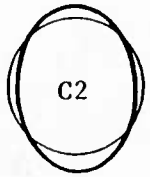 C2		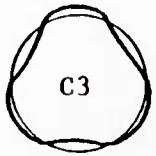 C3		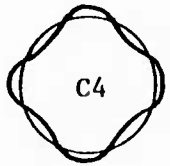 C4	
	Buckling Current	Natural Frequency	Buckling Current	Natural Frequency	Buckling Current	Natural Frequency
Experiment						
vibration test in the air	-----	34 Hz	-----	69 Hz	-----	103 Hz
static test	-----	-----	167 A	-----	-----	-----
dynamic test	-----	-----	156 A	80 Hz	-----	-----
Theory						
static analysis	62 A	-----	145 A	-----	236 A	-----
dynamic analysis	-----	32 Hz	-----	92 Hz	-----	177 Hz

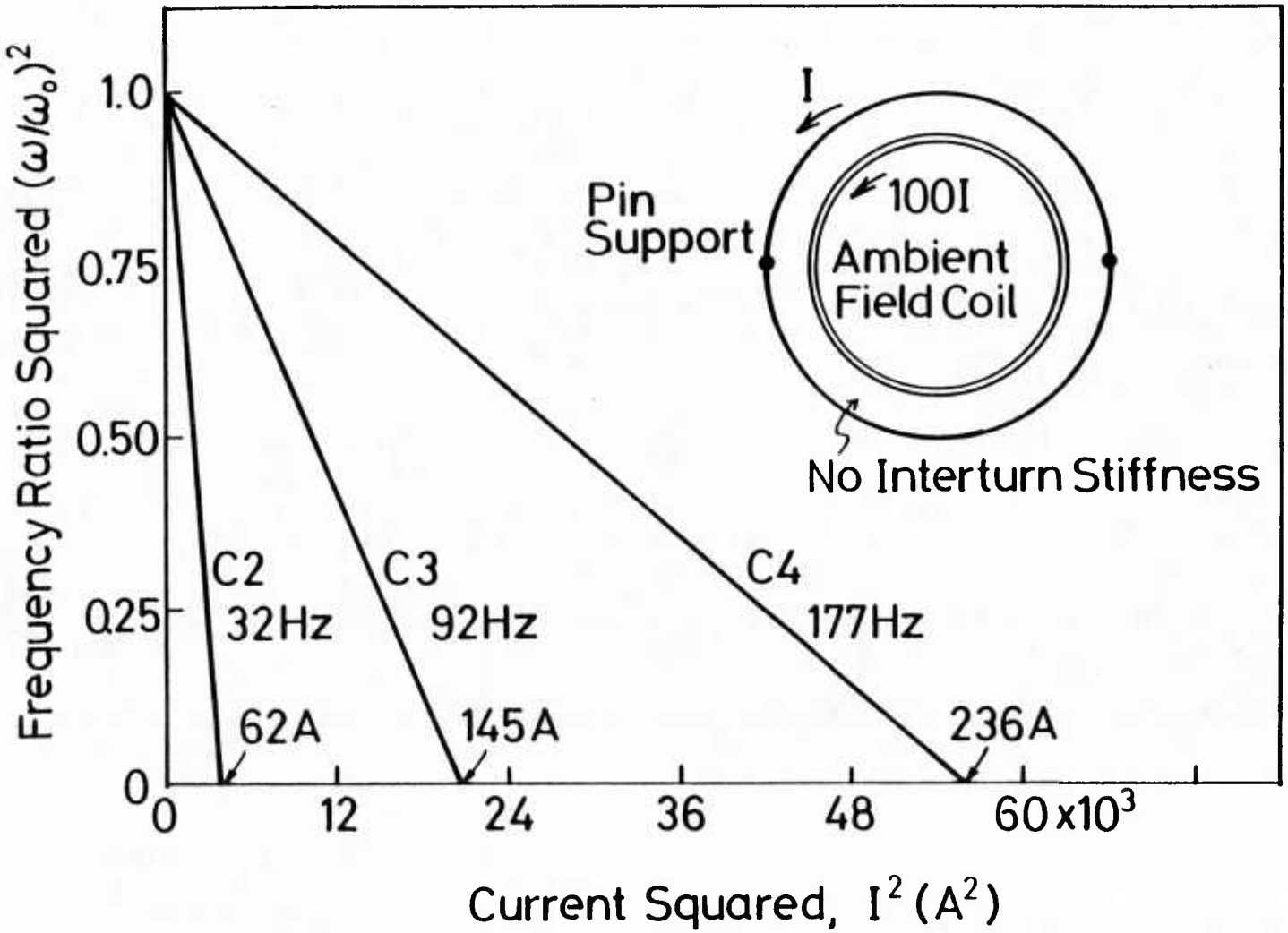

Figure 4.7 Theoretical current-frequency dispersion curves for one-ring model without interturn springs

under several different conditions. The experimental data are from the Southwell plot of the static test (Figure 3.7). The theoretical values were calculated under different conditions for the second, third and fourth circumferential modes using equation (4.2.26).

The effect of the magnetic stiffness on the critical buckling current is significant. The calculated values are close to those obtained from the experiment. When only the initial compression is taken into account, the critical current is lower for the higher circumferential modes. This will be explained in the next section.

The calculated critical current when the initial compression is neglected is shown at the bottom. For the second mode the value is close to that under the existence of both the initial tension and magnetic stiffness. Therefore, the critical current is more likely to be governed by the magnetic stiffness for the lower circumferential modes, while for the higher modes the effect of the initial tension is larger.

As for the effect of the circumferential springs, it is negligible for the higher modes. As a matter of fact, the buckling current is identical for the fourth mode, and the experimental values are closer to the values when the circumferential springs are neglected.

The theoretical frequency-current dispersion curves are shown in Figure 4.8 along with the experimental data. The rate of dispersion is higher for the theoretical values than the experimental ones, and the natural frequencies associated with the same mode are different. In the analysis the discretized springs used in the experiment were replaced by the elastic foundation. Also, the effect of the nonlinearity of the springs may have caused these results.

Table 4.2 Experimental and theoretical critical buckling currents for one-ring model with springs

Circumferential Mode	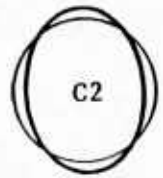	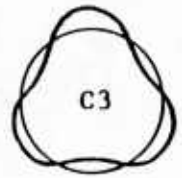	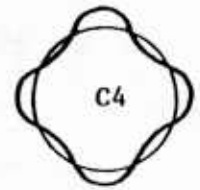
	(A)	(A)	(A)
Experiment (by Southwell plot, Figure 3.11)	141 , 151	-----	225
Theory [eqn. (4.2.26)]			
w/Initial Compression			
w/Magnetic Stiffness			
w/Torsional Spring	169	191	257
w/o Torsional Spring	145	186	257
w/o Magnetic Stiffness			
w/Torsional Spring	389	311	354
w/o Torsional Spring	339	301	351
w/o Initial Compression			
w/Magnetic Stiffness	185	243	378

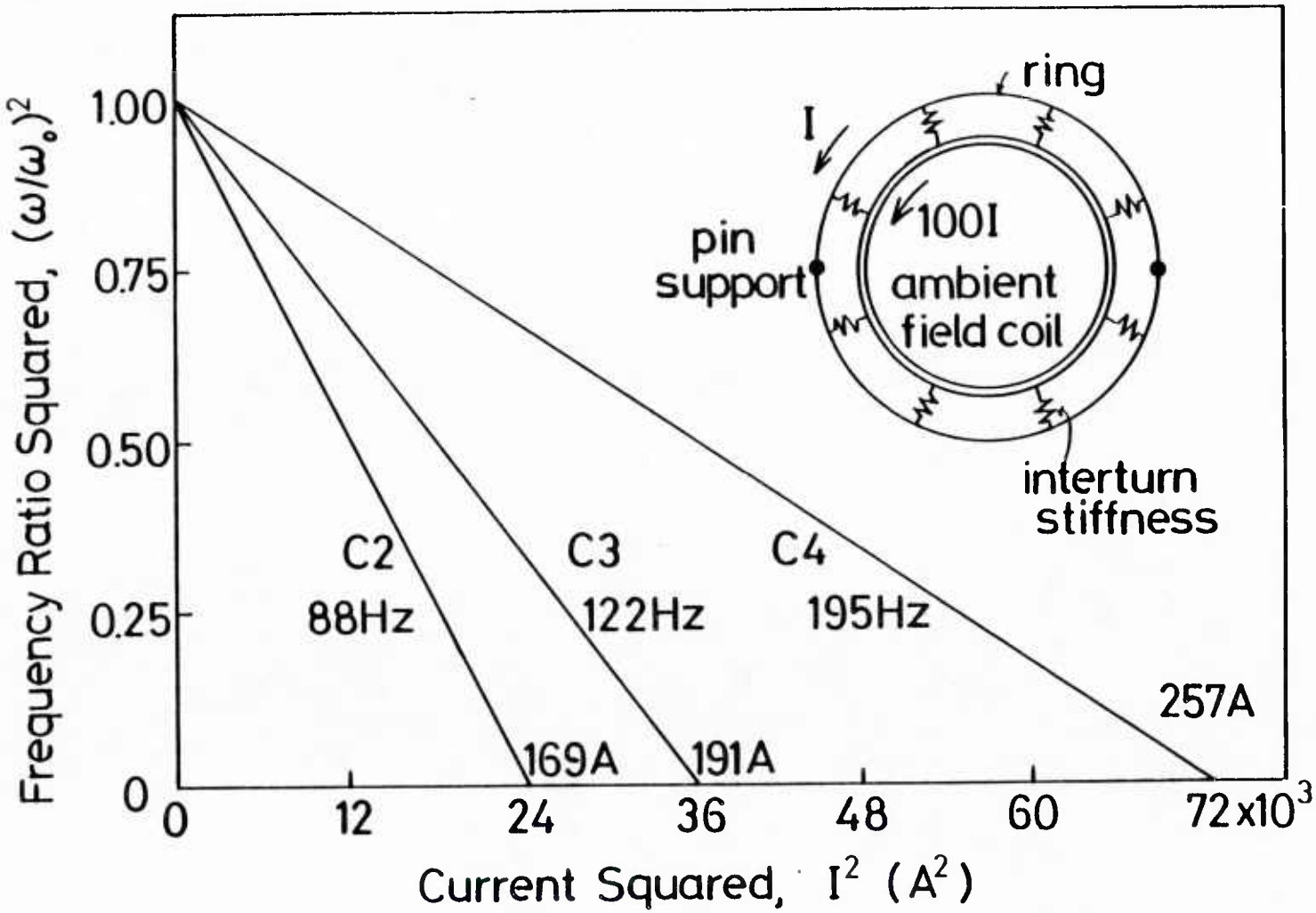

Figure 4.8 Theoretical current-frequency dispersion curves for one-ring model with interturn springs

4.2.3 Nondimensionalization

The critical buckling current for a ring in a transverse magı field depends on the spring constants and the magnetic field gra as well as the size. In this section their effects are discusse

In this analysis the effect of the circumferential springs i neglected. First, the effect of the radial spring is discussed, followed by the effect of the magnetic stiffness, and finally bo the effects will be taken into account.

The governing equation for the static case is given from equ (4.2.23) as

$$\frac{D}{R^4} n^2(n^2 - 1)^2 - \frac{B_o I}{R} n^2(n^2 - 1) + n^2 k_x - \Gamma I n^2 = 0$$

where the directions of the current and magnetic field are set that the resulting force is inward. When there is neither the i turn nor magnetic stiffness, the buckling load, which is the mul cation of the current and the magnetic field, denoted by P_o, is given rather simply.

$$P_o = B_o I$$
$$= \frac{(n^2 - 1)D}{R^3}$$

The lowest buckling load is given when the mode n is two and

$$P_{o,2} = \frac{3D}{R^3}$$

and this value is the same as given by Timoshenko and Gere (1961). This value is set as a standard P_e. The other buckling loads are expressed as a ratio to this value and nondimensionalized. For example, without the mechanical and magnetic stiffness, the nondimensionalized critical buckling loads for the other modes are

$$\text{(3rd mode)} \quad P_{o,3} = \frac{8D}{R^3} = \frac{8}{3} P_e \tag{4.2.31}$$

$$\text{(4th mode)} \quad P_{o,4} = \frac{15D}{R^3} = 5P_e \tag{4.2.32}$$

and so on.

If only the interturn radial stiffness is assumed to exist, then the buckling load is

$$\begin{aligned} P_{sp} &= B_o I \\ &= \frac{(n^2 - 1)D}{R^3} + \frac{kR}{n^2 - 1} \\ &= P_e \frac{n^2 - 1}{3} + \frac{1}{n^2 - 1} \frac{kR^4}{3D} \end{aligned} \tag{4.2.33}$$

and the nondimensional buckling load for each mode is a linear function of the nondimensional spring constant and is given as

$$\frac{P_{sp\cdot 2}}{P_e} = 1 + \frac{1}{3} \frac{kR^4}{3D} \tag{4.2.34}$$

$$\frac{P_{sp\cdot 3}}{P_e} = \frac{8}{3} + \frac{1}{8} \frac{kR^4}{3D} \tag{4.2.35}$$

$$\frac{P_{sp\cdot 4}}{P_e} = 5 + \frac{1}{15}\frac{kR^4}{3D} \quad . \tag{4.2.36}$$

The nondimensional critical loads are plotted against the nondimensional spring constant. The relationship between the buckling load and the deformational mode is shown in Figure 4.9. The lowest critical load does not necessarily associate with the lowest deformational mode. For example, when the nondimensional spring constant is 30, the lowest critical load is associated with the 3rd mode. The second lowest is the 4th mode, followed by the 2nd mode. This phenomena was seen in Table 4.2.

On the other hand, when only the magnetic stiffness exists, the governing equation may be rewritten as

$$\frac{D}{R^4} n^2(n^2 - 1)^2 - \frac{B_o I}{R} n^2(n^2 - 1) - \lambda B_o I n^2 = 0 \tag{4.2.37}$$

where λ is the ratio of the magnetic field gradient to the magnetic field and defined as

$$\lambda = \frac{\Gamma}{B_o} \quad . \tag{4.2.38}$$

The critical buckling load is then given as

$$\begin{aligned} P_{mag} &= B_o I \\ &= \frac{(n^2 - 1)D}{R^3} \cdot \frac{1}{1 + (1/n^2 - 1)\ \lambda R} \end{aligned} \tag{4.2.39}$$

or

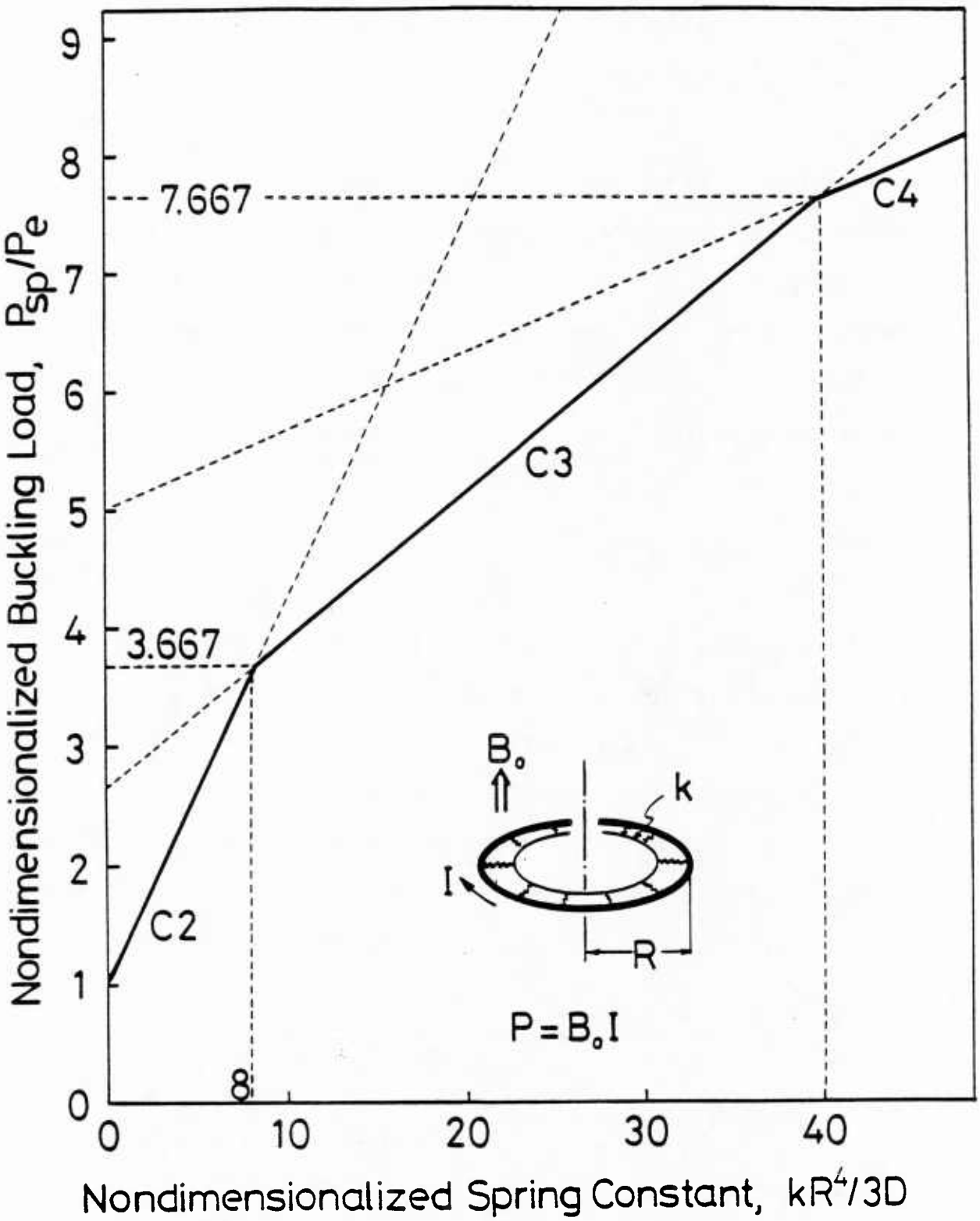

Figure 4.9 Nondimensionalized critical buckling vs. nondimensionalized spring constant for current carrying ring in transverse magnetic field

$$\frac{P_{mag}}{P_e} = \frac{n^2 - 1}{3} \cdot \frac{1}{1 + (1/n^2 - 1)\ \lambda R} \quad . \tag{4.2.40}$$

In Figure 4.10 the nondimensionalized critical load is plotted against the nondimensionalized magnetic stiffness for the different deformation modes. A sharp decrease of the buckling load is observed, particularly for the 2nd mode, as the magnetic stiffness increases.

Under the existence of both the mechanical and magnetic stiffness, the nondimensionalized buckling load is expressed as

$$\frac{P}{P_e} = \frac{n^2 - 1}{3} + \frac{1}{n^2 - 1}\,\frac{kR^4}{3D}\,\frac{1}{1 + (1/n^2 - 1)\ \lambda R} \quad . \tag{4.2.41}$$

The nondimensional buckling loads were plotted three-dimensionally as a function of both the nondimensional mechanical and magnetic stiffness in Figure 4.11. This graph shows the dependence of the buckling loads on both stiffnesses. For example, when the nondimensional spring constant is 30, the lowest mode is the 3rd and the 2nd mode is the highest if the magnetic stiffness is zero (Figure 3.9). However, as the magnetic stiffness increases the 2nd mode turns out to be the lowest mode.

4.3 Multi Ring Analysis

4.3.1 Derivation of Equations

In this section the equations are derived for the buckling and vibration of multi-concentric rings. The governing equations are basically the same as those for a single ring model. The major difference is the magnetic field on each ring is produced by the other rings and it depends on the movement of those rings. Also the mechanical

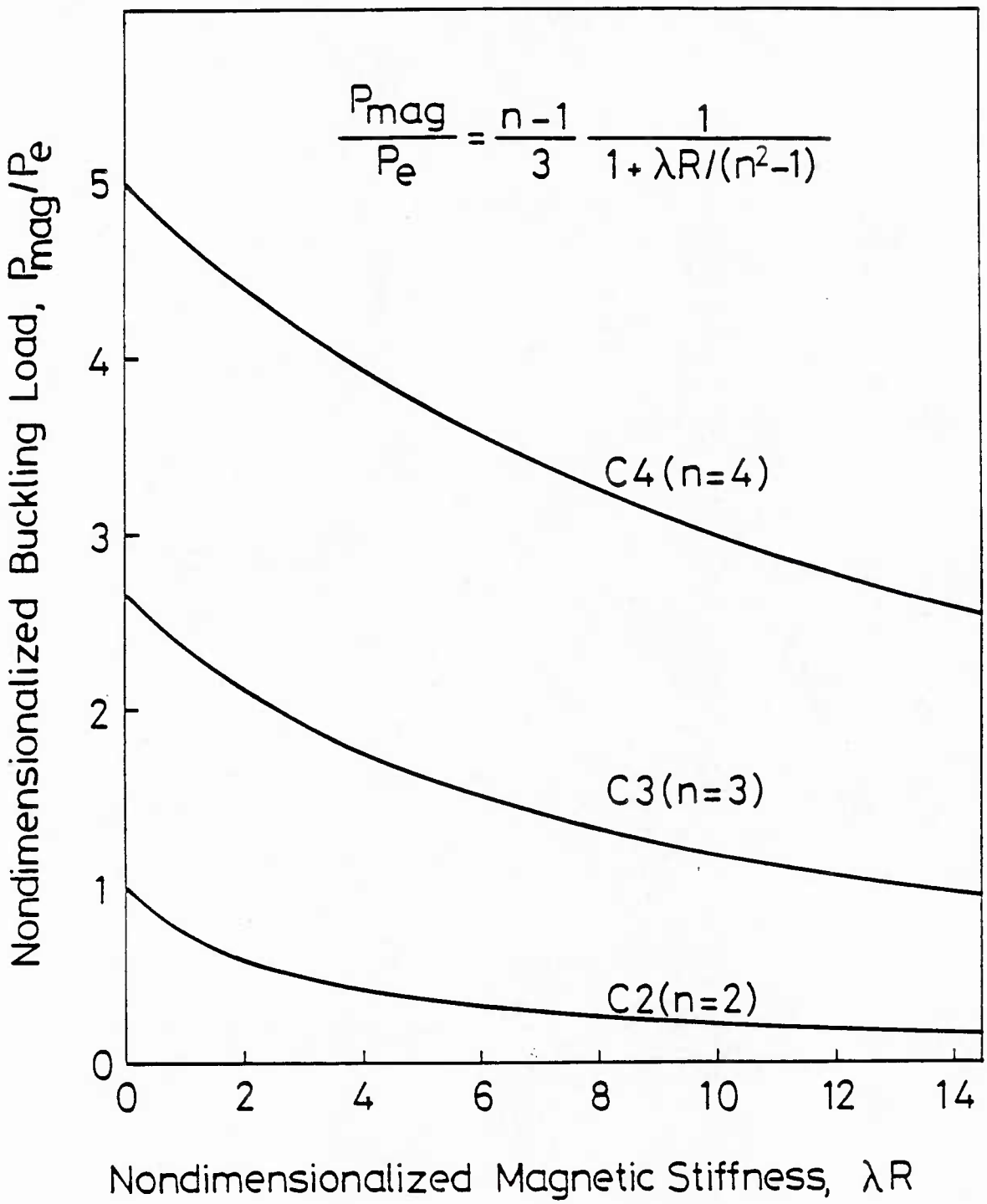

Figure 4.10 Nondimensionalized critical buckling load vs. nondimensionalized magnetic stiffness for current carrying ring in transverse magnetic field

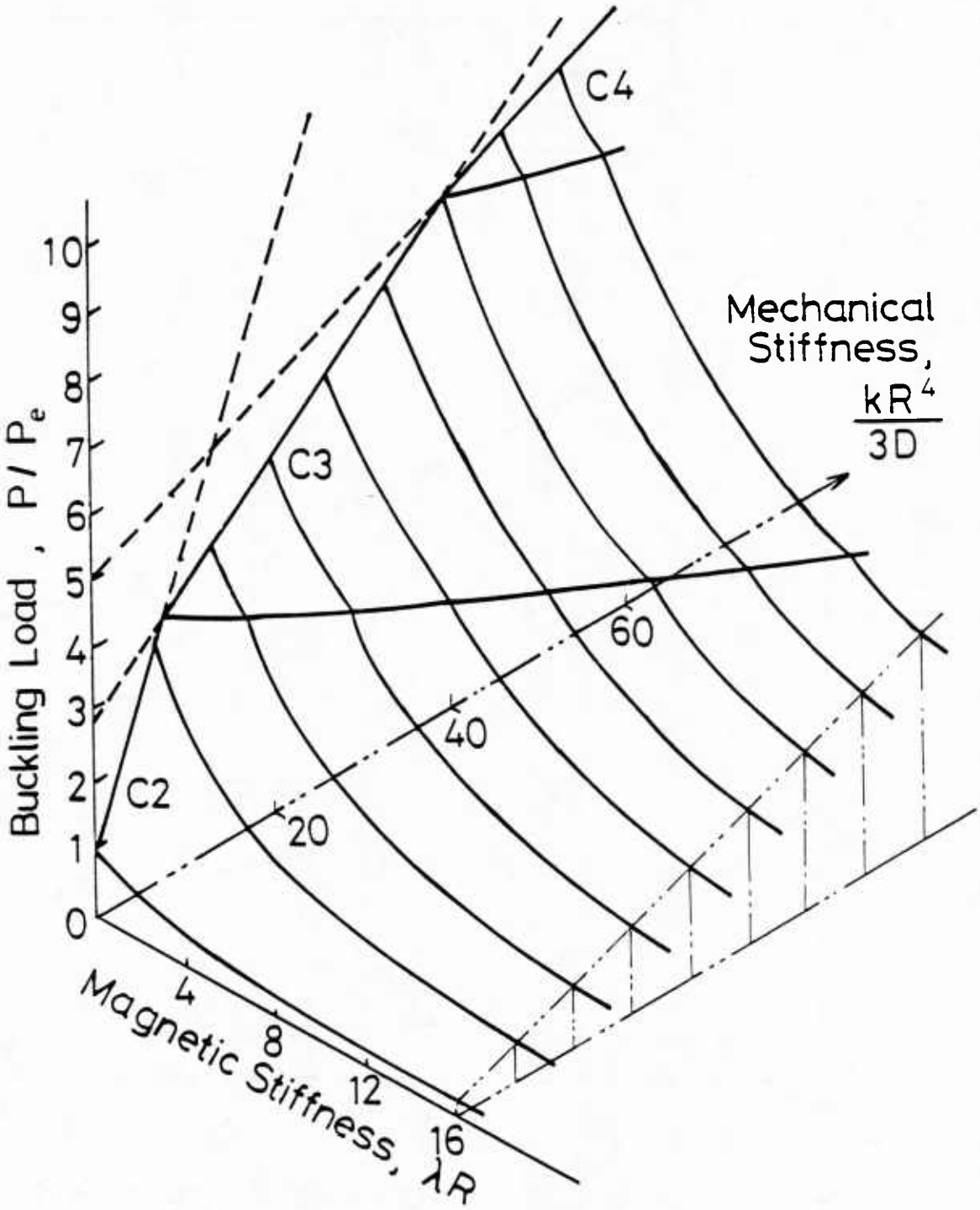

Figure 4.11 Three dimensional plot of nondimensionalized critical buckling load vs. mechanical stiffness vs. magnetic stiffness for current carrying ring in transverse magnetic field

force depends on the movement of the neighboring rings.

The model used in this analysis consists of N concentric rings of radii R_1 to R_N, which are connected by uniformly distributed elastic springs. The spring constants per unit length are k_x and k_z for the radial and circumferential directions.

The governing equation for the i-th ring is the same as that of a single ring and given by eqn (4.2.13) as

$$D\left(u_i^{(5)} + \frac{2}{R_i^2} u_i^{(3)} + \frac{u_i^{(1)}}{R_i^4}\right) + T_{o_i}\left(u_i^{(3)} + \frac{u_i}{R_i^2}\right) + f_{x_i}^{(1)}$$

$$- \frac{f_{z_i}}{R_i} = m \frac{\partial^2}{\partial t^2}\left(u_i^{(1)} - \frac{w_i}{R_i}\right) \qquad (4.3.1)$$

where $u^{(n)} = \partial^n u/\partial z^n$.

The force term $(f_{x_i}^{(1)} - f_{z_i}/R)$ may be divided into two components. In this case, too, the perturbed magnetic forces due to the ring movement in the uniform magnetic field cancel out (Section 4.2.1), which leaves the mechanical constraints and the magnetic stiffness due to the magnetic field gradient.

<u>Mechanical constraints</u>: The forces due to the mechanical springs are affected only by the movement of the neighboring rings. The radial and circumferential components are expressed as

(radial direction)

$$f_{sp\cdot x} = -k_x(u_i - u_{i-1}) - k_x(u_i - u_{i+1}) = k_x(u_{i-1} - 2u_i + u_{i+1}) \qquad (4.3.2)$$

(circumferential direction)

$$f_{sp\cdot z} = k_z(w_{i-1} - 2w_i + w_{i+1}) \qquad (4.3.3)$$

Magnetic stiffness: The magnetic stiffness is expressed as the magnetic field gradient at the i-th ring. The gradient is divided into two components; one due to the movement of the i-th ring itself and another due to the movement of the other rings.

1) Magnetic stiffness due to the i-th ring movement

The magnetic field gradient coefficient $\gamma_{i,j}$ is given by equation (2.1.58) as

$$\gamma_{i,j} = \frac{\mu}{2\pi} \frac{1}{R_i(R_j + R_i)} \left[\frac{R_j^2 + R_i^2}{(R_j - R_i)^2} E - K \right] \tag{4.3.4}$$

and $\gamma_{i,j} I$ implies the magnetic field gradient at i-th ring position produced by j-th ring due to the movement of the i-th ring.

2) Magnetic stiffness due to the movement of the other rings

In this case the magnetic field coefficient $\beta_{i,j}$ is given by equation (2.1.59) as

$$\beta_{i,j} = -\frac{\mu}{2\pi} \frac{2R_j}{(R_j + R_i)(R_j - R_i)^2} E \tag{4.3.5}$$

and $\beta_{i,j} I$ implies the magnetic field gradient at i-th ring produced by j-th ring due to the movement of the j-th ring.

Then the total magnetic stiffness is expressed as

$$f_{mag,x_i} = \sum_{\substack{j=1 \\ j\neq i}}^{N} \gamma_{i,j} I^2 u_i + \sum_{\substack{j=1 \\ j\neq i}}^{N} \beta_{i,j} I^2 u_j$$

$$= \gamma_i I^2 u_i + \sum_{\substack{j=1 \\ j\neq i}}^{N} \beta_{i,j} I^2 u_j \quad . \tag{4.3.6}$$

Therefore, the total distributed force on the i-th ring is given as

$$f'_{x_i} - \frac{f_{z_i}}{R_i} = k_x(u'_{i-1} - 2u'_i + u'_{i+1}) + \gamma_i I^2 u'_i + \sum_{\substack{j=1 \\ j\neq i}}^{N} \beta_{i,j} I^2 u'_j$$

$$- \frac{k_z}{R_i}(w_{i-1} - 2w_i + w_{i+1}) \quad . \tag{4.3.7}$$

The initial tension on the i-th ring is calculated by using equation (4.2.3) as

$$T_o = \sum_{\substack{j=1 \\ j\neq i}}^{N} B_{i,j} I = \sum_{\substack{j=1 \\ j\neq i}}^{N} \frac{\mu}{2\pi}\left[\frac{K}{R_j + R_i} + \frac{E}{R_j - R_i}\right] I^2 = \alpha_i I^2 \quad . \tag{4.3.8}$$

After substituting equations (4.3.7) and (4.3.8) into equation (4.3.1) the same procedure used in section 4.2.1 yields the governing equation for the i-th ring as a function of circumferential displacement vector $\{w_i\}$ which is proportional to radial displacement vector $\{u_i\}$.

$$\frac{D}{R_i^5} n^2(n^2 - 1)^2 w_i + \frac{\alpha_i}{R_i^2} n^2(n^2 - 1) I^2 w_i - k_x n^2\left(\frac{w_{i-1}}{R_{i-1}} - 2\frac{w_i}{R_i} + \frac{w_{i+1}}{R_{i+1}}\right)$$

$$- \frac{k_z}{R_i}(w_{i-1} - 2w_i + w_{i+1}) - \gamma_i n^2 I^2 \frac{w_i}{R_i} - \sum_{\substack{j=1 \\ j\neq i}}^{N} \beta_{i,j} I^2 n^2 \frac{w_i}{r_j}$$

$$= \frac{m\omega^2}{R_i}(n^2 + 1) w_i \quad . \tag{4.3.9}$$

The final governing equation for the multi-ring system is obtained by assembling equation (4.3.9) for N rings. This is expressed in the matrix form as follows

$$\left[[K_1] + [K_2] + \{[B_1] + [B_2]\}I^2\right]\{w\} = m\omega^2\{w\} \tag{4.3.10}$$

where

$[K_1]$: bending stiffness matrix (diagonal)

$$[K_1]_{ii} = \frac{D}{R^5} n^2(n^2 - 1)^2 \tag{4.3.11}$$

$[K_2]$: mechanical stiffness matrix

$[B_1]$: magnetic field coefficient matrix (diagonal)

$$[B_1]_{ii} = \frac{\alpha_i}{R_i^2}(n^2 - 1)^2 \tag{4.3.12}$$

and

$[B_2]$: magnetic field gradient coefficient matrix.

The components of matrices $[K_2]$ and $[B_2]$ are shown in the Appendix. The matrix $[K_2]$ is modified by changing the spring constants per unit length to the spring constant per radian to get the symmetry. The matrix $[B_2]$ is also symmetric because

$$[B_2]_{ij} = \frac{\beta_{i,j}}{R_j} = -\frac{\mu}{2\pi}\frac{2}{(R_j + R_i)(R_j - R_i)^2}E$$

$$= \frac{\beta_{j,i}}{R_i} = [B_2]_{ji} \quad . \tag{4.3.13}$$

The boundary conditions of the system are imposed on the matrices $[K_1]$, $[B_1]$ and $[B_2]$. If the inner or outer ring is fixed, then the equation of the motion for that ring will not be included in equation (4.3.10). Instead it will be considered as an ambient field coil and the effect

of the magnetic field on the system will be imposed in matrices $[B_1]$ and $[B_2]$. The condition on how the inner or outer ring is connected, for example whether it is connected to the foundation or only to the neighboring ring, is imposed on the component $[K_2]_{11}$ or $[K_2]_{NN}$.

The equation (4.3.10) is interpreted as a double eigenvalue problem. If the frequency is set to be zero, then the equation yields

$$\left[([K_1] + [K_2]) - (-[B_1] - [B_2])I^2\right]\{w\} = 0 \tag{4.3.14}$$

or

$$|([K_1] + [K_2]) - (-[B_1] - [B_2])I^2| = 0 \tag{4.3.15}$$

for arbitrary set of $\{w\}$. The critical buckling current of the system is then given as a square root of the eigenvalue of this determinant. If the eigenvalue of I^2 is negative, then the system is stable for the corresponding eigen-vector.

On the other hand, if the frequency is not zero, then equation (4.3.10) yields

$$\left[\{[K_1] + [K_2] + ([B_1] + [B_2])I^2\} - m\cdot\omega^2\right]\{w\} = 0 \tag{4.3.16}$$

or

$$|\{[K_1] + [K_2] - ([B_1] + [B_2])I^2\} - m\cdot\omega^2| = 0 \quad . \tag{4.3.17}$$

for the arbitrary set of $\{w\}$. Then the natural frequency for the given current is given as a square root of the eigenvalue. When the current

is zero, the equation (4.3.15) gives the natural frequency of the system. Since in this case the determinant

$$\frac{1}{m}\left|[K_1] + [K_2]\right| \tag{4.3.18}$$

is real, symmetric and positive definite, all the eigenvalues are real and positive.

The current-frequency dispersion curves can be obtained by calculating the eigenvalues as a function of the current. For the unstable mode, the frequency decreases and approaches to zero as the current is increased. If the current is higher than the certain critical value, then the corresponding eigenvalue or the squared frequency becomes negative. However, this is purely mathematical and has no physical meanings.

In this study a computer program was written to calculate the critical buckling current and the current-frequency dispersion relationship. The iteration method was used to calculate the eigenvalues.

4.3.2 Comparison Between Analytical and Experimental Results

The critical buckling current and the current-frequency dispersion curves were obtained for the models simulating the experiment. The effect of the ambient field coil was included in the diagonal elements of the matrices $[B_1]$ and $[B_2]$. A discussion of these analytical results and a comparison with the experimental results is given for the in-plane deformation, since the out-of-plane motion was prevented in experiments.

Two-Ring Model

Since the critical buckling current could not be obtained from the static test experimentally, the comparison of results on the dynamic

test is given here. The theoretical results for the selected modes are listed in Table 4.3 along with the natural frequencies obtained experimentally.

The modes chosen are the circumferential 2nd and 4th modes. They are represented by C2 and C4. For each circumferential mode there are two radial modes represented by R1 and R2. For the Cn or circumferential nth mode the n sinusoidal waves are along the circumference. In the two ring cases, the two rings deform in the same way in the R1 mode, which they move oppositely in the R2 mode.

The natural frequencies 70 Hz and 130 Hz are considered to be those of the C3R1 and C4F1 modes, respectively, since the directions of the movement were the same. The current-frequency dispersion curves obtained theoretically are shown in Figure 4.12. A strong nonlinearity in the ω^2-I^2 function is observed in this graph. The slopes of the dispersion curves do not necessarily show the critical buckling currents. The slope of the C4R1 mode when the current is low indicates the higher critical current but actual critical current for that mode is lower than that. The curves of the C2R2 and C4R2 modes sow the opposite tendencies.

For the R1 mode, the magnitude of vibration for the outer ring is higher when the current is small. As the current increases the magnitude of vibration of the inner ring increases. The magnitude of the inner ring in the C4R1 mode becomes almost twice that of the outer ring near the critical buckling current although it is about one third when the current is low. On the other hand for R2 modes, the magnitude of the inner ring decreases as the current increases.

Table 4.3 Comparison of experimental and theoretical critical currents and natural frequencies for two-ring model with interturn stiffness

Circumferential Mode	C2		C4	
Radial Mode	R1	R2	R1	R2
Critical Current (Static)				
Experiment	-----	-----	-----	-----
Theory	151 A	348 A	270 A	391 A
$w_1 : w_1$ [a]	0.8:1	-0.3:1	2.2:1	-0.1:1
Natural Frequency (Dynamic)				
Experiment	70 Hz	-----	130 Hz	-----
Theory	56 Hz	134 Hz	162 Hz	215 Hz
$w_1 : w_2$ [b]	0.5:1	-1.6:1	0.3:1	-2.8:1

[a]Ratio of the extreme deformation of the inner ring to the outer ring at the buckling.

[b]Ratio of the extreme deformation of the inner ring to the outer ring when the current is zero.

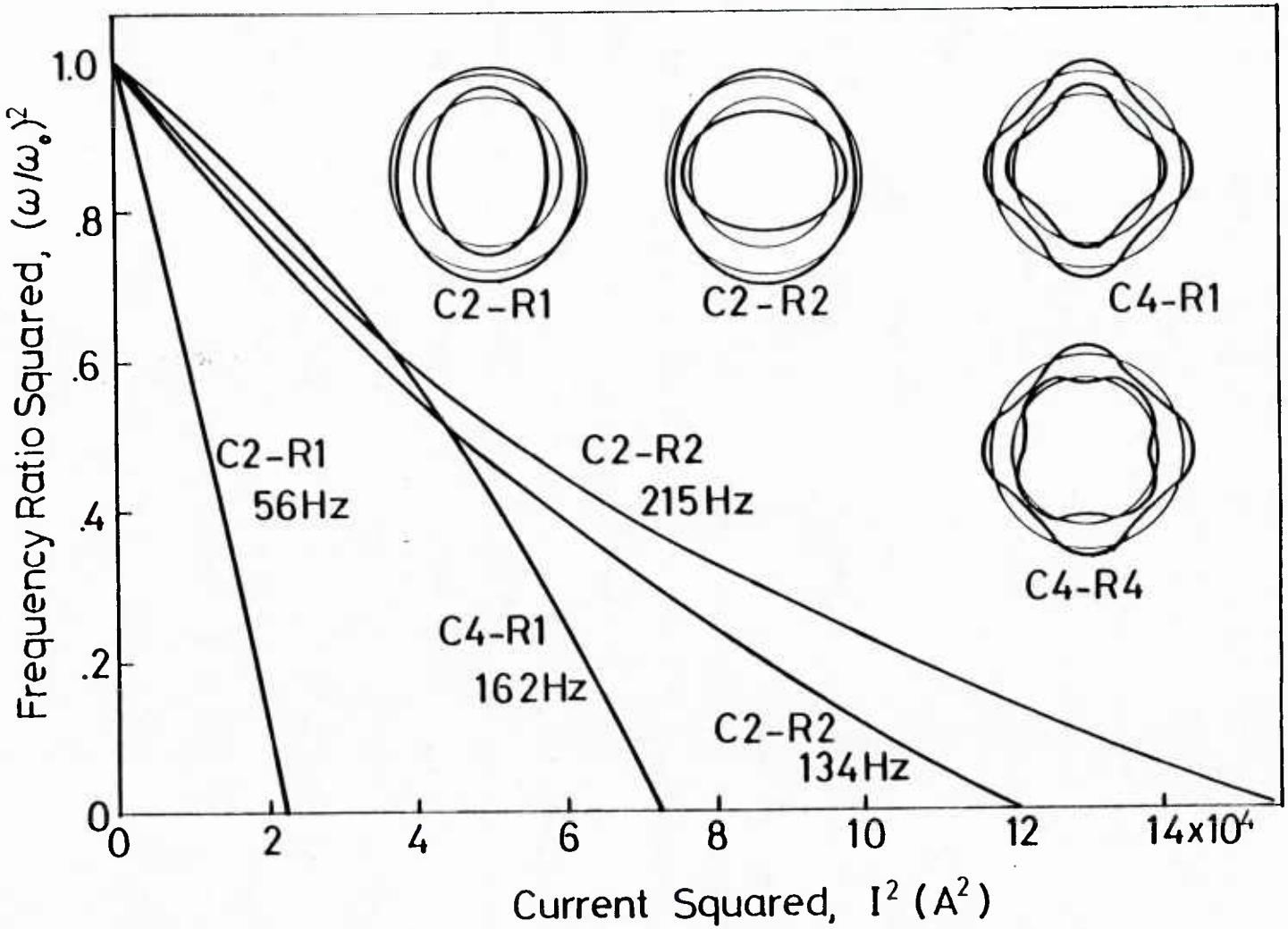

Figure 4.12 Theoretical current-frequency dispersion curves for two-ring model with interturn stiffness

Three-Ring Model

The analytical results of the critical buckling current of the model is shown in Table 4.4. The eigenvector and frequency corresponding to each mode are also listed.

As to the static result, three different buckling current were obtained experimentally by the Southwell plots. They are

Inner ring. . . . . 134 A, 223 A

Middle ring . . . . . 195 A

Since all rings deformed in the same direction those results correspond to the R1 modes. These three values are close to theoretical buckling currents of the C2R1, C3R1 and C4R1 modes.

The current-frequency dispersion curves obtained analytically are shown in Figures 4.13 and 4.14 for the circumferential second and fourth modes. The significant nonlinearity is observed particularly in the fourth mode. Since this kind of nonlinearity is not obvious when the high ambient field is absent (section 4.3.3), this nonlinearity is due to the ambient field coil. To compare the theoretical and experimental results, their dispersion curves are plotted for the low current region in Figure 4.15. They show the qualitative agreement of the decrease in frequency with increase to the current. The experimental lowest mode of 50 Hz seems to correspond to the C2R1 mode though the dispersion rates differ.

Table 4.4 Theoretical critical currents, natural frequencies and deformation ratios of the three ring model with interturn stiffness (simulating experiment)

Radial Mode / Circumferential Mode	R1		R2		R3	
C1 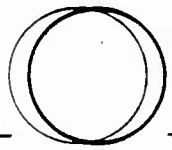	179 A	36 Hz	420 A	104 Hz	858 A	151 Hz
	0.6	0.4	-0.4	-1.0	0	2.0
	0.8	0.7	0.5	0.7	-0.6	-2.4
	1.0	1.0	1.0	1.0	1.0	1.0
C2 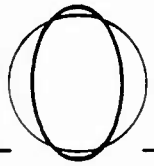	145 A	42 Hz	288 A	102 Hz	546 A	145 Hz
	0.6	0.3	-0.4	-1.1	0	2.2
	0.9	0.7	0.5	-0.7	-0.6	-2.4
	1.0	1.0	1.0	1.0	1	1.0
C3 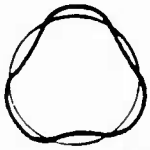	201 A	79 Hz	305 A	126 Hz	473 A	163 Hz
	1.5	0.2	-0.2	-1.1	0	3.1
	1.2	0.6	0.7	1.1	-0.6	-2.8
	1.0	1.0	1.0	1.0	1.0	1.0
C4 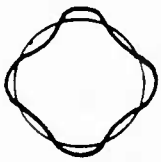	272 A	138 Hz	395 A	182 Hz	506 A	217 Hz
	6.0	0.1	-0.2	-1.0	0	8.6
	2.0	0.4	1.0	-2.0	-0.4	-4.4
	1.0	1.0	1.0	1.0	1.0	1.0

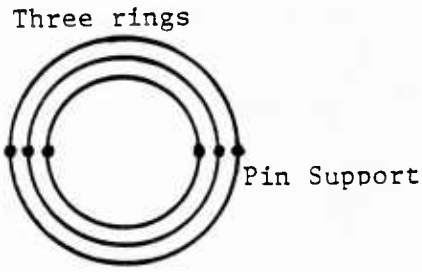

Critical Current	Natural Frequency
deformation ratio of three rings at buckling	deformation ratio of three rings at zero current

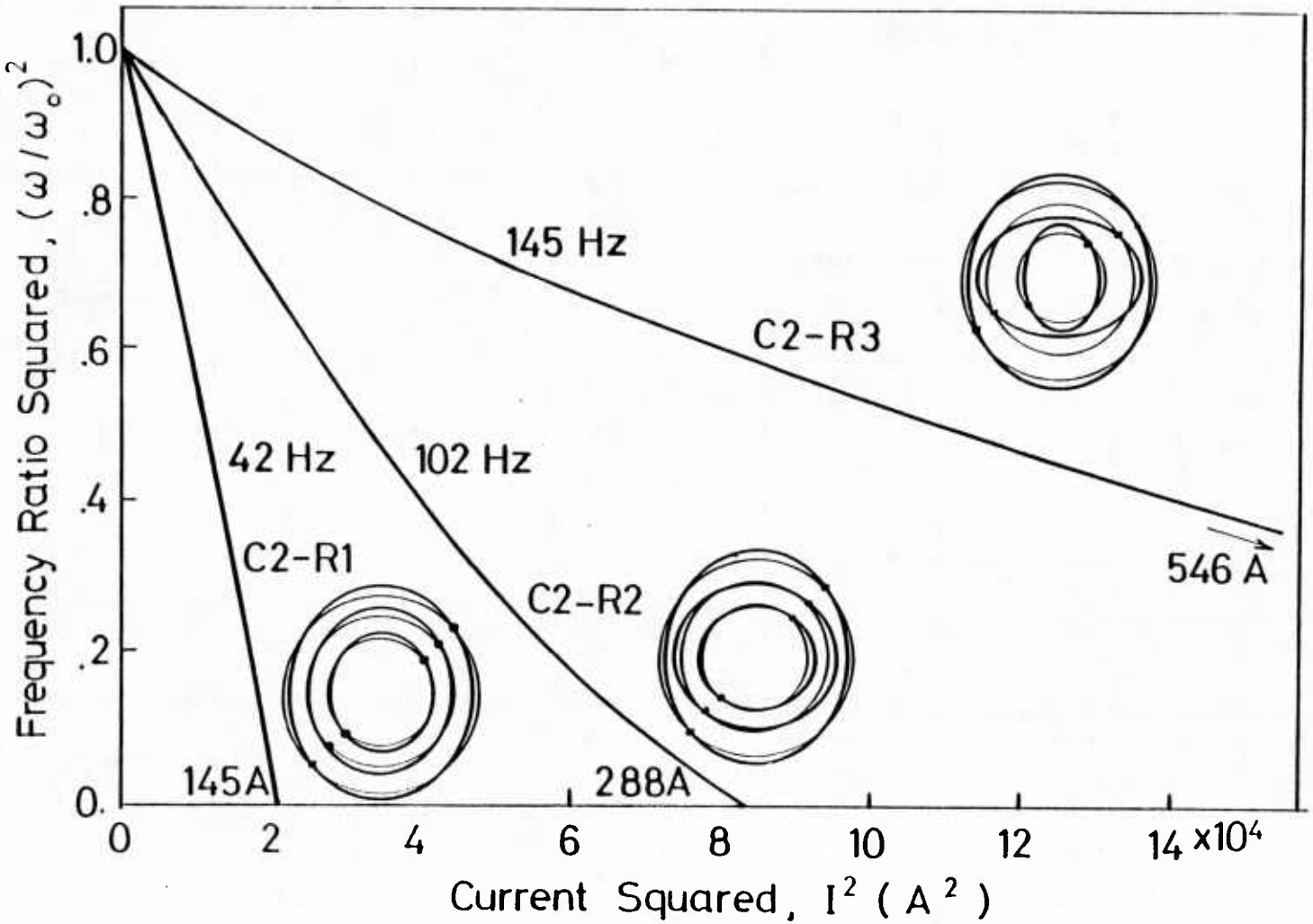

Figure 4.13 Theoretical current-frequency dispersion curves for circumferential second mode for three-ring model with interturn stiffness

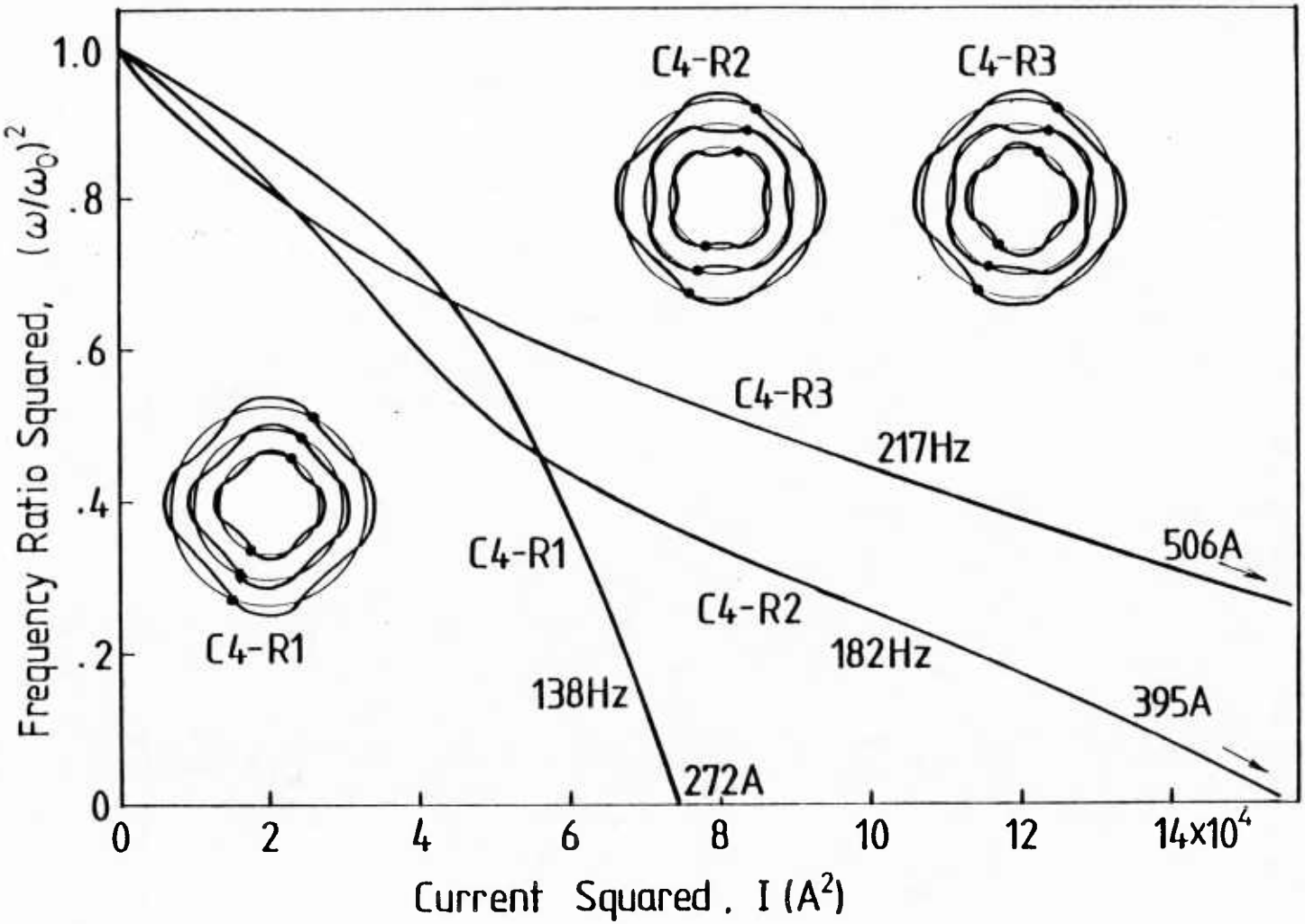

Figure 4.14 Theoretical current-frequency dispersion curves for circumferential fourth mode for three-ring model with interturn stiffness

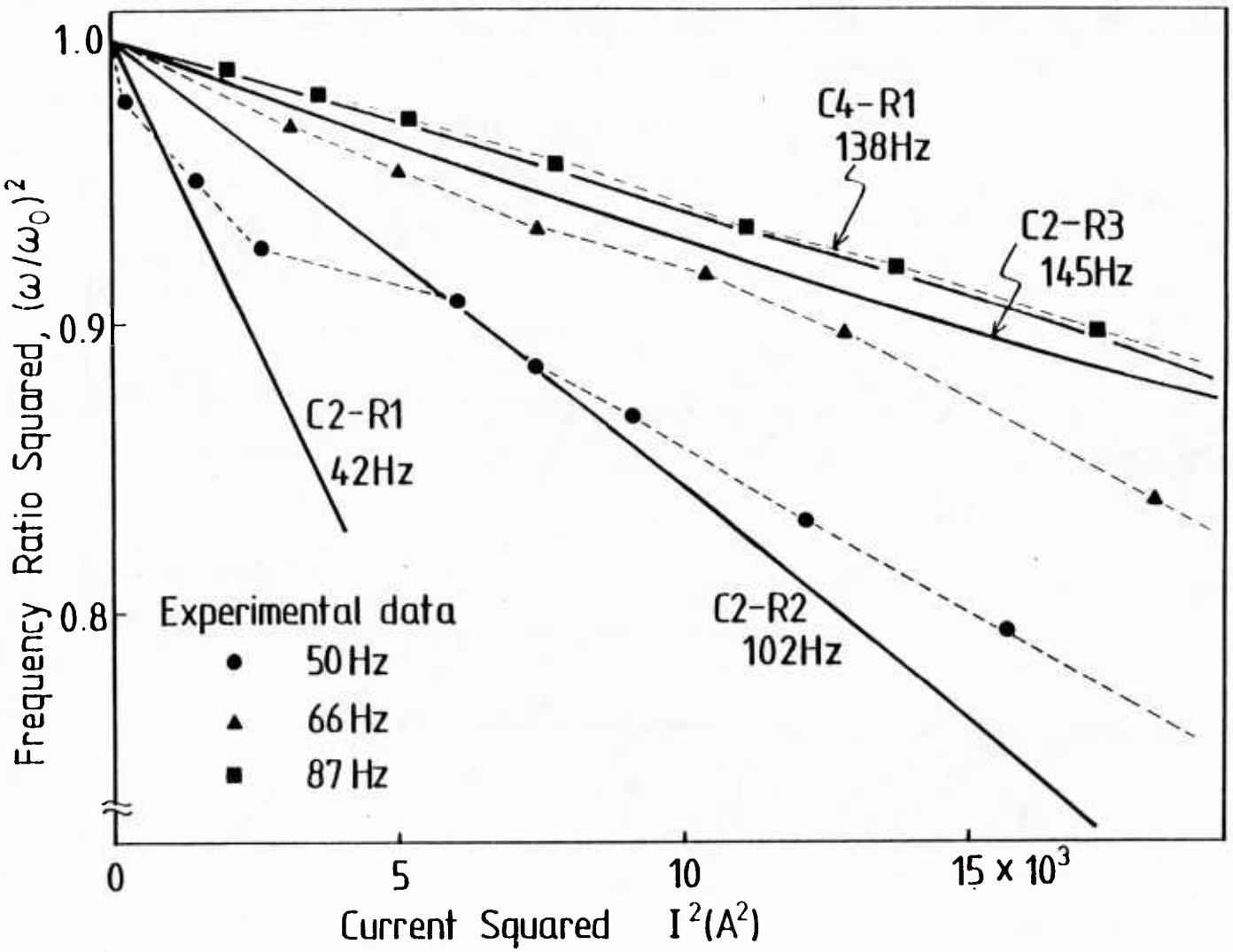

Figure 4.15 Comparison of experimental and theoretical current-dispersion curves for the three-ring model with interturn stiffness

4.3.3 General Analysis

The critical buckling currents and the current dispersion curves were obtained for 3-, 7- and 10-concentric rings connected by mechanical springs. In this analysis the material constants of the rings and spring constants were of the same material used in the experiment.

Three-Ring Model

The radii of the concentric rings are 11, 12 and 13 cm. The neighboring rings are assumed to be connected by the same springs used in the experiment. Neither the inner nor the outer ring is connected to the foundation. The results of the static calculation is listed in Table 4.4. While the C2 modes are all unstable, the C3 modes have two unstable and one stable modes. For the circumferential modes higher than eight, there is only one unstable mode and the rest are stable.

These results are confirmed by the current-frequency dispersion curves in Figures 4.16, 4.17 and 4.18, which correspond to the circumferential second, third, and eighth modes, respectively. In the C2 modes, the frequencies decrease as the currents increase. In the C3 mode, the frequency corresponding to the R3 mode increases with the current. In the C8 mode, only the frequency associated with the R1 mode decreases with increase in the current.

As for the deflection, all rings deform in the same way in the R1 modes. As the circumferential mode gets higher, only the outer ring shows significant deflection.

The outer ring deforms in a different direction than the rest in the R2 modes, which show stability for the high circumferential modes. In the R3 modes, the deflection direction of the rings alternate.

Table 4.5 Theoretical critical buckling currents for three ring model with interturn stiffness

Radial Mode	R1	R2	R3
Circumferential Mode	(1-mass mode) (A)	(2-mass mode) (A)	(3-mass mode) (A)
C1 (rigid body motion)	0	965	-----
C2	334	1814	8519
C3	854	3214	-----
C4	1457	3257	-----
C5	2079	4910	-----
C6	2689	7933	-----
C7	3283	14883	-----
C8	3866	-----	-----
C9	4441	-----	-----
C10	5011	-----	-----
C11	5575	-----	-----
C12	6135	-----	-----
C13	6693	-----	-----
C14	7245	-----	-----
C15	7799	-----	-----
C16	8350	-----	-----
C17	8899	-----	-----
C18	9446	-----	-----

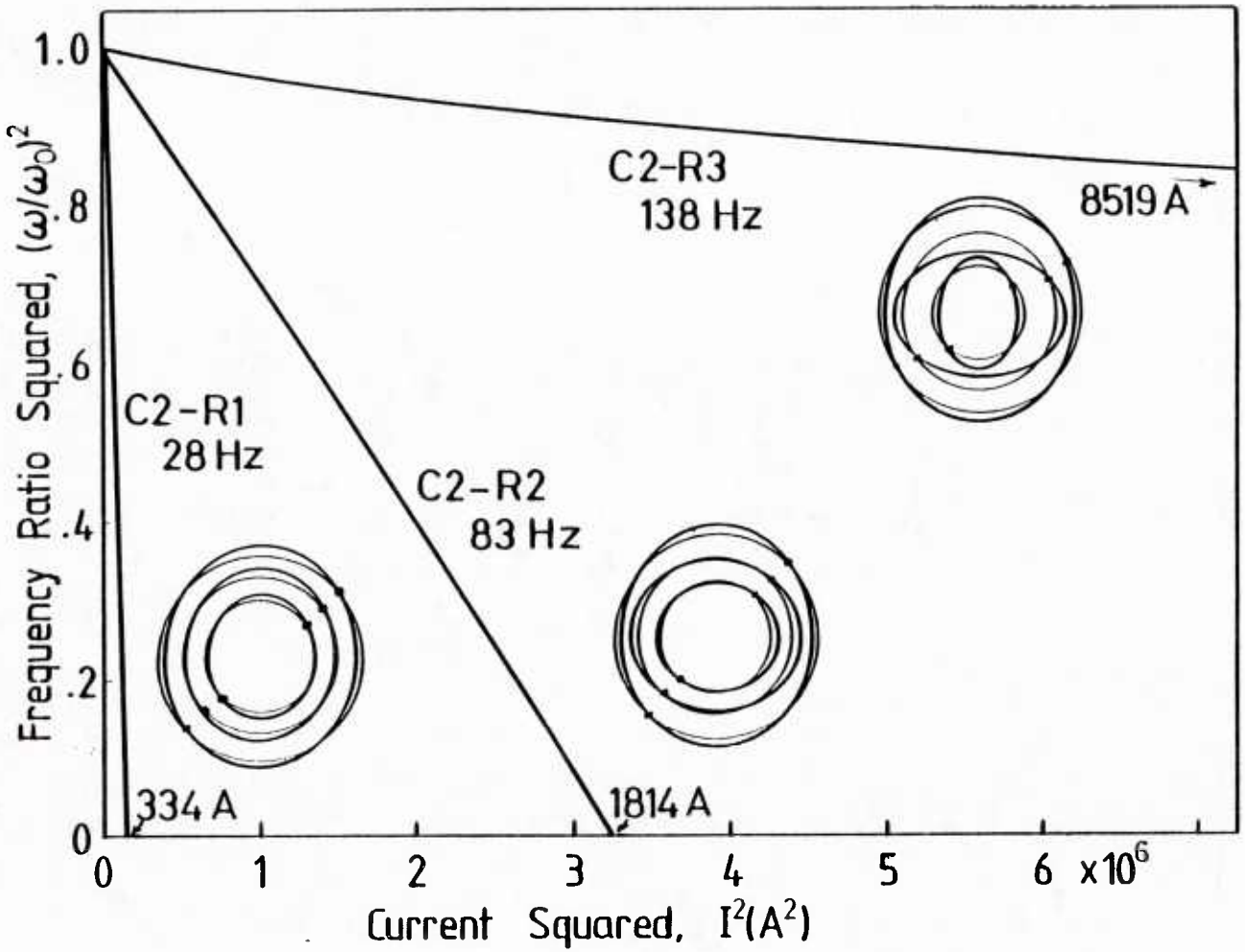

Figure 4.16 Theoretical current-frequency dispersion curves of circumferential second mode for three-ring model with interturn stiffness

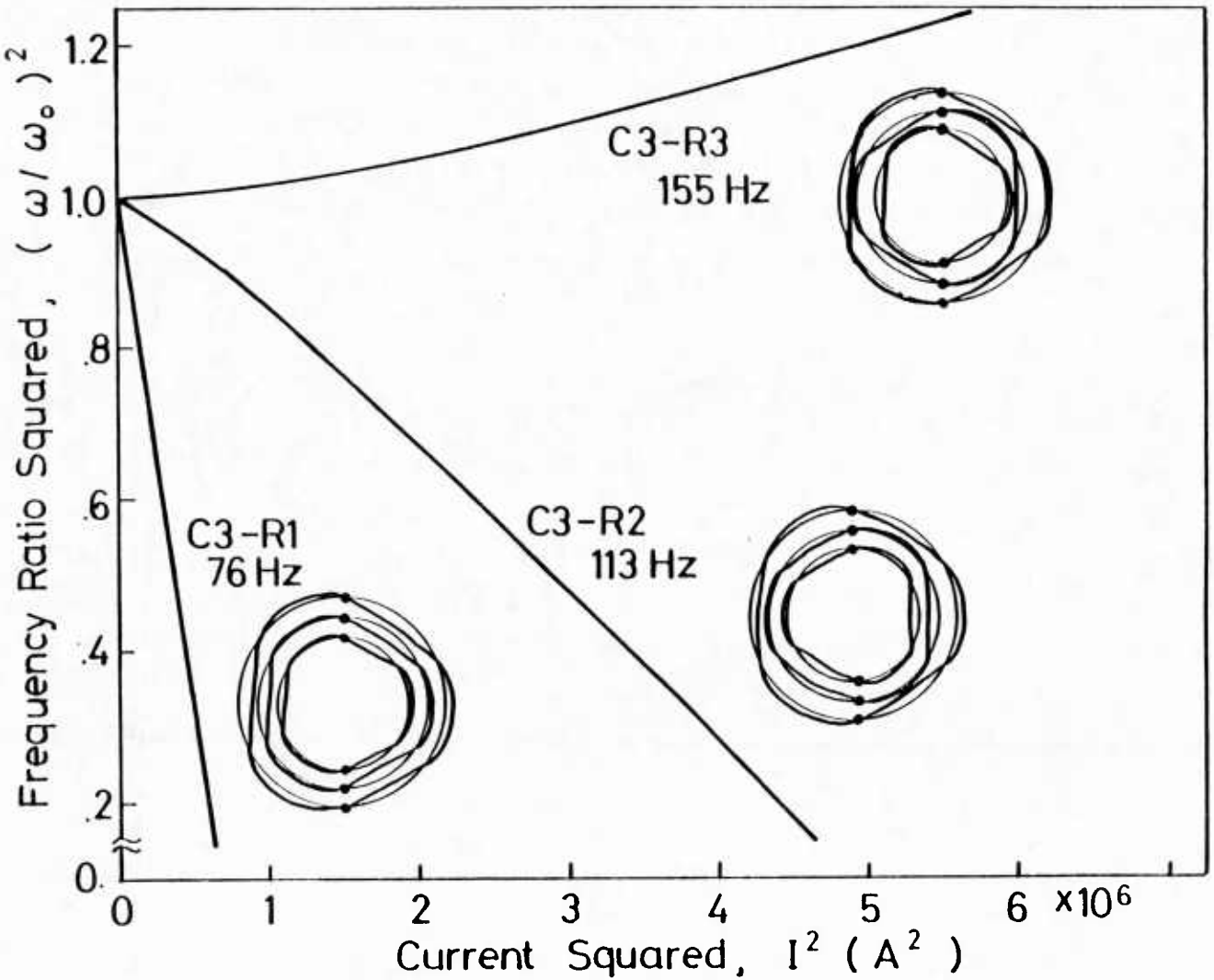

Figure 4.17 Theoretical current-frequency dispersion curves for circumferential third mode for three-ring model with interturn stiffness

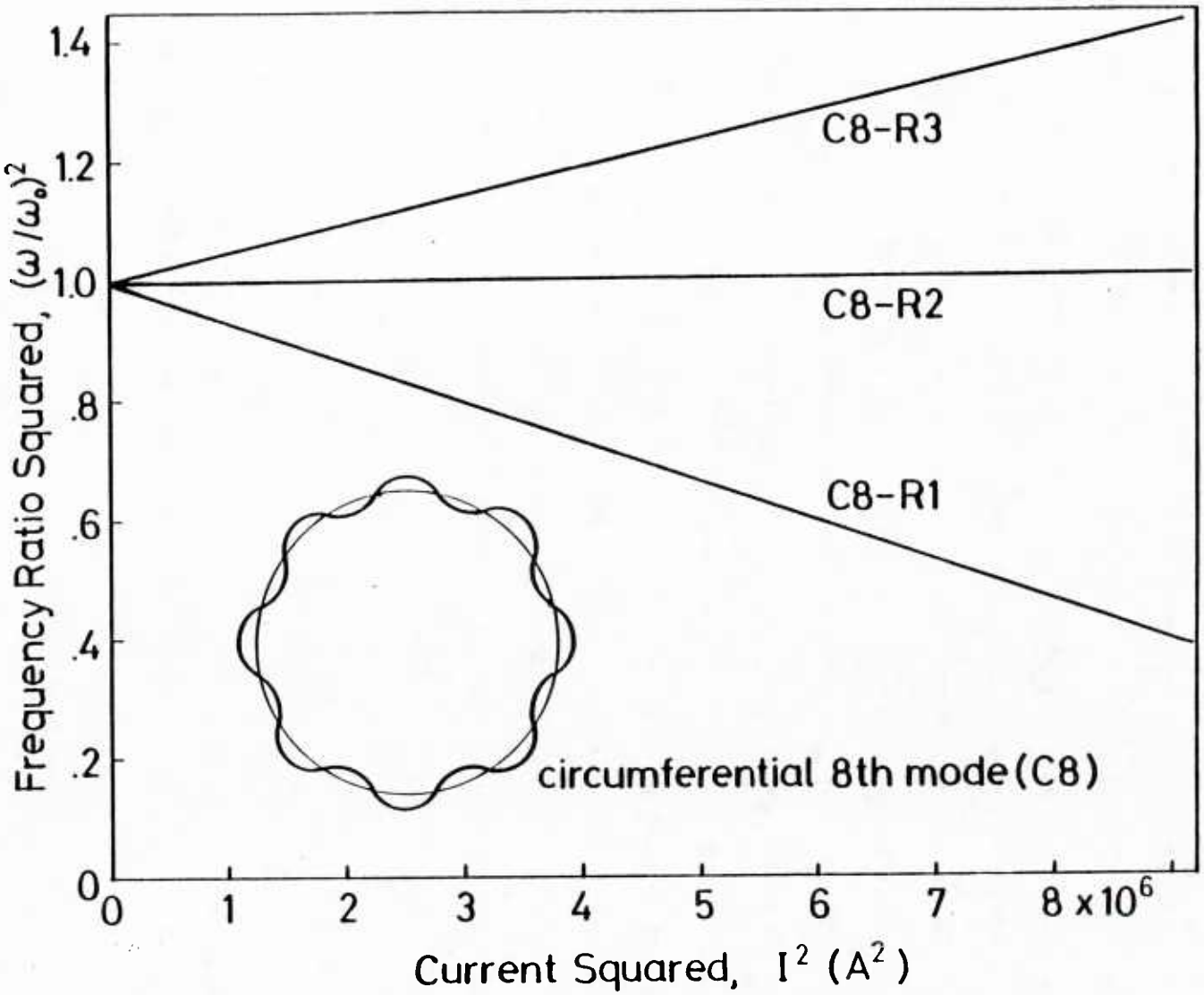

Figure 4.18 Theoretical current-frequency dispersion curves for circumferential eighth mode for three-ring model with interturn stiffness

Seven-Ring Model

In the 7-ring analysis, the radii of the rings range from 11 cm to 17 cm. Table 4.6 lists the critical buckling currents for the different circumferential and radial modes. For example, for the circumferential sixth mode the system is unstable for the lowest four radial modes. This is shown in Figure 4.19 by the current-frequency dispersion curves.

The magnitudes of the deformation of each ring when the current is zero and at buckling for the circumferential sixth mode are shown in Figure 4.20. For zero current, each radial vibration mode excites one ring more than the others. For the lowest frequency, the outermost ring vibrates the most, and the innermost ring vibrates the most at the highest frequency. As the current increases the lowest four modes show buckling. The deflection ratio at buckling is shown on the right-hand side of the figure. The shape of the deflection vs. position curve is similar to the curve with no current. But energy is more spread out among the neighboring rings.

Ten-Ring Model

The 10 coplanar rings with radii ranging from 11 cm to 20 cm were analyzed in the same fashion. The buckling current results are shown in Table 4.7. The stability exhibits the same pattern shown by previous results. The circumferential third and sixth modes are chosen for the plot of the current-frequency dispersion curves, which are shown in Figures 4.21 and 4.22, respectively. The R6, R7 and R8 modes, which are unstable in C3 mode deformation, become stable for the higher C6 mode. The deflection vs. position curves at buckling for these modes are plotted in Figure 4.23. The comparison of the curves shows that the

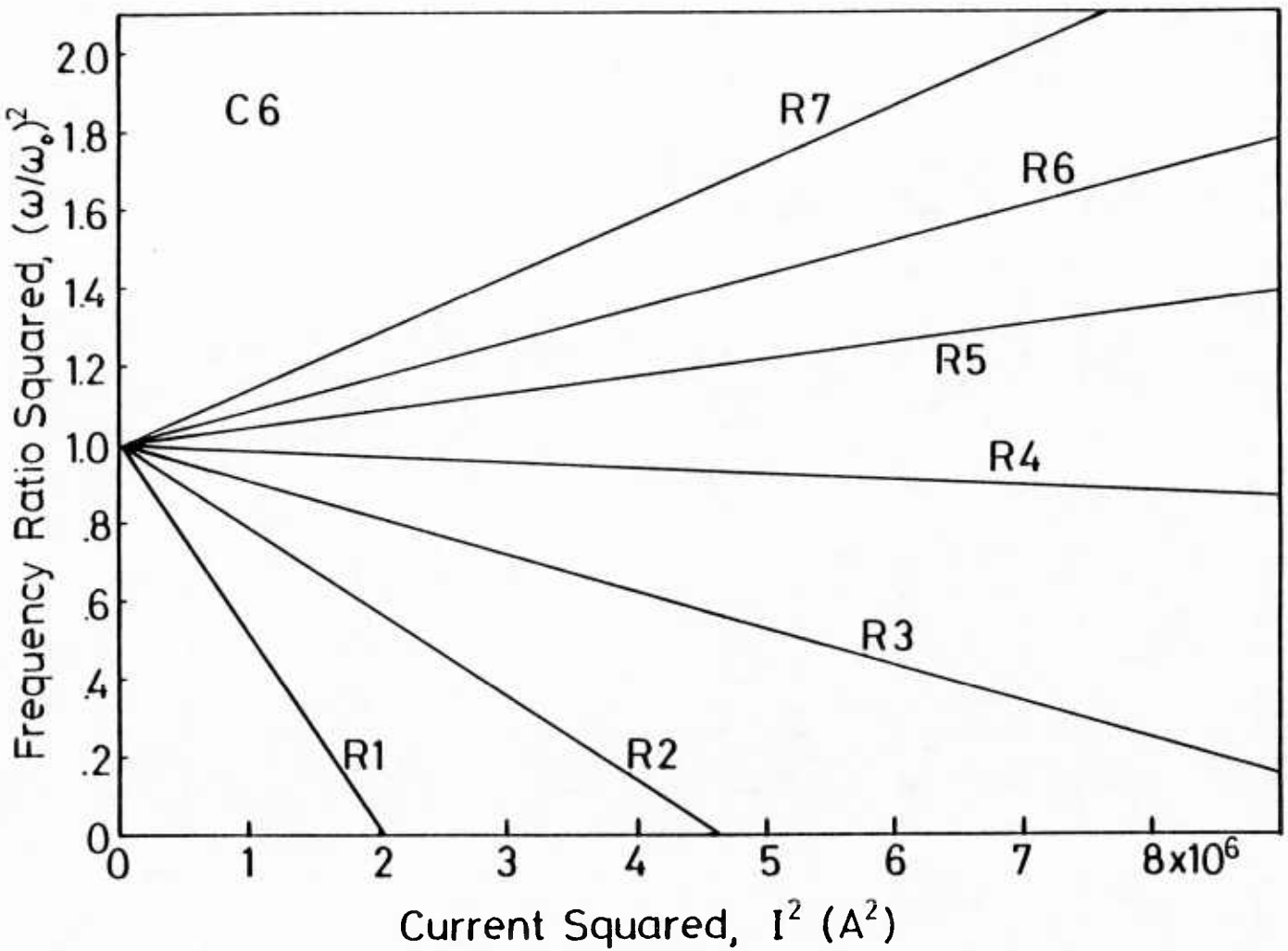

Figure 4.19 Theoretical current-frequency dispersion curves of circumferential sixth mode for seven-ring model with interturn stiffness

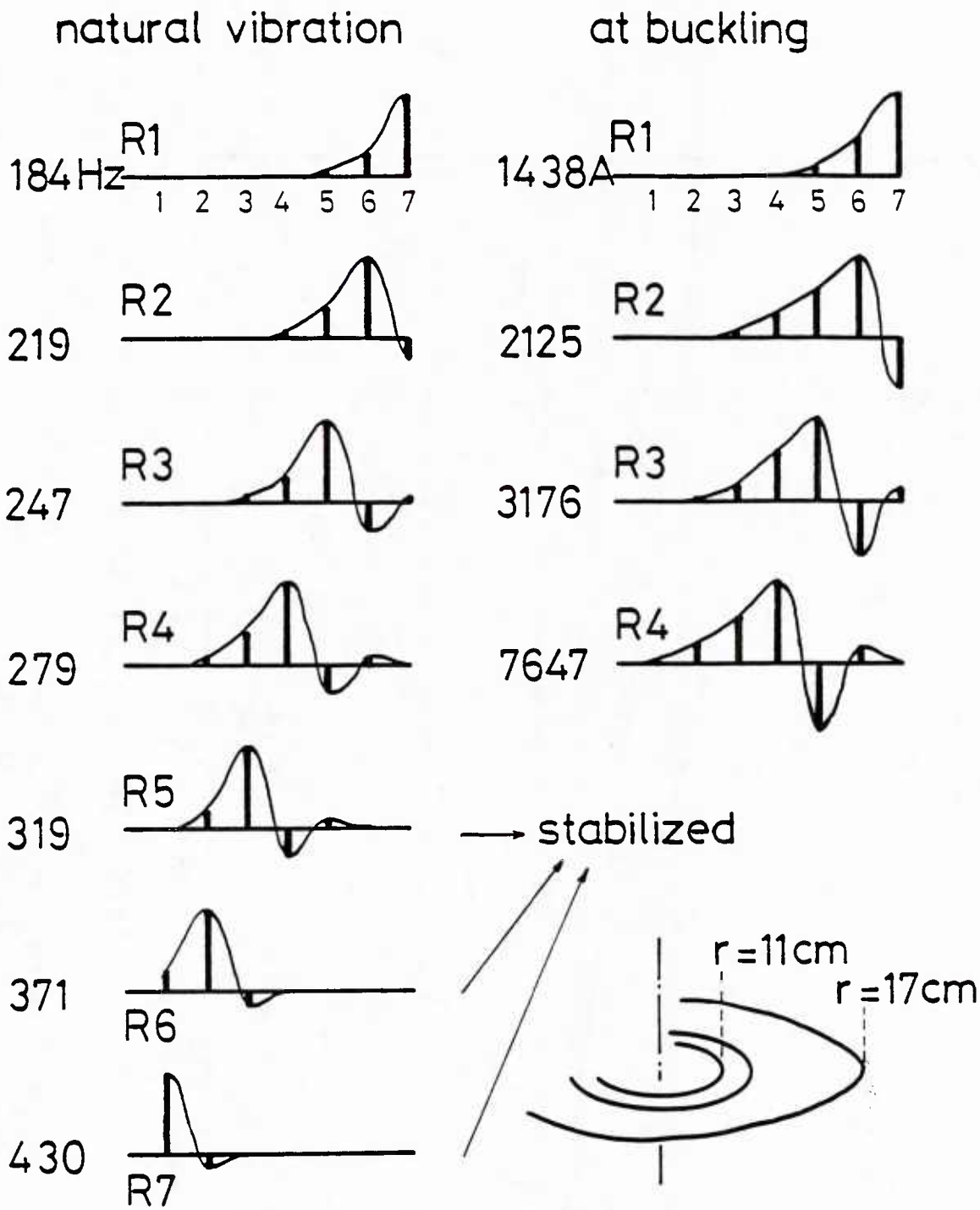

Figure 4.20 Radial or circumferential deflection vs. position curves when current is zero and at buckling for circumferential sixth (C6) mode of seven-ring model with interturn springs

Table 4.7 Theoretical critical buckling currents for 10 ring model with interturn stiffness

Radial Mode	R1	R2	R3	R4	R5	R6	R7	R8	R9	R10
Circumferential Mode	(A)	(A)	(A)	(A)	(A)	(A)	(A)	(A)	(A)	(A)
C1	0	447	374	628	955	1078	1202	-----	-----	-----
C2	148	324	555	854	1212	1626	2075	2431	2877	-----
C3	321	550	796	1089	1445	1844	2245	3044	-----	-----
C4	541	834	1142	1491	1879	2236	2431	-----	-----	-----
C5	791	1158	1531	1970	2679	4700	-----	-----	-----	-----
C6	1048	1489	1962	2685	4501	-----	-----	-----	-----	-----
C7	1297	1826	2486	3742	-----	-----	-----	-----	-----	-----
C8	1537	2179	3104	5166	-----	-----	-----	-----	-----	-----
C9	1770	2547	3883	8253	-----	-----	-----	-----	-----	-----
C10	1990	2926	4562	13476	-----	-----	-----	-----	-----	-----
C11	2226	3311	5379	24189	-----	-----	-----	-----	-----	-----
C12	2450	3699	6244	-----	-----	-----	-----	-----	-----	-----
C13	2673	4088	6871	-----	-----	-----	-----	-----	-----	-----
C14	2895	4477	8087	-----	-----	-----	-----	-----	-----	-----
C15	3116	4866	9054	-----	-----	-----	-----	-----	-----	-----
C16	3336	5253	10044	-----	-----	-----	-----	-----	-----	-----
C17	3556	5640	11053	-----	-----	-----	-----	-----	-----	-----
C18	3775	6025	12078	-----	-----	-----	-----	-----	-----	-----

deflections concentrate as the circumferential mode increases. For example, in the radial first (R1) mode, the outer rings have more significant deflections compared to the inner rings in the circumferential sixth (C6) mode.

In summary, the deflections concentrate for the stable mode and spread out for the unstable mode as the current increases. At buckling, the deflections concentrate for the higher circumferential mode.

This phenomenum was confirmed by the buckling of pancake winding experiment (Section 3.2). The experiment shows that only the outer 7 turns out of 20 deformed in the bending mode, while the inner turns deformed in the expansion mode (Figures 4.20 and 4.21). This is the typical buckling of the radial first (R1) mode for the high circumferential mode. On the other hand the result of Daniels (Figure 1. shows the typical buckling of the radial first (R1) mode for the low circumferential mode with the most windings buckled.

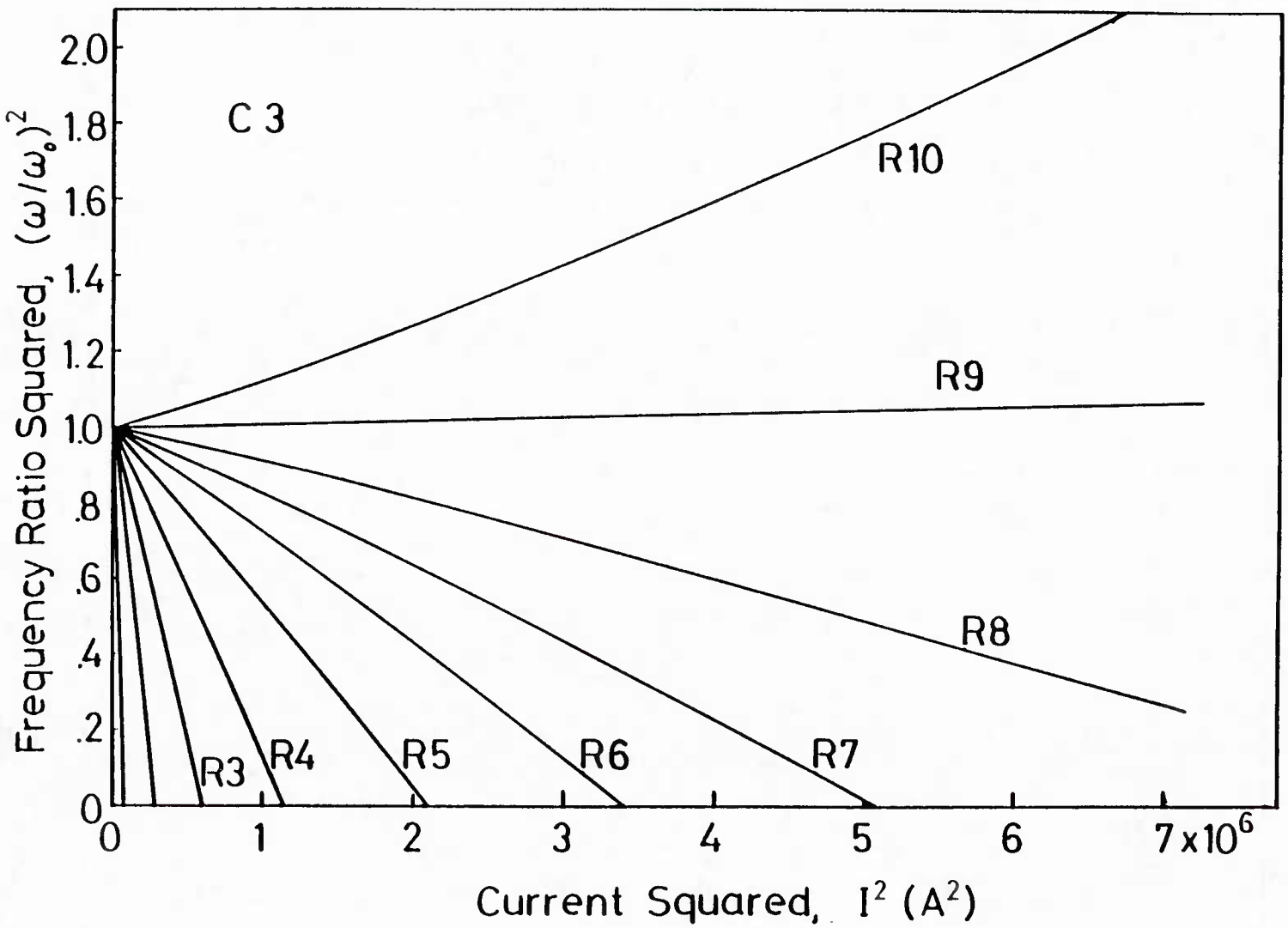

Figure 4.21 Theoretical current-frequency dispersion curves for circumferential sixth (C6) mode for ten-ring model with interturn springs

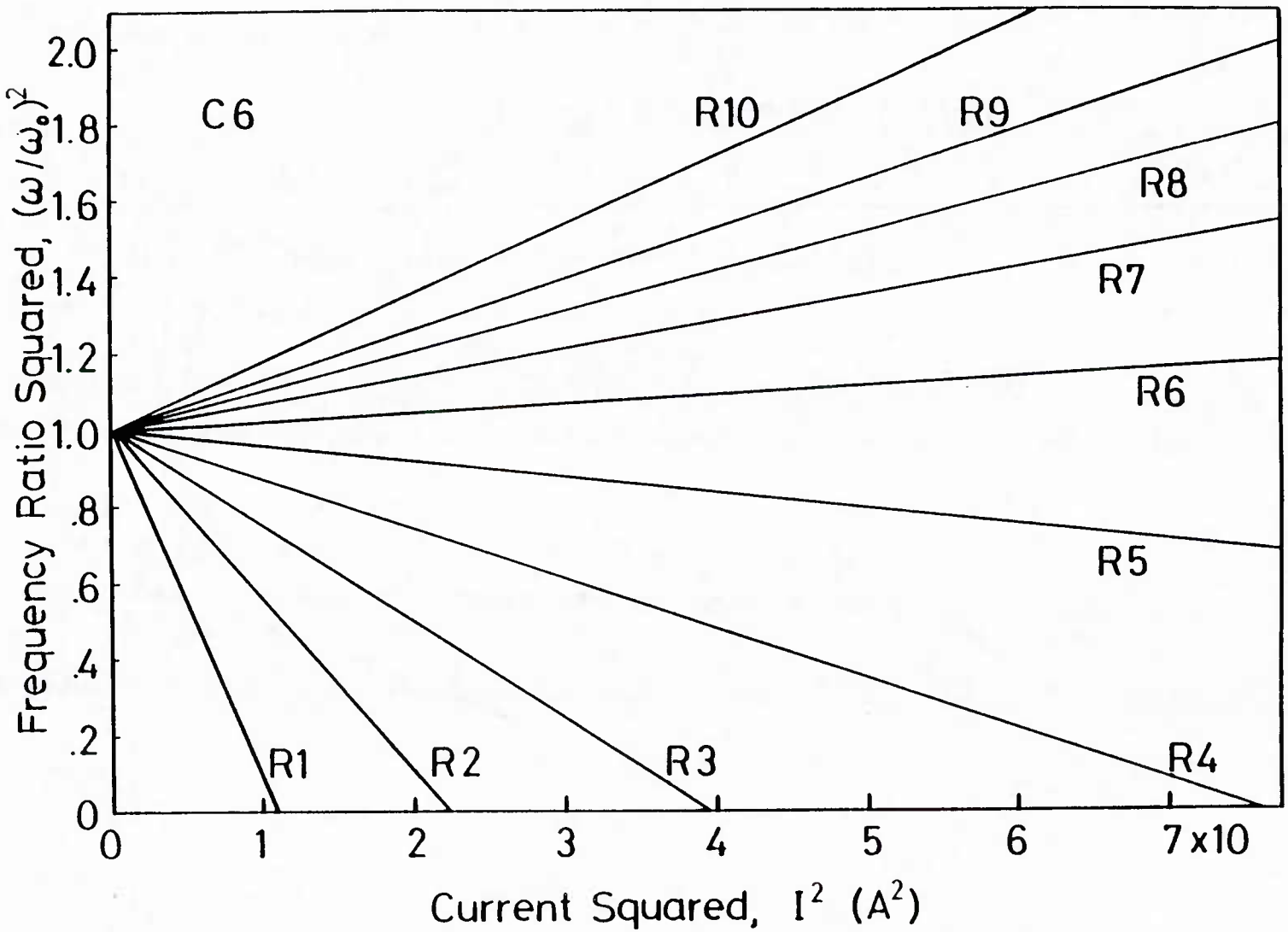

Figure 4.22 Theoretical current-frequency dispersion curves of circumferential sixth (C6) mode for ten-ring model with interturn springs

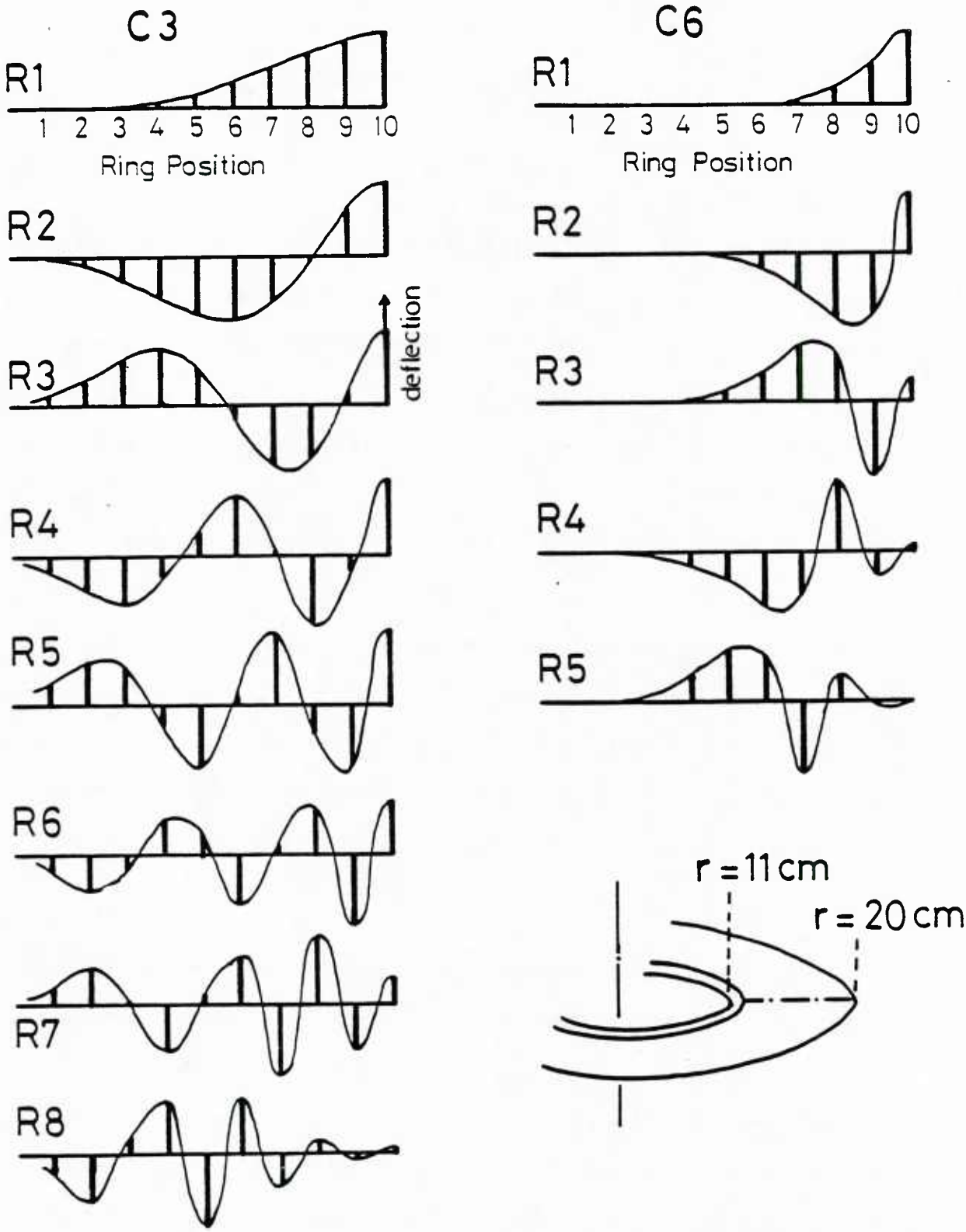

Figure 4.23 Deflection vs. position curves at buckling of circumferential third (C3) and sixth (C6) mode for ten-ring model with inter-turn springs

CHAPTER 5

CONCLUSION

Development of reliable magnets is one of the main technological problems to be solved before economic usage of high magnetic fields can be realized; for example, magnetic fusion energy, magnetohydrodynamics (MHD), accelerators in nuclear physics, nuclear magnetic resonance (NMR) for medical use. Because they are expensive and are interconnected to other parts of the system, magnets must have a life-expectancy equal to the life-time of the overall system. This thesis has presented an integrated study of the internal vibration and buckling of cylindrically wound superconducting magnets. The two-dimensional concentric multiple ring model was adapted to preserve the characteristics of the superconducting solenoid magnet. A summary of the work presented in this thesis is given below. Conclusions from the present study are then drawn. Some suggestions for further research are made at the end of the chapter.

5.1 Summary

Cylindrically wound superconducting magnets were modeled by two-dimensional multi-rings connected by soft springs, and the internal vibration and buckling of the system were studied both experimentally and analytically. Since the linear elastic theory used in the previous studies has failed to predict buckling and vibration of the internal turns in the bending mode, elastic ring theory was used in this study. Also the effect of the magnetic stiffness was extensively examined.

In Chapter 2 the linearized theories of electromagnetism and elasticity were summarized to provide a proper background of the theory of magnetoelasticity for nonferrous conducting materials. Ring theory was given in detail to take into account the effect of the initial tension on the bending of the ring. The magnetic field and its gradient due to a current carrying ring were discussed to calculate the initial tension and the magnetic stiffness on the ring.

Chapter 3 is devoted to the experiments. Two different experiments were conducted. A set of experiments on the vibration and stability of the superconducting concentric rings was treated first. These experiments were conducted in the cryogenic dewar at liquid helium temperature. One-turn and multi-turn elastic superconducting rings in the magnetic field of a 100-turn concentric rigid ring magnet were used to study vibration and stability phenomena. Elastic brass shim springs were used to simulate the flexibility of the insulation between the turns of an actual solenoid. Both static and dynamic methods were used to determine the critical currents. In the static test, the typical buckling cruves could not be obtained because of misalignments and imperfections in the shape of the elastic rings. The critical buckling currents were obtained by the Southwell plot. The dispersion of the natural frequencies with increase in current was obtained in the dynamic test. The decrease of the natural frequencies suggesting an instability was observed except in one mode of the three ring experiment. The second experiment was the in-plane buckling of a normal pancake coil. A 20-turn copper pancake coil was made and a high pulse

current was conducted through it. A large plastic outward deformation was observed in inner turns, while the outer turns buckled and deformed to form waves.

Analytical and experimental results were compared in Chapter 4. The magnetic field and gradient produced by multiple concentric rings were discussed first. It was verified that the direction of the magnetic field in the outer turn is always reversed, that the reversed magnetic field applied on the outer ring is not necessarily much smaller than one on the inner ring, and that the magnetic field inside the winding does not change linearly. The equation of motion for a single ring in a transverse magnetic field with gradient was then derived. The buckling of the ring was predicted and the frequency-current dispersion curves were obtained analytically. These results were compared with the experimental results. The theoretical and experimental critical buckling currents agreed reasonably when the magnetic stiffness was included in the analysis. However, the dynamic results agreed only qualitatively. The nondimensional analysis showed the dependency of the critical current on the spring constant and the magnetic stiffness. It was shown that the lowest circumferential mode was not necessarily the lowest buckling mode, depending on the spring constant and the magnetic stiffness. Finally, the equations for the current carrying multiple ring model were derived. The results were compared with the experimental results. They showed a qualitative agreement. These equations were applied to general cases to predict the buckling and vibration of the system. The buckling of the system was predicted for some circumferential and radial modes. The stability was shown to depend on the modes as well as the

spring constant. The frequency-current dispersion curves showed that the unstable radial mode turned to be stable for the higher circumferential mode.

5.2 Conclusions

The following conclusions may be drawn for the work presented:

1) The two-dimensional multiple ring model was adapted to analyze the inner stability and vibration of cylindrically wound superconducting magnets. By taking into account the effects of the initial tension on the bending of the ring, the buckling of the system could be predicted. Also the frequency-current dispersion about the vibration of the bending mode was obtained. These results were verified by the experiment. It is believed that this is the first complete analysis of internal buckling in solenoidal magnets.

2) The effect of the magnetic stiffness was included in the analysis and was shown to play an important role in the vibration and stability properties of the system. The critical buckling currents and the vibration frequencies calculated by this analysis agreed reasonably with the experimental results in the one-ring model, while they agreed qualitatively in the two- and three-ring models. For the one-ring model, the analytical value of the critical currents when the magnetic stiffness was neglected were much higher than the experimental values. For these reasons, the analytical method adapted in this study was proved to be effective.

3) The effect of the magnetic stiffness is larger for the lower circumferential mode. As the circumferential mode increases, the effect of the initial tension becomes dominant.

4) The non-dimensional analysis on the one-ring model showed that the critical buckling currents largely depend on the spring constant of the system and the magnetic stiffness. The lowest circumferential mode is not necessarily the lowest buckling mode, depending on them.

5) According to the analysis, the dispersion of the frequencies with increase in current did not necessarily mean instability of the system. The increase of the frequency, which implies the stability of the system, was obtained as well as the decrease of the frequency, which implies the instability. This phenomenum depends on the circumferential and radial modes of the vibration of the system.

6) In the multiple ring system with interturn stiffness, each radial mode excited one ring more than the others when the current was zero. For the lowest frequency the outer ring vibrated the most, while the innermost ring vibrated the most for the highest frequency. As the current increased the deflection spread out among the neighboring rings for the unstable mode. On the other hand, the deflection concentrated for the stable mode.

7) In the same system, the deflections at buckling concentrated as the circumferential mode increased. For the radial first (R1) mode, the deflections concentrated in outer rings and inner rings did not deform in the bending mode particularly for the high circumferential mode.

5.3 Suggestions for Further Research

The following suggestions are made for further work.

1) For the continuation of the experimental work, the multiple ring and helical coil experiments without the ambient field coil should be

conducted. This shall supply the experimental data on the analysis and also the stable in-plane vibration as well as the unstable one. Out-of-plane stability and vibration experiments should also be performed.

2) In this study the insulation between the superconductors were replaced by the radial and circumferential springs. To apply this analysis to the existing magnets, or those under design, these spring constants should be expressed by the elastic moduli of the insulation.

3) A nondimensional study of the multi-ring model should be executed as well as a parameter study.

4) The analytical method adapted here should be expanded into a three-dimensional ring model. This should not be difficult, if the radial deformation and the axial deformation are separated. Then a similar technique could be applied to other shapes of magnets such as the D-shaped magnets for Tokamak fusion and the three-dimensional coils for Yin-Yang coils. In this case, too, the effects of the initial tension and the magnetic stiffness must not be neglected. By assuming the deformed shape one could obtain characteristic euqations for the buckling and vibration.

APPENDIX A

COMPONENTS OF MECHANICAL STIFFNESS AND MAGNETIC FIELD GRADIENT COEFFICIENT MATRICES

Components of mechanical stiffness matrix $[K_2]$

$$
[K_2] = \begin{bmatrix}
\frac{\Gamma h}{R_1^2} & -\frac{h}{R_1 R_2} & & & & & \\
-\frac{h}{R_1 R_2} & \frac{2h}{R_2^2} & -\frac{h}{R_2 R_3} & & \approx 0 & & \\
 & & \frac{2h}{R_{i-1}^2} & -\frac{h}{R_{i-1} R_i} & & & \\
 & & -\frac{h}{R_{i-1} R_i} & \frac{2h}{R_i^2} & -\frac{h}{R_i R_{i+1}} & & \\
 & & & -\frac{h}{R_i R_{i+1}} & \frac{2h}{R_{i+1}^2} & & \\
 & & & & & \frac{2h}{R_{N-1}^2} & -\frac{h}{R_{N-1} R_N} \\
 & \approx 0 & & & & \frac{h}{R_{N-1} R_N} & \frac{\Gamma h}{R_N^2}
\end{bmatrix}
$$

$$k = k_x n^2 + k_z$$

Boundary Conditions

$\Gamma = 1$ if the element is connected to the neighboring element only.

$\Gamma = 2$ if the element is connected to the foundation too.

Components of magnetic field gradient coefficient matrix $[B_2]$

$$[B_2] = n^2 x$$

$$\begin{bmatrix}
-\frac{\gamma_1}{R_1} & \frac{\beta_{1,2}}{R_2} & \frac{\beta_{1,3}}{R_3} & \cdots & \cdots & \cdots & \frac{\beta_{1,N}}{R_N} \\
\frac{\beta_{2,1}}{R_1} & -\frac{\gamma_2}{R_2} & \frac{\beta_{2,3}}{R_3} & \cdots & \cdots & \cdots & \frac{\beta_{2,N}}{R_N} \\
\vdots & & & & & & \vdots \\
\cdots & \cdots & -\frac{\gamma_{i-1}}{R_{i-1}} & \frac{\beta_{i-1,i}}{R_i} & \frac{\beta_{i-1,i+1}}{R_{i+1}} & \cdots & \vdots \\
\cdots & \cdots & \frac{\beta_{i,i-1}}{R_{i-1}} & -\frac{\gamma_i}{R_i} & \frac{\beta_{i,i+1}}{R_{i+1}} & \cdots & \vdots \\
\cdots & \cdots & \frac{\beta_{i+1,i-1}}{R_{i-1}} & \frac{\beta_{i+1,i}}{R_i} & -\frac{\gamma_{i+1}}{R_{i+1}} & \cdots & \vdots \\
\vdots & & & & & & \vdots \\
\frac{\beta_{N-1,1}}{R_1} & \cdots & \cdots & \cdots & \cdots & -\frac{\gamma_{N-1}}{R_{N-1}} & \frac{\beta_{N-1,N}}{R_N} \\
\frac{\beta_{N,1}}{R_1} & \cdots & \cdots & \cdots & \cdots & \frac{\beta_{N,N-1}}{R_{N-1}} & -\frac{\gamma_N}{R_N}
\end{bmatrix}$$

$$\gamma_i = \sum_{\substack{j \\ j \neq i}} \frac{\mu}{2\pi} \frac{1}{R_j(R_j + R_i)} \left[\frac{R_j^2 + R_i^2}{(R_j - R_i)^2} E - K \right]$$

$$\beta_{i,j} = -\frac{\mu}{2\pi} \frac{2R_j}{(R_j + R_i)(R_j - R_i)^2} E \quad .$$

APPENDIX B

FLOW CHART OF PROGRAMS "STATIC" AND "DYNAMO"

"STATIC". . . . calculates buckling current of multi-ring system

$$|([K_1] + [K_2]) - (-[B_1] - [B_2])I^2| = 0 \qquad (4.3.15)$$

"DYNAMO". . . . calculates frequencies due to change of current

$$|\{[K_1] + [K_2] - ([B_1] + [B_2])I^2\} - m\omega^2| = 0 \qquad (4.3.17)$$

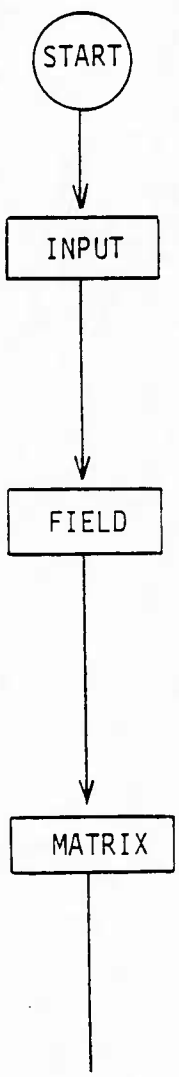

Read

Ambient field coil data

Ring data

Interturn stiffness data

Boundary conditions

Calculate magnetic field using elliptical integral tables

$[B_1]$...Magnetic initial tension eqn. (4.3.12)

$[B_2]$...Magnetic field gradient Appendix A

Calculate mechanical stiffness

$[K_1]$...Bending stiffness eqn. (4.3.11)

$[K_2]$...Interturn stiffness eqn. Appendix A

Form final determinants

$[P] = [K_1] + [K_2]$

$[D] = -[B_1] - [B_2]$

"STATIC".... $|[D]^{-1}[P]|$

"DYNAMO".... $|m^{-1}([P] + [D]I^2)|$

Calculate eigenvalues and eigenvectors by iteration method

Repetition of calculation for different currents for "DYNAMO"

Print out results

REFERENCES

Arp, V. (1977) "Stresses in Superconducting Solenoids," J. Appl. Phys., Vol. 48, No. 5, pp. 2026-2036.

Bobrov, E. S. and Williams, J.E.C. (1980) "Stresses in Superconducting Solenoids," Mechanics of Superconducting Structures, F. C. Moon, Editor, Published by ASME, New York, pp. 13-42.

Brechna, H. (1973) Superconducting Magnet Systems, Springer-Verlag, New York.

Brown, W. F. (1962) Magnetostatic Principles in Ferromagnetism, North-Holland Publishing Co., Amsterdam.

Chattopadhyay, S. (1979) "Magnetoelastic Instability of Structures Carrying Electric Current," Int. J. Solid. Struct. 15, pp. 467-477.

Cockroft, J. D. (1928) "The Design of Coils for the Production of Strong Magnetic Fields," Phil. Trans. Roy. Soc., A277, p. 317.

Crandall, S. H., Karnopp, D. C., Kurtz, E. F., Jr. and Pridmore-Brown, D. C. (1968) Dynamics of Mechanical and Electromechanical Systems, McGraw-Hill Book Co., New York.

Daniels, J. M. (1953) "High Power Solenoids: Stresses and Stability," British J. of Appl. Phys., 4, No. 2, pp. 50-54.

Dwight, J. B. (1945) Electrical Coils and Conductors: Their Electrical Characteristics and Theory, McGraw-Hill Book Co., New York.

Furth, J. P., Levine, M. A. and Waniek, R. W. (1957) "Production and Use of High Transient Magnetic Fields II," Rev. Sci. Instr., 28, pp. 949-958.

Gersdorf, R., Muller, F. A. and Roeland, L. W. (1965) "Design of High Field Magnet Coils for Long Pulses," The Review of Scientific Instruments, Vol. 36, No. 8, August, pp. 1100-1109.

Gray, W. H. and Long, C. J. (1979) "Status of the Structural Design of Superconducting Magnets for the Large Coil Program," 8th Symposium on Engineering Problems of Fusion Research, November, pp. 1953-1958.

Hague, B. (1929) The Principles of Electromagnetism Applied to Electrical Machines (originally Oxford University Press, 1929), Dover Publishers, New York.

Hara, K. and Miya, K. (1980) "Finite Element Analysis of Experiment on Dynamic Behaviour of Cylinder due to Electric Forces," Nucl. Eng. & Design, Vol. 59, August, pp. 401-410.

Haubenreich, P. N. (1981) "Superconducting Magnets for Toroidal Fusion Reactors," IEEE Transaction on Magnetics, Vol. MAG-17, No. 1, January.

Henning, C. D. et al. (1980) Mirror Fusion Test Facility Magnet-System, Final Report, Lawrence Livermore Laboratory, Livermore, CA, Rep. UCRL-52955.

Horvath, J. A. (1980) "Mechanical Behavior of the Mirror Fusion Test Facility Superconducting Magnet Coils," ASME, Mechanics of Superconducting Structures, AMD-Vol. 41, November, pp. 55-65.

Jackson, J. D. (1962) Classical Electrodynamics, J. Wiley & Sons, New York.

Jeans, J. (1925) The Mathematical Theory of Electricity and Magnetism, 5th Edition, Cambridge University Press.

Johnson, N. E., Gray W. H. and Weed, R. A. (1976) "Stress Analysis of Non-Homogeneous Transversely Isotropic Superconducting Solenoids," Proc. 6th Symp. on Eng. Prob. Fusion Research, San Diego, CA, pp. 243-247.

Kapitza, P. L. (1927) "Further Developments of the Method of Obtaining Strong Magnetic Fields," Proc. Roy. Soc. of London, A115, pp. 658-670.

Kirchhoff (1885) Annalen der Physik, Bd. 25.

Kokavec, J. and Cesnak, L. (1977) "Mechanical Stresses in Cylindrical Superconducting Coils," J. Physics D, Applied Physics 10.

Kuznetsov, A. A. (1960) "Mechanical Stresses Produced by the Radial Electromagnetic Force in Multilayer Coil Wound with Wire of Rectangular Cross Section Carrying a Uniform Current," Soviet Physics - Technical Physics, 5, pp. 555-561 (Translated from Zhurnal Teknicheskow Fiziki 30, No. 5, pp. 592-597).

Kuznetsov, A. A. (1961) "Mechanical Stresses Produced by the Radial Force in Turns in the Central Region of a Long, Single-Layer, Plane-Helix Coil," Soviet Physics - Technical Physics, 6, No. 8, pp. 687-690 (Translated from Zhurnal Teknicheskow Fiziki 31, No. 8, pp. 944-947).

Lammeraner, J. and Stafl, M. (1966) Eddy Currents, CRC Press Illiffe Books Ltd., London.

Landau, E. and Lifshitz, M. (1960) Electrodynamics of Continuous Media, Pergamon Press, New York.

Love, A.E.H. (1922) A Treatise on the Mathematical Theory of Elasticity, 4th Edition, Dover Publishing, New York.

Maxwell, J. C. (1891) A Treatise on Electricity and Magnetism I, II, Dover Publishing, New York.

Mellville, D. and Mattocks, P. G. (1972) "Stress Calculations for High Magnetic Field Coils," J. of Physics D: Applied Physics, 5, No. 10, pp. 1745-1759.

Miya, K., Hara, K. and Someya, K. (1978) "Experimental and Theoretical Study on Magnetoelastic Buckling of a Contilever Beam Plate," ASME, J. of Appl. Mech., Vol. 45, No. 5, June, pp. 355-360.

Miya, K., Takagi, T. and Uesaka, M. (1980) "Finite Element Analysis of Magnetoelastic Buckling and Experiments on a Three-Coil Superconducting Partial Torus," ASME Mechanics of Superconducting Structures, AMD-Vol. 41, November, pp. 91-107.

Montgomery, B. (1980) Solenoid Magnet Design, John Wiley & Sons, New York.

Moon, F. C. and Pao, Y.-H. (1968) "Magnetoelastic Buckling of a Thin Plate," J. Appl. Mech., 35, No. 1, pp. 53-58.

Moon, F. C. and Swanson, C. (1977) "Experiments on Buckling and Vibration of Superconducting Coils," J. Appl. Mech., 45, No. 4, pp. 707-713.

Moon, F. C. (1978) "Problems in Magneto-Solid Mechanics," Chapter V, Mechanics Today, 4, S. Nemat-Nasser, Editor, Pergamon Press.

Moon, F. C. (1980) "Magnetoelastic Instability in Superconducting Structures and Earnshaw's Theorem," ASME Mechanics of Superconducting Structures, AMD-Vol. 41, November, pp. 77-90.

Moon, F. C. and Hara, K. (1981) "Elastic Buckling of Superconducting Yin-Yang Magnets for Fusion," IEEE Trans. of Mag., Vol. MAG-17, No. 1, January, pp. 207-210.

Moon, F. C. and Hara, K. (1982) "Buckling Induced Stresses in Martensite Stainless Steels for Magnetic Fusion Reactions," Nucl. Eng. & Design, Vol. 71, pp. 27-32.

Moon, F. C. (1984) Magneto-Solid Mechanics, John Wiley & Sons, New York.

Pao, Y.-H. and Yeh, C.-S. (1973) "A Linear Theory for Soft Ferromagnetic Elastic Solids," Int. J. of Engr. Sci., 11, No. 4, p. 415.

Rose-Innes, A. C. and Rhoderick, E. H. (1978) Introduction to Superconductivity, Pergamon Press, New York.

Smythe, W. R. (1968) Static and Dynamic Electricity, 3rd Edition, McGraw-Hill Co., New York.

Sokolnikoff, I. S. (1956) Mathematical Theory of Elasticity, McGraw-Hill Co., New York.

Stoll, R. L. (1974) The Analysis of Eddy Currents, Clarendon Press, Oxford, London.

Southwell, R. V. (1932) "On the Analysis of Experimental Observation in Problems of Elastic Stability," Proceedings, Royal Society, London, Series A, Vol. 135, p. 601.

Thome, R. J. and Tarrh, J. M. (1982) MHD and Fusion Magnets: Field and Force Design Concepts, John Wiley & Sons, New York.

Timoshenko, S. P. and Gere, J. M. (1961) Theory of Elastic Stability, Second Edition, McGraw-Hill Co., New York.

Walstrom, P. L. (1975) "The Effect of High Magnetic Fields on Metal Foil Starin Gauge," Cryogenics, May, pp. 270-272.

Woodson, J. J. and Melcher, J. F. (1968) Electromechanical Dynamics, Parts I, II and III, John Wiley & Sons, New York.

Yuan, K., Abel, J. and Moon, F. C. (1981) "Eddy Current Calculations in Thin Conducting Plates Using a Finite Element Stream Function Code," IEEE Trans. Magnetics, Vol. MAG-18, No. 2, pp. 447-449.

COMPOSITE LIST OF TECHNICAL REPORTS
TO THE
OFFICE OF NAVAL RESEARCH

NUMERICAL SOLUTIONS FOR COUPLED MAGNETOTHERMOMECHANICS

Contract Number N00014-79-C-0224
Task Number NR 064-621

Departments of Structural Engineering and
Theoretical and Applied Mechanics,
Cornell University,
Ithaca, New York 14853

1. K. Y. Yuan, F. C. Moon, and J. F. Abel, "Numerical Solutions for Coupled Magnetomechanics", Department of Structural Engineering Report Number 80-5, February 1980.

2. F. C. Moon and K. Hara, "Detection of Vibrations in Metallic Structures Using Small Passive Magnetic Fields", January 1981.

3. S. Mukherjee, M. A. Morjaria, and F. C. Moon, "Eddy Current Flows Around Cracks in Thin Plates for Nondestructive Testing", March 1981.

4. K. Y. Yuan, F. C. Moon, and J. F. Abel, "Finite Element Analysis of Coupled Magnetomechanical Problems of Conducting Plates", Department of Structural Engineering Report Number 81-10, May 1981.

5. F. C. Moon, "The Virtual Theorem and Scaling Laws for Superconducting Magnet Systems", May 1981.

6. K. Y. Yuan, "Finite Element Analysis of Magnetoelastic Plate Problems", Department of Structural Engineering Report Number 81-14, August 1981.

7. K. Y. Yuan et al., "Two Papers on Eddy Current Calculations in Thin Plates", September 1981.

8. G. R. Doelp, J. F. Abel, and F. C. Moon, "Experimental and Numerical Analysis of Electric Currents and Electromagnetic Blunting of Cracks in Thin Plates", Department of Structural Engineering Report Number 84-12, December 1984.

9. K. Hara and F. C. Moon, "Stability and Vibrations of Internal Windings of High Current Superconducting Solenoids", December 1984.

10. J. F. Abel, F. C. Moon, and T. J. McCoy, "Pre- and Post-Processing for Stream-Function Eddy Current Calculations", Department of Structural Engineering Report Number 84-13, December 1984.

U219374